UNIVERSIDADE ESTADUAL DE CAMPINAS

Faculdade de Engenharia Elétrica e de Computação

Érick Alves Santos

Development of activated carbon (AC) electrodes for Lithium-Sulfur (Li-S) batteries: A scalable proposal.

Desenvolvimento de eletrodos a base de carvão ativado (AC) para baterias de Lítio-Enxofre (Li-S): Uma proposta escalável.

Campinas
2022

Érick Alves Santos

Development of activated carbon (AC) electrodes for Lithium-Sulfur (Li-S) batteries: A scalable proposal.

Desenvolvimento de eletrodos a base de carvão ativado (CA) para baterias de Lítio-Enxofre (Li-S): Uma proposta escalável.

Dissertation presented to the School of Electrical and Computer Engineering of the University of Campinas in partial fulfillment of the requirements for the degree of Master, in Electrical Engineering, in the area of Electrical Energy.

Dissertação apresentada à Faculdade de Engenharia Elétrica e de Computação da Universidade Estadual de Campinas como parte dos requisitos exigidos para a obtenção do título de Mestre em Engenharia Elétrica, na Área de Energia Elétrica.

Supervisor/Orientador: Prof. Dr. Hudson Giovani Zanin

Este exemplar corresponde à versão final da dissertação defendida pelo aluno Érick Alves Santos, e orientado pelo Prof. Dr. Hudson Giovani Zanin.

Campinas
2022

Ficha catalográfica
Universidade Estadual de Campinas
Biblioteca da Área de Engenharia e Arquitetura
Rose Meire da Silva - CRB 8/5974

Santos, Érick Alves, 1995-
Sa59d Development of activated carbon (AC) electrodes for lithium-sulfur (Li-S) batteries: A scalable proposal / Érick Alves Santos. – Campinas, SP: [s.n.], 2022.

Orientador: Hudson Giovani Zanin.
Dissertação (mestrado) – Universidade Estadual de Campinas, Faculdade de Engenharia Elétrica e de Computação.

1. Baterias de lítio. 2. Eletrodos. 3. Espectroscopia de impedância eletroquímica. 4. Enxofre. 5. Difusão. I. Zanin, Hudson Giovani, 1983-. II. Universidade Estadual de Campinas. Faculdade de Engenharia Elétrica e de Computação. III. Título.

Informações para Biblioteca Digital

Título em outro idioma: Desenvolvimento de eletrodos a base de carvão ativado (AC) para baterias de Lítio-Enxofre (Li-S): Uma proposta escalável.
Palavras-chave em inglês:
Lithium batteries
Electrodes
Electrochemical impedance spectroscopy
Sulfur
Diffusion
Área de concentração: Energia Elétrica
Titulação: Mestre em Engenharia Elétrica
Banca examinadora:
Hudson Giovani Zanin [Orientador]
Josimar Ribeiro
Gustavo Doubek
Data da defesa: 25-08-2022
Programa de Pós-Graduação: Engenharia Elétrica

Identificação e informações acadêmicas do(a) aluno(a)
- ORCID do Autor: https://orcid.org/0000-0001-5831-8706
- Currículo Lattes do autor: http://lattes.cnpq.br/0600759104621867

COMISSÃO JULGADORA – DISSERTAÇÃO DE MESTRADO

Candidato (a): Érick Alves Santos RA: 194216

Data da defesa: 25 de agosto de 2022

Título da dissertação (inglês): ‘*Development of activated carbon (AC) electrodes for Lithium-Sulfur (Li-S) batteries: A scalable proposal*’.

Título da dissertação (português): ‘*Desenvolvimento de eletrodos a base de carvão ativado (AC) para baterias de Lítio-Enxofre (Li-S): Uma proposta escalável*’.

Prof. Dr. Hudson Giovani Zanin (Presidente, FEEC/UNICAMP)
Prof. Dr. Gustavo Doubek (FEQ/UNICAMP)
Prof. Dr. Josimar Ribeiro (DQUI/UFES)

A Ata de Defesa, com as respectivas assinaturas dos membros da Comissão Julgadora, encontra-se no SIGA (Sistema de Fluxo de Dissertação/Tese) e na Secretaria de Pós-Graduação da Faculdade de Engenharia Elétrica e de Computação.

To my parents, Rita Alves Gastino and Adeval Alves dos Santos.

Acknowledgments

The acknowledgments will be written in Portuguese.

Inicialmente gostaria de agradecer aos meus pais, Rita e Adeval, por sempre me apoiar e não me deixar pensar em desistir nem por um segundo. Vocês foram fundamentais para que esse processo pudesse ser concluído com sucesso. Obrigado por serem minha base, amo vocês.

Gostaria de agradecer a Cida, que sempre me apoiou e acreditou em mim independentemente do desafio. Saiba que você foi muito importante para que eu pudesse avançar em meio as adversidades que ocorreram dá graduação até aqui, obrigado por acreditar no meu potencial.

Ao Prof. Mauro Vanderlei de Amorim pelo apoio, ajuda, discussões e amizade. Sem você essa conquista não seria possível.

Ao meu orientador Prof. Hudson Giovani Zanin pela orientação, parceria, conselhos, desafios e confiança. Todas as suas contribuições me fizeram evoluir grandemente como cientista e pessoa. Você é e sempre será minha referência. Obrigado por tudo.

Ao Professor Leonardo de Moraes (UFVJM) pela orientação, concelhos, críticas construtivas e incontáveis contribuições. Você não só foi importante para meu desenvolvimento como também é fonte de inspiração.

Ao Rodolfo Castanho Rodrigues pelas orientações, paciência, colaborações em trabalhos e amizade. Você de fato foi muito importante durante a evolução deste mestrado e da minha postura como pesquisador.

A todos os meus colegas da *BREnergies*. Sem vocês eu não teria chegado até aqui, tenho propriedade em dizer que a formação de um cientista não depende apenas dele, mas de tudo que o rodeia. Fico feliz em ter vocês ao meu lado. Agradeço a todos que me ajudaram a chegar até aqui de alguma forma, desde uma breve passagem até os que permanecem ao meu lado até hoje de forma efetiva. Vocês são incríveis e eu me sinto como tal por estar ao lado de vocês. Juntos somos mais fortes.

“This study was financed in part by the grant 2020/04281-8, São Paulo Research Foundation (FAPESP)."

"If you want to find the secrets of the universe, think in terms of energy, frequency, and vibration."

(Nikola Tesla)

"Motivation is a lie. You need consistency"

Abstract

Lithium-Sulfur batteries (LSBs) are high theoretical and specific capacity energy storage devices of 1675 mAh g^{-1} and 2600 Wh kg^{-1}. LSBs have at least five times the energy storage capacity of lithium-ion batteries. The raw material of the Li-S battery is S_8 sulfur, which has a very low cost and is an abundant resource in the national territory, which means that this technology can be improved in Brazil with a very high chance of success. Fundamental studies are taking place in the best centers in the world to solve the problems associated with the chemistry of this device. One of the biggest problems is the shuttle effect. This master's thesis aims to present an electrochemical study of the battery's internal behavior following the state of charge (SoC) variations with electrochemical impedance spectroscopy (EIS). The electrode produced here reached discharges of approximately 1350 mA.h g_{sulfur} cm^{-2}, 360 cycles and theoretical gravimetric energy of 5.0367 Wh/kg; which are superior results for the first Li-S coin cell produced in our department. The electrodes were already produced aiming at the scaling of the cell and presented excellent adhesion, capacity and flexibility. Here we have a proposal for an activated carbon (AC) based electrode with commercialization potential for the production of the first Li-S batteries made in the national territory. The results obtained are very promising for the development of Li-S batteries in Brazil.

Keywords: Li-S batteries, EIS, shuttle effect, coin cell, pouch cell

Resumo

As baterias de Lítio enxofre (LSBs) são dispositivos de armazenamento de energia de alta capacidade teórica e específica, sendo 1675 mAh g^{-1} e 2600 Wh kg^{-1} respectivamente. As LSBs têm capacidade de armazenamento de energia pelo menos cinco vezes maior que as baterias de íon-lítio. A matéria prima da bateria de Li-S é o enxofre, que tem custo baixíssimo e é um recurso abundante em território nacional, o que faz com que essa tecnologia possa ser aprimorada no Brasil com altíssima chance de sucesso. Estudos fundamentais estão acontecendo nos melhores centros do mundo para resolver os problemas associados à química desse dispositivo. Um dos maiores problemas é o efeito *shuttle*. Essa dissertação de mestrado tem como objetivo apresentar um estudo eletroquímico do comportamento interno da bateria acompanhando as variações do estado de carga (SoC) com a espectroscopia de impedância eletroquímica. O eletrodo aqui produzido alcançou descargas de aproximadamente 1350 mA.h $g_{enxofre}$ cm^{-2}, 360 ciclos e energia gravimétrica teórica de 5,0367 Wh/kg; que são resultados surpreendentes para a primeira célula moeda de Li-S produzida em nosso departamento. Os eletrodos já foram produzidos visando o escalonamento da célula que aqui apresentaram excelente aderência, capacidade e flexibilidade. Aqui temos uma proposta de eletrodo a base de carvão ativado (AC) com potencial de comercialização para produção das primeiras baterias de Li-S feitas em território nacional. Os resultados obtidos são muito promissores para o desenvolvimento de baterias de Li-S no Brasil.

Palavras-chave: baterias de Li-S, EIE, efeito *shuttle*, *coin cell*, *pouch cell*.

List of Figures

List of Tables

List of Acronyms

AC	Activated Carbon
AC:S	Activated Carbon and Sulfur
AP	Pyrolyzed to 1000ºC
BP	Pyrolyzed to 500ºC
BP	Black Pears
CV	Cyclic Voltammetry
CNLS	Complex Nonlinear Squares
CPE	Constant Phase Element
CB	Carbon Black
DOL	1,3-Dioxolane
DOD	Deep of Discharge
DME	Dimethoxyethane
DMC	Dimethyl Carbonate
DEC	Diethyl Carbonate
EIS	Electrochemical impedance spectroscipy
E/S	Electrolyte/Sulfur
EC	Ethylene Carbonate
ESR	Equivalent Series Resistance
FSW	Finite Space Warburg
GCPL	Galvanostatic Cycling with Potential Limitation
GCD	Galvanostatic Charge-Discharge
GEIS	Galvanostatic EIS
GWE	Generalized Warburg Element
HF	High Frequencies
LF	Low Frequencies
LPS	Lithium Polysulfide
LI-S	Lithium-sulfur
LSBs	Lithium-sulfur batteries
LIBs	Lithium-ion batteries
LiTFSI	Lithium Bis (Trifluoromethanesulfonyl)Imide

MF	Middle frequency
MWCNT	Multiwalled Carbon Nanotube
NMP	N-Methyl-2-Pyrrolidone
N/P	Negative and Positive Electrode
ND	Number Donor
OCV	Open-Circuit Voltage
PC	Propylene Carbonate
PP	Polypropylene
PVDF	Polyvinylidene Fluoride
RGO	Reduced Graphene Oxide
SoC	State of Charge
SoH	State of Health
SEM	Scanning Electron Microscope
SEI	Solid Electrolyte Interface
TEGDME	1,2-Dimethoxyethane and Tetra (Ethylene Glycol) Dimethyl Ether
WVW	Working Voltage Window
XPS	X-ray Photoelectron Spectrometry

List of Symbols

e^-	Electron
$Ø$	Thickness Membrane
εr	Dielectric Constant
δI	Wave Amplitude
π	*pí*
F	Frequency
$I_{d.c}$	Direct Current
μA	Microampere
$sp^{2/}sp^3$	Hybridization of Atomic Orbitals
W	Warburg
W_o	Open Warburg
Z_f	Faradaic Impedances
R_{ct}	Overall Charge-Transfer Resistance
C_{dl}	Overall Electrical Double-Layer Capacitance
R_e	Equivalent Series Resistance
χ^2	Xí Square
Ω	OHM
φ	Phase Angle
ω	Angular Frequency
C_W	Pseudocapacitance
l	Effective Diffusion Length
σ	Warburg Coefficients
D	Diffusion Coefficients
Z_{cpe}	CPE Impedance
Y_o	Admittance of the Constant Phase Element
C	Overall Capacitance
μF	Micofaraday
Z_{GWE}	GWE impedance
D	Diffusion Coefficient
T/s	Characteristic Time Constant

T	Active Redox Species Diffuse
R_o	mass-transfer resistance
n	Fractal Mass Transport of the Redox Species
ΔOCV	Variation in Open-Circuit Voltage
I_{sd}	Self-discharge current
t	Time
ppm	Part Per Million
C-*rate*, C	Charge and Discharge in One Hour
R_{CT}	Charge Transfer Resistance

Summary

1 Li-S battery presentation

The great demand for better energy storage systems in portable electronic devices, electric vehicles, and smart power grids has driven worldwide continuous technological developments [1]. In this scenario, lithium-sulfur batteries (LSBs) have received significant attention in the last decade due to their high theoretical specific capacity and energy of 1675 mAh g^{-1} and 2600 Wh kg^{-1}[2–4], respectively. This specific capacity is much higher than that observed for the conventional cathode materials used in lithium-ion batteries (LIBs) of *ca*. 100–250 mAh g^{-1} [4]. In addition, sulfur has impressive characteristics such as natural abundance, eco-friendly properties, and low-cost [5]. The LSB is a promising electrochemical device for energy chemistry conversion and storage. Figure 1 presents the schematic cell configuration of LSB, evidencing anode and cathode, electrolyte, separator and casing. The LSB are very similar to lithium-ion batteries (LIBs), with advantages and disadvantages [6]. A great advantage of LSBs is that compared to LIBs, a much higher capacity is observed, in addition to the fact that the use of sulfur makes this battery extremely low cost, does not generate explosive and extremely toxic gases. Disadvantages are power density and ciclability.

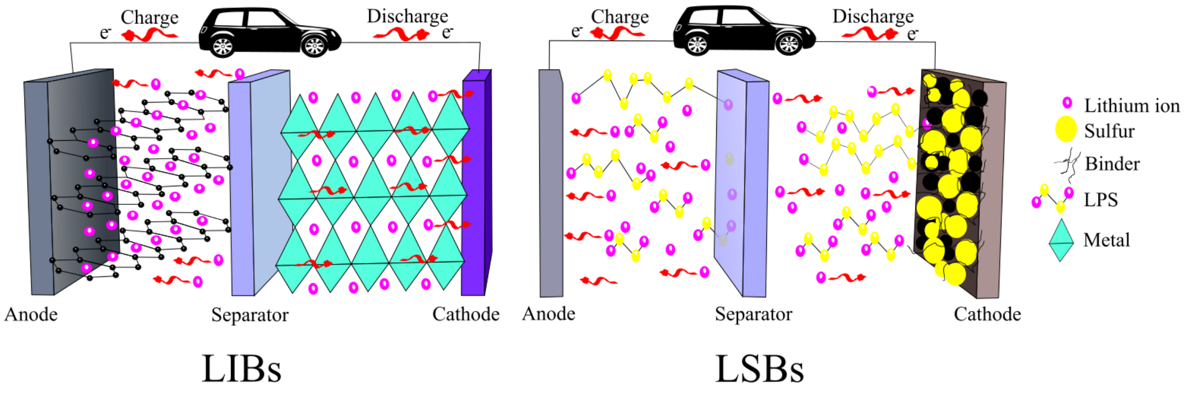

Figure 1.0 – a) Electrochemical behavior for lithium-ion batteries (LIBs), b) electrochemical behavior of lithium sulfur batteries (LSBs).

As mentioned, the Li-S battery has a system very similar to batteries already on the market, having differential structural modifications in the cathode that allows it to have this characteristic name. **Figure 1.2** illustrates in a didactic way the structural organization of the Li-S battery and the transport of lithium-ion during its oxidation and reduction process.

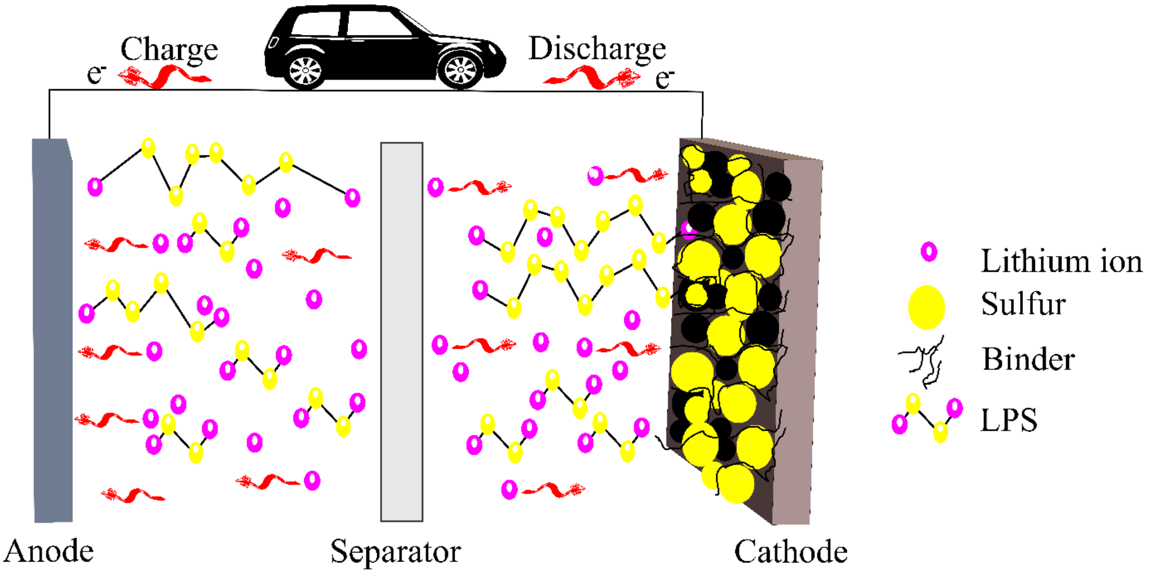

Figure 1.2 *- Internal components of Li-S Battery.*

In simple lithium-sulfur batteries, some components for their assembly deserve to be highlighted. The variation of these components will present different results about capacity, the number of cycles, internal impedance, and self-discharge, among other properties considered limiting for the evaluation of efficiency and viability of this product. Among the most important components, the metallic lithium anode [7], cathode based on doped carbon/sulfur allotropes[8], separator[9], electrolyte [10] and encapsulation are fundamental. It is essential to choose the best materials to compose this system in a cheap and fast way, avoiding very complex and toxic synthesis processes for the environment. With a focus on producing innovative national technology, which is scalably viable for mass production and using abundant local natural resources, two components stand out strongly, namely the electrolyte and the electrode, as together they make up approximately 60% of the mass of this type of battery[11]. **Figure 1.3** shows the distribution of battery elements in percentage for both coin cell and pouch cell models[12].

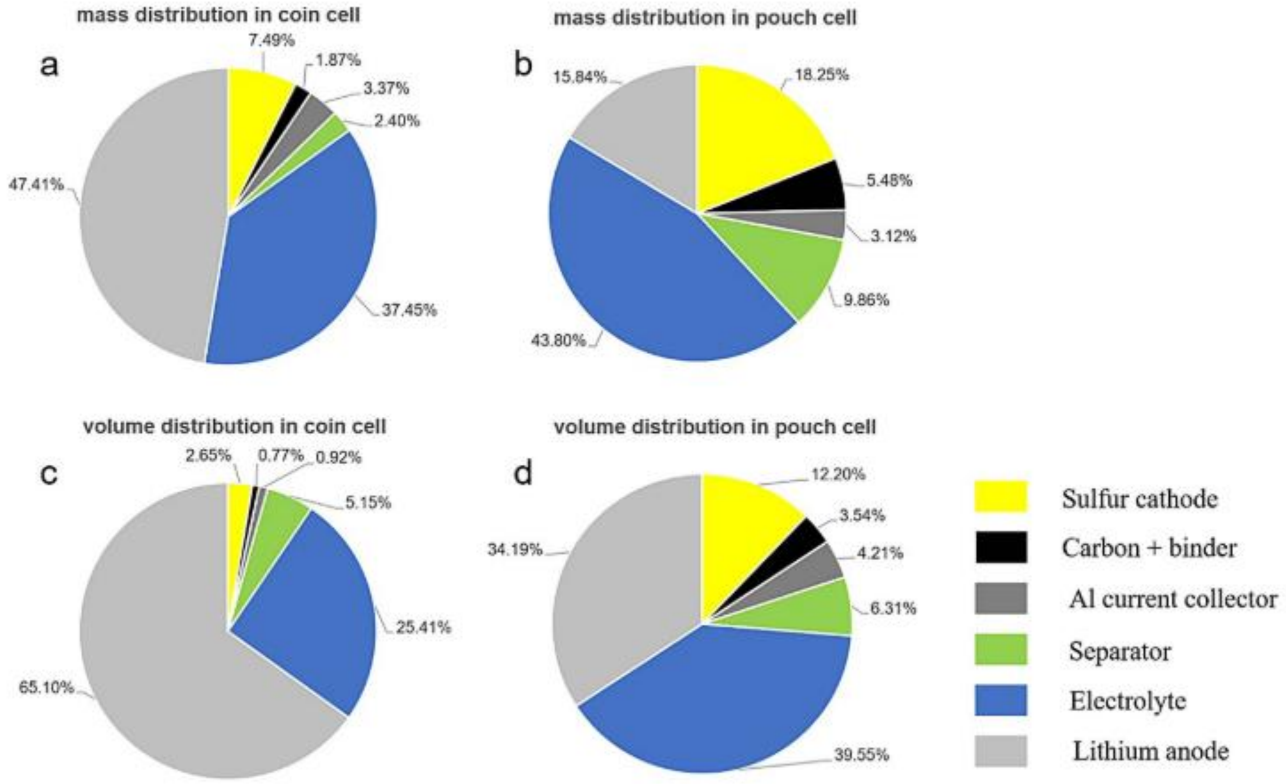

Figure 1.3 - Distribution of components used to produce Li-S batteries for a coin cell(a), pouch cell (c) and the volume of distribution of these materials within the cell, also for the coin cell (c) and pouch cell(d) Reproduced from James B Robinson et al, 2021 roadmap on lithium-sulfur batteries, 2021, J. Phys. Energy,10.1088/2515-7655/abdb9a, used under Creative Commons CC-BY license[12].

Knowing these parameters is essential to obtain a good result compared to the state of the art of technology. The proportions vary greatly between cells in scale from coin cell to pouch cell, but even so, an electrode with good surface area and high-capacity electrolyte are important factors that are preserved in both systems. **Figure 1.4** shows us the state of the art for these parameters and they can be changed when using different materials, mainly the ideal S_8 loading on each electrode[12].

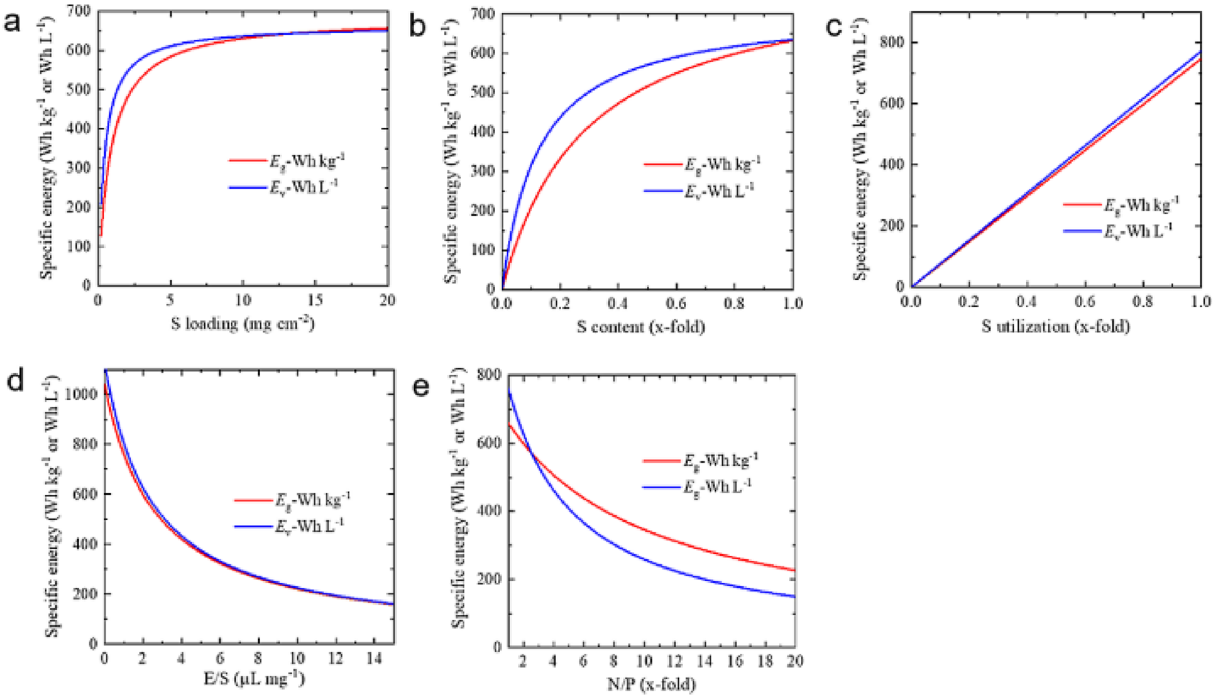

Figure 1.4 - Parameters considered essential for the production of a good Li-S battery (a) S charging, (b) S content, (c) S utilization, (d) E/O, (e) N/P. Each graph is plotted as a function of one parameter fixing the other four parameters. S load: 6 mg cm^{-2}, S content: 0.8, S utilization: 0.8, E/O ratio: 2 µl mg^{-1}, N/P ratio: 2. Reproduced from James B Robinson *et al*, 2021 roadmap on lithium-sulfur batteries, 2021, J. Phys. Energy,10.1088/2515-7655/abdb9a, used under Creative Commons CC-BY license.. [12].

Following this reasoning, knowledge of the composition, synthesis process and application of these materials is of paramount importance for understanding and motivating the studies carried out in this research proposal at the master's level. In sequence, we present the variations of these materials that exist in the literature and those of greatest interest to carry out this case study.

1.1 Organic electrolytes

Electrolytes are constantly changed to obtain good efficiency in lithium-sulfur batteries. It is possible to find solid [13–15], quasi-solid[16], organic solvent [10,17–21], ionic liquid[22,23], among others within models reported in the literature. These electrolytes feature simplicity in preparation and high ionic conductivity. Organic electrolytes are divided into two groups that stand out for their high efficiency and stability. The first group is formed by organic carbonates such as ethylene carbonate (EC), propylene carbonate (PC), dimethyl carbonate (DMC) and diethyl carbonate (DEC). The second group is formed by ethers, such as 1,3-dioxolane (DOL), 1,2-dimethoxyethane and tetra(ethylene glycol) dimethyl ether (TEGDME) among others [24]. DOL presents an improvement in the solubility of the electrolyte that contains the polysulfides and high stability when in contact with the lithium metal electrode, thus reducing the viscosity of the electrolyte when it is in the phase of formation of a two-phase state in the process of reducing molecules in a solid of LSBs[25]. TEGDME has a high Glyme structure with a high donor number (ND=18.6) and a low dielectric constant (εr = 7,9), which has sufficient capacity to dissociate the lithium salt and the active sulfur material. 1,2–Dimethoxyethane (DME) also has a high lithium polysulfide dissolution capacity and can provide sufficient amounts of active materials[26].

Given the importance of the electrolyte, it is necessary to find one that presents good compatibility and suitable property for the Li-S system, having good conductivity and low viscosity. **Figure 1.5** illustrates in schematic form the composition that stands out for producing an efficient electrolyte and adopts it as a standard in organic electrolytes formed by the ether groups.

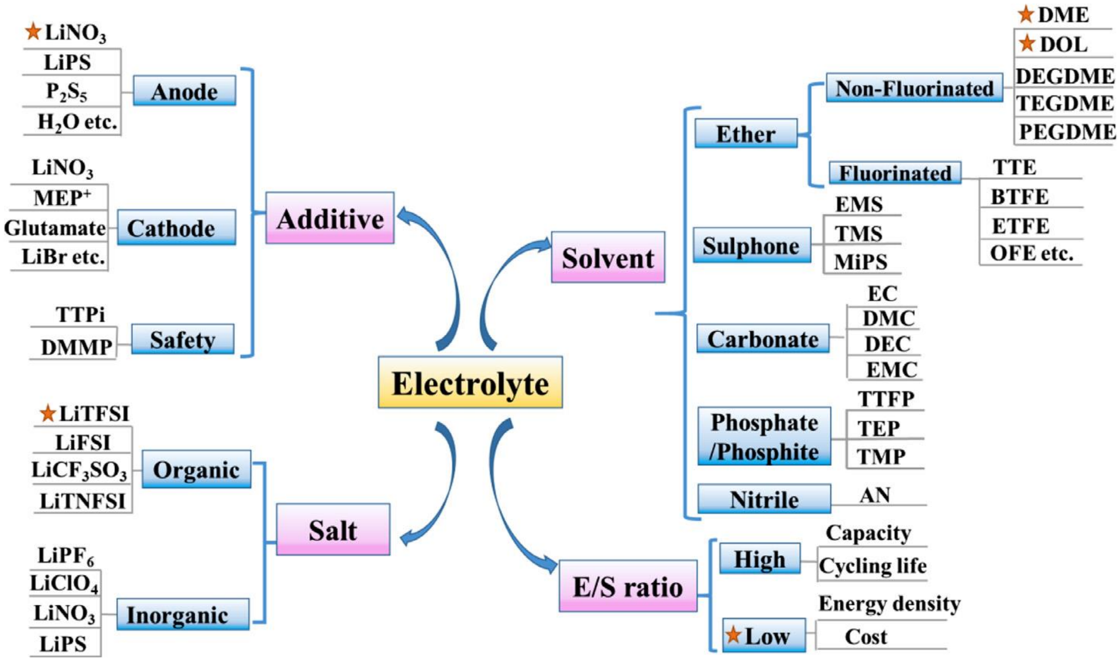

Figure 1.5 – Presentation of the composition of organic electrolytes used in lithium-sulfur batteries. With red stars, the most efficient components were highlighted. Reproduced with permission [10].

From the diagram presented, it is possible to conclude which reagents have the best result. Of this composition, the use of lithium nitrate ($LiNO_3$) as an additive, lithium bis (trifluoromethane sulfonyl) imide (LITFSI) as a salt, 1,3-dioxolane (DOL) and 1,2-dimethoxyethane (DME) as solvents stands out. organic[10]. This electrolyte is extremely effective, using the smallest proportions of reagents possible with excellent cost-effectiveness[27,28][29] which is why we will use it in this work.

1.2 Carbon-based electrodes as Li-S battery cathodes

The carbon-based electrodes used as cathodes of Li-S batteries are essential to obtaining good electrochemical results. Due to this fact, some materials are highlighted, such as Reduced Graphene Oxide (rGO)[30–32], Multi Layer Carbon Nanotude (MWNTC)[33,34] and Activated Carbon (AC)[35,36,36–40]. Both rGO and MWCNT are materials obtained through expensive processes involving highly acidic reagents and strong oxidants [41]. In this work, we think of easy and scalable production, and AC is more promising because it can obtain it in a pyrolysis process from biomass [42] and our group has great experience in making electrodes from carbon materials[43–147]. Its main feature is its high surface area and porosity. To better take advantage of these properties, the electrode doping process must be done as effectively as possible, which takes less cost (energy) for large-scale processes. Among the doping processes, co-precipitation in solution [148], vaporization [149], mechanical mixing [150] and melt-difusion[22,151–153]. Thinking in carbon electrode materials our group are specialist and have a larger expertise in to use different allotropes of carbon for this aplication. **Figure 1.6** illustrates the different forms and doping of sulfur on carbon electrodes.

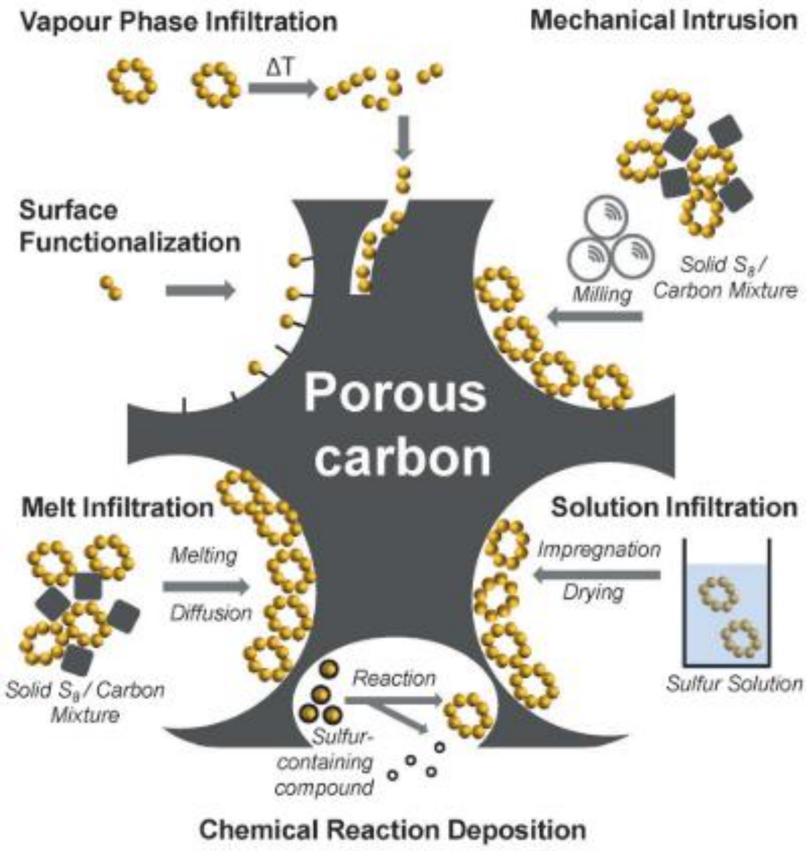

Figure 1.6 – diferentes formas de impregnação de enxofre em estruturas de carbono como eletrodos de baterias de Li-S. Reproduced with permission [154].

The melt-diffusion process is practical for bringing the electrodes to a relatively low temperature (155 ºC) for only 30 minutes. In melt diffusion, S_8 melts onto carbon, leading to electrode doping, as shown in **Figure 1.6**. This process proves effective for processes that take large-scale synthesis into account. Based on the above facts, the proposal to use structurally doped AC via the S_8 melt-diffusion process appears to be a plausible choice. After choosing and assembling the battery, some tests are shown to be extremely important to observe the Li-S battery's electrochemical behavior. For us, carbon will be applied as a high surface area electrode to allow the chemical conversion reaction of the species from S_8 to Li_2S_8, that is acknowledged as the phase solid to liquid species form and after that the reduction of Li_2S_8 to Li_2S. The more porous and the greater the surface area, the better for the interests of this work. To understand the chemical processes that take place here, the next section was created, where the knowledge about the oxidation and reduction processes that occur in the electrode bulk and its surface is duly detailed.

Chapter 2 presents the internal process of the Li-S battery, the chemical conversion process, the general equation and half-reactions of the oxidation and reduction processes during charging and discharging, as well as an introduction to the advantages and disadvantages of this technology.

2 Overview of electrochemical behavior of Li-S batteries and shuttle effect

When the battery begins to charge, there is the oxidation of the lithium electrode at the anode with the release of 1 electron and the reduction of sulfur in the cathode that receives this electron from Li^+. At the cathode, the S_8 structure from sulfur is observed in its solid-state orthorhombic crystalline morphology. The reaction of lithium-ion and sulfur produces a poly lithium sulfide (LPS), Li_2S_n, where the value of "n" can vary between 1-8. In the reduction of sulfur, it changes from the orthorhombic phase (S_8) to the monoclinic phase (Li_2S_n). In charge and discharge of Li-S battery is possible to observe the process of reduction of sulfur in its solid-state (S_8), which presents a high degree of S-S bonds during the high order LPS reduction reaction, and this occurs at approximately 2.4 V. First, a long sulfur chain is formed with a lithium atom at each end. Subsequently, this chain is reduced until it finds its shortest state, known as lithium disulfides (Li_2S_2) and sulfides (Li_2S). This process takes place while the battery charge is consumed. When the inverse process is observed, so that the battery begins to be charged, the lithium sulfides that are in solid-state in their most reduced version. This carry out the formation process of soluble species, which evolve to the S_8 molecule in the started process [155]. During the discharge stage, very well-defined levels are formed, giving the reader and researchers which species are involved during the redox process of this battery. Each level shows which types of species are predominantly participating there. Each generated species then presents information on potential (Voltage vs Li^+/Li) and associated capacity (mA h g^{-1}). That process guides the discharge curve shape, which represent the redox processes associated with structural modification of species. In the charge, we have something very similar happen[155].

The Li-S battery, during its oxidation and reduction process, has 4 important regions[29] The first region is associated with the voltage drop (2.4-2.2V vs. Li^+/Li) resulting from the reduction of the solid-state sulfur molecule (S_8) to the S_8^{2-} ion, which is soluble in most electrolytic media. The second region is characterized by the sudden voltage drop as an additional reduction of ¼ per sulfur atom (S) occurs, along with complex series of equilibrium reactions that resulted in the LPS chain length reduced to four sulfur atoms (Li_2S_4). The third region is a flexible voltage plateau (~2.1V vs. Li^+/Li) that is associated with the ½ (e-) reduction of tetra sulfide to lithium disulfide (Li_2S_2), as well as the deeper reduction (1 e-) for Li_2S. The last discharge step takes place in region four, where the total reduction of the molecule takes place. In the vast majority of electrolytic media, disulfide and sulfate are insoluble, leading to precipitation of both [17,156,157].

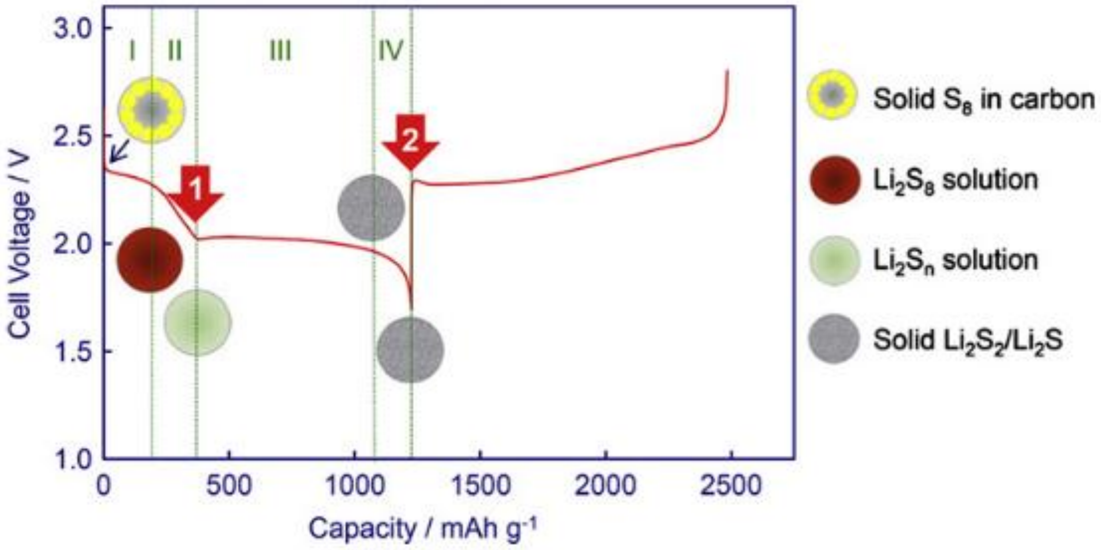

Figure 2.0 Sulfur in its solid-state. II) Formation of long-chain LPS and beginning of the Solid-Liquid phase of the Li-S battery. III) Predominance of short-chain LPS. IV) Formation of lithium disulfides in solid-state. . Reproduced with permission [158].

This type of battery is reported by the scientific community as safe and environmentally friendly, and compared to other types of galvanic cells, such as lead acid or Li-ion, for example, its toxicity to the environment is very low. LSBs have good theoretical results and very high potential compared to the technologies currently developed in the field of energy storage, where it is possible to observe in several works of literature, that their theoretical capacity of 1675 mA h g^{-1} and theoretical specific energy of 2600 Wh kg^{-1}[159]. One of the disadvantages of LSB compared to LIB is life cycles, interleaving batteries have charge and discharge numbers many times higher compared to lithium-sulfur batteries, which are known as conversion batteries, so there is a conversion of chemical energy into electrical energy. The main malefactor of this undesirable effect is due to the formation of sulfur precipitates, which are the lower order polysulfides (Li_2S_2 and Li_2S). Its formation in the electrolyte causes disastrous effects on the development of this battery, which causes it to end its life cycle very prematurely.

Two distinct peaks are observed during the discharge and charge voltage as shown in the indications of the red arrows. Arrow 1 corresponds to the point where the electrolyte solution has its highest viscosity, as it marks the moment of change of all the S_8 present in the carbon electrode being reduced to Li_2S_8, they are responsible for this increase in viscosity due to the size of their chain and the concentration. Arrow 2 shows reduced polarization due to the phase transition of LPS from the solid phase to the phase that is dissolved in the electrolyte. During discharge, the electrode presents a coating of these species in a solid-state and this leads the cell to high polarization. On charge, solid LPS is oxidized to the soluble phase and causes a decrease in cell polarization.

Here we conclude that the cell undergoes different polarization effects depending on the transition state of the sulfur molecule during the redox process and this can be observed by the peaks indicated from the 4 regions of the charge and discharge graph that are highlighted in it as regions I through IV (see more in **Figure 2.0**). The sulfur mixture is as efficient as its addition in the liquid phase, it is already from a specific potential that the cell capacity graph is formed, which comes from the chemical conversions of LPS [160]. The Li-S battery does not depend on the initial state of sulfur itself to obtain a good development, so we can add it either in solid phase such as S_8 or liquid phase such as long-chain LPS, since sulfur in its solid state only starts to reduce from approximately 2.4 V. In this way, what we observe above this potential can be reduced, causing the cut-off of the window to also decrease and act only within the reduction space of the long and short chain polysulfides.

According to some researchers reported, the effect of the appearance of these species in the battery electrolyte causes the ionic impediment of the lithium species to access the battery pores, resulting in a sudden decrease in the energy storage capacity, formation of an insulating film on the separator/anode /cathode, in addition to consuming in parts the amount of useful S_8 of the system, which leads the battery in each charge and discharge to also decrease its capacity, since the global reaction of this cell corresponds directly to the interaction between sulfur and lithium ions provided by the electrode and electrolyte. The name of this effect that calls into question the qualifications of this very promising energy conversion system is Shuttle[161–164]. The Shuttle effect is the main problem of LSBs and most of the efforts to solve the problems of this battery are on top of that regarding the cathode and cell development. In addition, as this battery uses lithium metal as an anode, another problem is observed, which is the formation of lithium dendrites. The dendrites work like spikes that grow in a disorderly way on top of the lithium electrode, caused by the migration of this ion as it leaves the metallic lithium anode of the discharge process, when it is oxidized. Lithium is transported towards the cathode and then in the charging process it returns to the anode, causing the formation of an irregular solid layer of this material. The uncontrolled growth of this material over the course of battery operation causes it to puncture the separator and cause a short circuit in the cell [2,155,165–173].

2.2 Mechanistic Understanding of Li-S

The Li-S battery presents a general mechanism of oxidation and reduction that occurs during the charging and discharging processes at the electrodes, which are well known in the literature. The complete system is complex and involves more steps. Please refer to the following literature to learn more below is shown the redox mechanism of this type of battery in its summarized form.

The first equation represents the initial reaction between the electrodes, where there is an exchange of electrons between metallic lithium and solid sulfur, thus producing LPS.

Eq. 1 $$16Li^{+} + 16e^{-} + S_8 \leftrightharpoons 8Li_2S$$

This process of formation of LPS causes the production of vacancies in the electrode due to its dissolution in the electrolyte.

Eq. 2 $$S_8 + 2Li^{+} + 2e^{-} \leftrightharpoons Li_2S_8$$

The functioning of a Li-S battery has, as known in the literature, four stages of operation, in which the first is described in Eq. 2. In the second stage, it is possible to observe that the cell voltage decreases due to the increase of the electrolyte viscosity via LPS formation.

Eq. 3 $$Li_2S_8 + 2Li^{+} + 2e^{-} \leftrightharpoons Li_2S_{8-n} + Li_2S_n$$

In the third stage, two liquid phases are observed in the electrolyte due to the dissolution of the disulfide in the organic electrolyte, a stage also known as catholyte, which undergoes reduction until reaching the minimum number of sulfur in its molecule.

Eq. 4 $$2Li_2S_n + (2_{n-4})\mathrm{Li} \leftrightharpoons nLi_2S_2$$

Eq. 5 $$Li_2S_n + (2_{n-2})\mathrm{Li} \leftrightharpoons nLi_2S$$

In the fourth stage, the maximum reduction of lithium sulfide occurs, where the molecule reaches its insoluble state in the electrolyte. The kinetics of this step is slow and undergoes high polarization due to the non-conductivity of the chemical species[174].

Eq. 6 $$Li_2S_2 + 2Li^{+} + 2e^{-} \leftrightharpoons 2Li_2S$$

From these reactions, the battery stores and supplies energy. The SoC and its respective variation (0 until 100% or vice versa) will determine to the user whether the battery is charging or discharging, hence the direction in which these reactions are taking place.

In more detail, the discharge step for LSBs is presented here below[175].

High or 1st plateau 2.7- 2.1V

Eq. 7 $S_8 + 2e^- \rightarrow S_8{}^{2-}$

Eq. 8 $S_8 + 4e^- \rightarrow S_7{}^{2-} + S^{2-}$

Eq. 9 $S_8 + 4e^- \rightarrow S_6{}^{2-} + S_2{}^{2-}$

Eq. 10 $S_8 + 4e^- \rightarrow S_5{}^{2-} + S_3{}^{2-}$

Eq. 11 $S_8 + 4e^- \rightarrow S_4{}^{2-} + S_4{}^{2-}$

Stage 2 - High to low plateau 2.3–2.1 V (mid-way on 2nd plateau).

Eq. 12 $S_8{}^{2-} + 2e^- \rightarrow S_6{}^{2-} + S_2{}^{2-}$

Eq. 13 $S_8{}^{2-} + 2e^- \rightarrow S_5{}^{2-} + S_3{}^{2-}$

Eq. 14 $S_8{}^{2-} + 2e^- \rightarrow S_4{}^{2-} + S_4{}^{2-}$

Eq. 15 $S_7{}^{2-} + 2e^- \rightarrow S_4{}^{2-} + S_3{}^{2-}$

Eq. 16 $S_6{}^{2-} + 2e^- \rightarrow S_3{}^{2-} + S_3{}^{2-}$

Eq. 17 $S_5{}^{2-} + 2e^- \rightarrow S_3{}^{2-} + S_2{}^{2-}$

Eq. 18 $S_4{}^{2-} + 2e^- \rightarrow S_2{}^{2-} + S_2{}^{2-}$

Stage 3 – Low plateau 2.1 V, shuttle effect.

Eq. 19 $S_3{}^{2-} + 2e^- \rightarrow S_2{}^{2-} + S^{2-}$

Stage 4 – Low plateau < 2.1 V, shuttle effect.

Eq. 20 $S_2{}^{2-} + 2e^- \rightarrow S^{2-} + S^{2-}$

In this context, defining these relevant species and the respective electrochemical techniques to characterize the Li-S battery is essential. The EIS proves to be very efficient for this type of analysis[176].

Electrochemical impedance spectroscopy

EIS is a technique that works in the frequency domain characterizing electrochemical systems to determine the individual contribution of the elements that constitute the electrode/electrolyte surface, specifically in electrochemical systems. The interface of the material under analysis can be interpreted through the combination of passive electrical elements such as: inductors, resistors and capacitors. The association of these elements can represent an equivalent circuit with physical sense. Such a circuit can be used to model the internal behavior of batteries in the frequency domain [177].

To perform the measurement, an initial disturbance is applied at a specific potential defined within the potential window determined by the galvastatic charge and discharge, for example. This initial sinusoidal disturbance ΔE (10 to 50 mV defined by the system as steady state, is compared with the sinusoidal current response of the electrode ΔI, measuring the phase difference Φ between the current and voltage elements and their respective frequencies (100kHz to 10mHz). The EIS analysis is considered the fundamental analysis for the characterization of Li-S batteries. There are several methods used to simulate equivalent circuits, such as the Randles model, as shown in **Figure 2.1**.

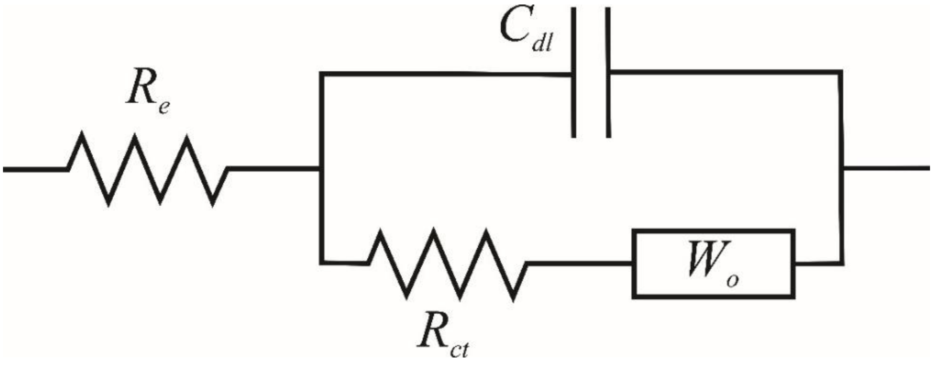

Figure 2.1 – Randles circuit.

In this circuit we have capacitive components (Q) that represent non-faradaic sources electrostatic process or electrical double layer capacitance (C_{dl}), as well as impedances such as series equivalent resistance (R_e), charge transfer resistance (R_{ct}). Complex elements such as Warburg (W_o) that are designed to simulate impedances caused by limitations in ion diffusion. Thus, the EIS technique helps in understanding the complexity of the pores present in the material. This technique allows the use of organic materials based on carbon for example (AC, CNT and rGO). Following this line of study, this work uses AC, as it promotes high chemical stability and charge transport when combined with S_8 sulfur and applied in Li-S batteries.

2.3 Electrochemical variables and techniques for Li-S battery characterization

2.3.1 State of charge (SoC)

This paragraph aims to exemplify some terminologies widely used in battery studies so that it is possible to understand the information presented in the results and discussion related to electrochemistry in this work. Battery SoC represented as a percentage (%) expresses the current battery capacity as a percentage of maximum capacity, ranging from 0 to 100%. The SoC is usually calculated using time-based integration to determine the change in battery capacity as a function of time. **Figure 2.2** shows the graph of charge and discharge of Li-S batteries as a function of SoC.

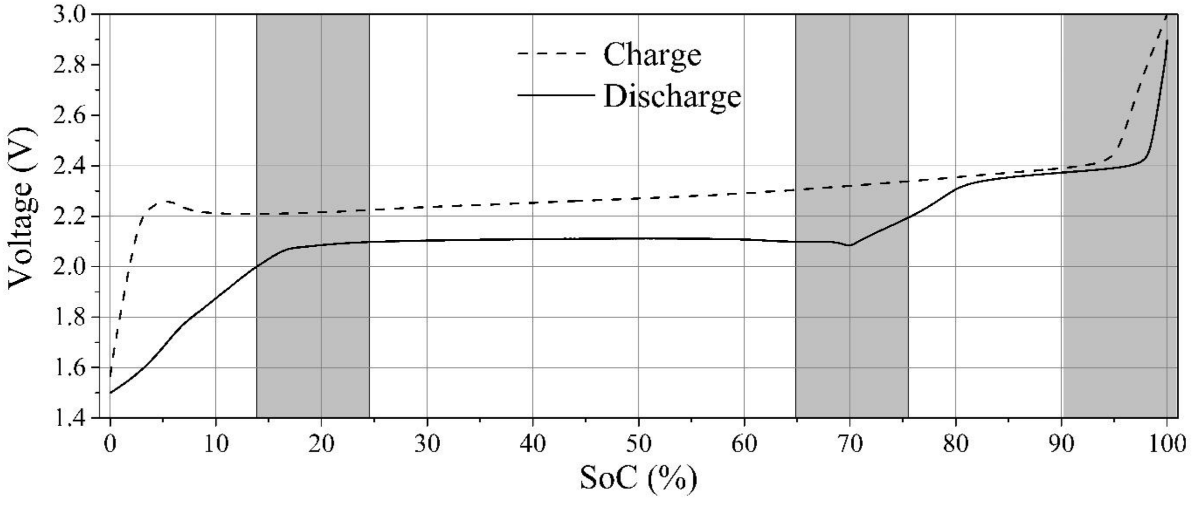

Figure 2.2 - Li-S battery charge and discharge graph with their transformation curves for the chemical species in evidence. Author's preliminary results.

2.3.2 Deep of discharge (DOD)

The depth of discharge (DOD) is also measured in terms of percentage (%) and is related to the battery capacity, but with a focus on observing how much it is discharged, that is, when the battery is around 80% of its capacity. discharge it is possible to consider that it is in a state of deep discharge

2.3.3 State of Health (SoH)

The battery health status is an indicator of its life status, *i.e.*, how much battery life has been used so far. To define this variable, it is possible to make a relationship between the type of battery chemistry, test temperature, C-rate, depth of discharge during use, among others.

2.3.4 Terminal Voltage (V)

The terminal voltage (V) is located between the polarization applied to the battery terminals as the charging process. The voltage at the terminals depends on the SOC and charging and discharging current.

2.3.5 Open Circuit Voltage (V)

The open circuit voltage (V) is located between the battery terminals with no applied load.

2.3.6 Internal Resistence

Internal battery resistence is generally different for charging and discharging, even more so when looking at chemical systems that are based on chemical intercalation or conversion associated with their internal potential generation process. Even more, this resistance depends a lot on your SoC. When the internal resistance increases, its efficiency decreases and this is due to the transformation of dissipated electrical energy in the form of heat. The more charged the battery is, the more energy is converted into heat.

Through this information, it is possible to understand the motivation and depth of the studies that follow. The Li-S battery presents a plateau during its discharge process that makes it impossible to evaluate its SoC just by looking at its potential. During the SoC of 20% - 70%, the same potential value is observed and therefore, it is not possible to determine in which SoC the system is within this region. In this way, in-depth studies of EIS are extremely important to understand which SoC our battery is located and how impedance values vary in sync with internal chemical processes. Associating this extremely effective EIS characterization technique can solve this problem and understand the behavior of our technology with the desired precision.

2.3.7 Technical specifications

- **Nominal voltage(V)**: The specified or reference battery voltage, sometimes referred to as the “normal” battery voltage.

- **Cutt off**: The minimum allowable voltage. This voltage generally defines the “empty” state of the battery, reached in the discharge process, in which the battery is completely discharged. We usually also call it the working voltage window (WVW) limit, which can vary from battery to battery, considering the associated chemical processes and components such as electrolytes and electrodes.

- **C-rate:** When describing a battery, a discharge current is usually expressed numerically as a multiple of "C", *i.e*., also known as a C-rate to normalize battery capacity, which often varies greatly between each system. A multiplicity of size C is a measure of the current at which the battery is discharged, referring to the maximum capacity. The 1C rate means that the discharge current will charge a fully charged battery within 1 h. For a 500Ah battery, this discharge time for 1C corresponds to an applied discharge current of 500A.

- **Capacity or Nominal Capacity:** A measure of the charge stored by a battery (Ah for a specified C-rate value).

- **Nominal energy or energy:** The “capacity” of the battery, or the number of hours available when the battery is discharged at the specified discharge current (corresponding to the C-number value) of 100% from SoC to cut off. Energy is calculated by multiplying the discharge power (in watts) by the discharge time (in hours). Like capacity, power decreases with increasing current C.

- **Life, number of cycles for a specified DOD**: Number of discharge cycles. Battery charging may occur before it continues to meet specific performance criteria. Service life is estimated for certain charging and discharging conditions. Actual battery life depends on the speed and depth of cycles and other conditions such as temperature and humidity. The higher the DOD, the shorter the lifespan.

- **Specific energy (Wh/kg):** Nominal battery energy per unit of mass, sometimes referred to as energy density by weight. Proper power is characterized by chemical configuration adjustment and battery packaging. Determines the weight of the battery needed to reach a given range of electrical current.

- **Specific power (W/kg**): Specific power or gravimetric energy density **i**s a measure of how much energy a battery contains in comparison to its weight. This information is very import and can be used in ragone plot.

With these definitions made, we can proceed to understand Li-S batteries better. To this end, we set up a simple battery to apply this knowledge and improve our understanding of the device

3 Electrochemical properties and the diffusion process as a function of state-of-charge for lithium-sulfur batteries with activated carbon cathode

3.1 Experimental section

3.1.1 Preparation of the Li-S cathode material and cell assembly

The Li:S cathode material was prepared as follows: First, 8 mL of *N*-methyl-2-pyrrolidone (NMP, Sigma Aldrich) was stirred at 60 °C for 30 min. At the same time, the polyvinylidene fluoride (PVDF, Sigma Aldrich) used as a binder was added in small quantities until the dissolution of PVDF. After that, carbon black (CB, Cabot XC72R) was added to improve the conductivity. Afterward, a 60% (*w/w*) mixture of activated carbon (AC) and sulfur powder (S_8, Sigma Aldrich), denoted as AC:S, was added in the mixture to obtain a mass ratio of 10:10:80 for PVDF, CB, and AC:S, respectively. The mixture was then stirred for 24 h and sonicated for 15 min three times. The composite material was coated on the current collector (A_G = 1.93 cm^2) and dried overnight at 60°C. Finally, the electrode samples were heated for 1.0 h at 150°C to melt and evaporate the sulfur excess. Each AC:S composite electrode had a nominal mass of 0.200 mg_{sulfur} cm^{-2}. All electrode samples were assembled using a glass filter membrane (GF50/A) (*e.g.*, Ø = 25 ± 0.5 mm) as the separator for the anode and cathode. The anode utilized was the Lithium metallic disc, with 14mm of diameter. The membrane was soaked with a 1.0 M LiTFSI solution containing 1% (*w/w*) of $LiNO_3$, where the solvent was a 1:1 (*v/v*) mixture of *1,3*-dioxolane (DOL) and *1,2*-dimethoxyethane (DME). Three electrochemical cells were assembled and used as described in the following sections. **Figure 3.0** depicts the fabrication process.

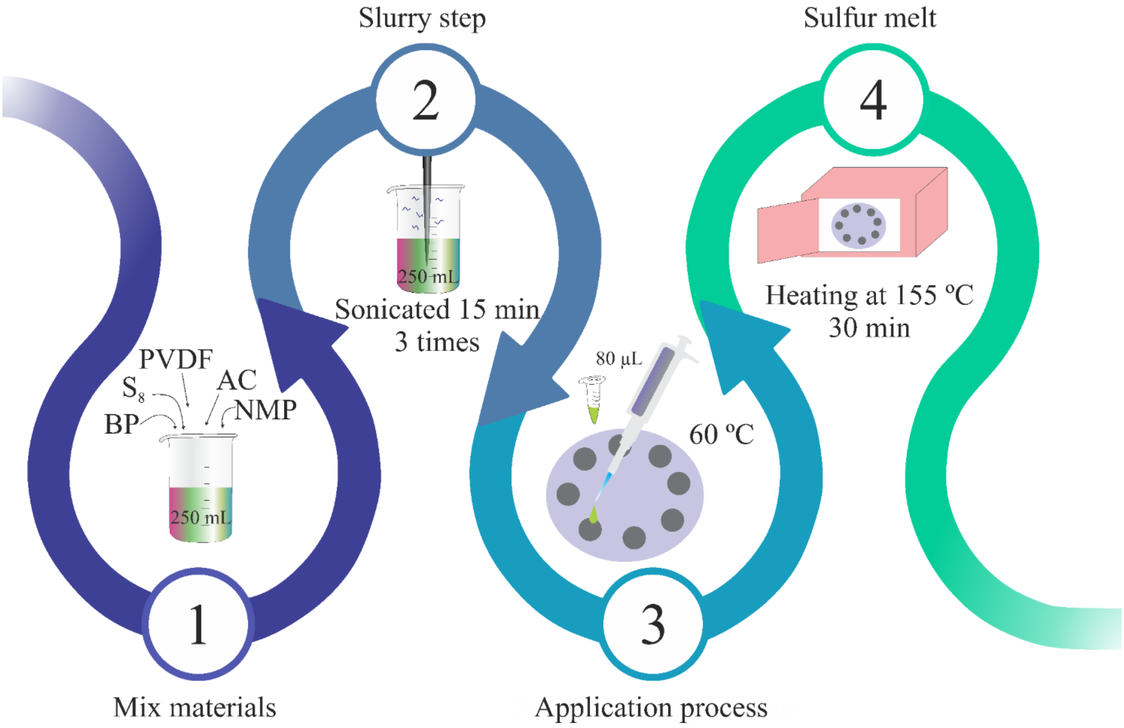

Figure 3.0 - Scheme representing the fabrication of the AC:S composite electrodes.

3.1.2 Ex-situ materials characterization

The surface morphology of the AC:S composite material was analyzed by scanning electron microscopy (SEM) using a model Quattro ESEM microscope from Thermo Scientific™. The X-ray photoelectron spectrometry (XPS) analysis was carried out using Thermo Scientific equipment. The AC:S composite was also analyzed using a Renishaw inVia Raman spectrometer with a 785-nm wavelength laser. Data were acquired in the first-order region located in the 100 to 2200 cm^{-1} wavenumber interval to evidence the spectroscopic signals exhibited by carbon and sulfur. Raman experiments were accomplished using 30 s and 2 accumulations with a laser power of 10 mW. XPS and Raman data were deconvoluted using Gaussian and Lorentzian functions with the aid of Fityk® software. These findings were normalized in relation to the most intense peak.

3.1.3 Electrochemical measurements

Electrochemical cells (battery prototypes) were charged and discharged using two consecutive cycles in the range of 1.5 to 3.0 V. Although cell capacity is unknown at this initial stage, and it can only be roughly estimated, a small current of 50 µA was used in charge-discharge experiments so that ohmic losses are negligible. This first experiment revealed the (*i*) initial capacity (which will be later used for C-rate calculations), the (*ii*) voltage *vs*. SoC curve, and the (*iii*) initial coulombic efficiency for each cell.

3.1.4 Charge and discharge studies

The electrochemical response of the AC:S cathode under cyclic charge-discharge conditions was studied using the cyclic voltammetry (CV) at 0.1 mV s^{-1} and the galvanostatic charge-discharge (GCD) techniques. The latter was carried out at different C-rates in the range of 0.06 to 1.1 C covering the WVW of 1.5 to 3.0 V using the Potential Limitation (GCPL) method. A model BCS-815 potentiostat from BioLogic® was used throughout.

3.1.5 Electrochemical impedance spectroscopy (EIS) experiments

Due to a Nernstian behavior, the charge-discharge curves (*U vs. I*) exhibited by different secondary (rechargeable) batteries are commonly characterized by *voltage plateaux*. In this sense, the galvanostatic EIS (gEIS) experiments are commonly used for studying batteries instead of the potentiostatic (pEIS) case. In the former case, denoted as '*current control*' (*e.g.*, $I_{\text{a.c.}} = \delta I \text{sen}(2\pi f)$, where δI is the wave amplitude), the application of *a.c.* low-amplitude currents during the frequency scan prevents significant changes in SoC values.

The different input parameters used in the impedance experiments were previously adjusted to ensure reproducible gEIS findings. A frequency range of 10 kHz to 10 mHz was swept by recording six points per decade. To ensure linearity on impedance response, a small sinusoidal amplitude of 100 µA without a *d.c.* bias ($I_{\text{d.c.}} = 0$) was applied. As a result, the average *d.c.* current response was practically zero in the gEIS experiments with virtually no change on SoC. The gEIS spectra were initially measured for a 100% SoC. Afterward, a galvanostatic discharge at 50 µA for 2.0 h was used to change the SoC value, meaning a C/40 rate with a 0.1-mAh capacity discharge. A 15-min waiting time was adopted after each galvanostatic experiment to ensure reproducible impedance findings. Each consecutive galvanostatic discharge at 0.1 mAh corresponded to a 5% SoC decrease. The gEIS findings were obtained at regular SoC intervals covering the 0 to 100% interval.

Conversely, the same procedure was applied when the galvanostatic charged experiments were used to recover the 100% SoC condition. Impedance data were analyzed using ZView® software from Scribner Associates Inc.

3.1.6 Self-discharge, relaxation time, and sample aging

Evaluation of cell self-discharge was performed following the open-circuit voltage (OCV) as a function of the elapsed time (mV h^{-1}) for a fully charged cell. In this sense, the cell was initially charged to the upper limit voltage of 3.0 V. Afterward, OCV was monitored every

60 s or whenever the voltage varied more than 1 mV. The cell rest period was 1500 h at 24 ± 1°C. Later on, the OCV data in intervals of 50 and 100 mV were compared with the *U vs. SoC* curve obtained previously for the cell under test, and the self-discharge current was evaluated. Since initial cell capacity is known and considering that the cell was not completely discharged after the rest period, the changes in OCV were followed after galvanostatic discharge experiments until the lower voltage limit of 1.5 V was achieved so that the remaining capacity could be determined. This procedure served as a second estimation criterion for measuring the self-discharge current. From the GCD experiment, the cell was fully charged and then fully discharged at a C/40-rate. Then, capacity and coulombic efficiency were reassessed after a controlled resting time.

3.2. Results of experimental analisys

3.2.1 Morphological, physical, and chemical characterization of the composite material

SEM analysis revealed that the surface morphology of the AC:S composite presents the typical characteristics found for AC particles. **Figure 3.1 (a & b)** shows the SEM micrographs evidencing the AC particles decorated with sulfur and forming clusters with average lengths of *ca*. ~10 µm. The energy dispersive X-ray spectrometry (EDS) was employed to confirm the presence of sulfur in the carbon-based samples. The EDS elemental mapping is presented in **Figure 3.1 (c & d)**. As seen, there is a uniform distribution of S and C elements on the surface of the composite sample. Moreover, other chemical species (impurities) were not detected at a level corresponding to *ca*. 0.1 at.%.

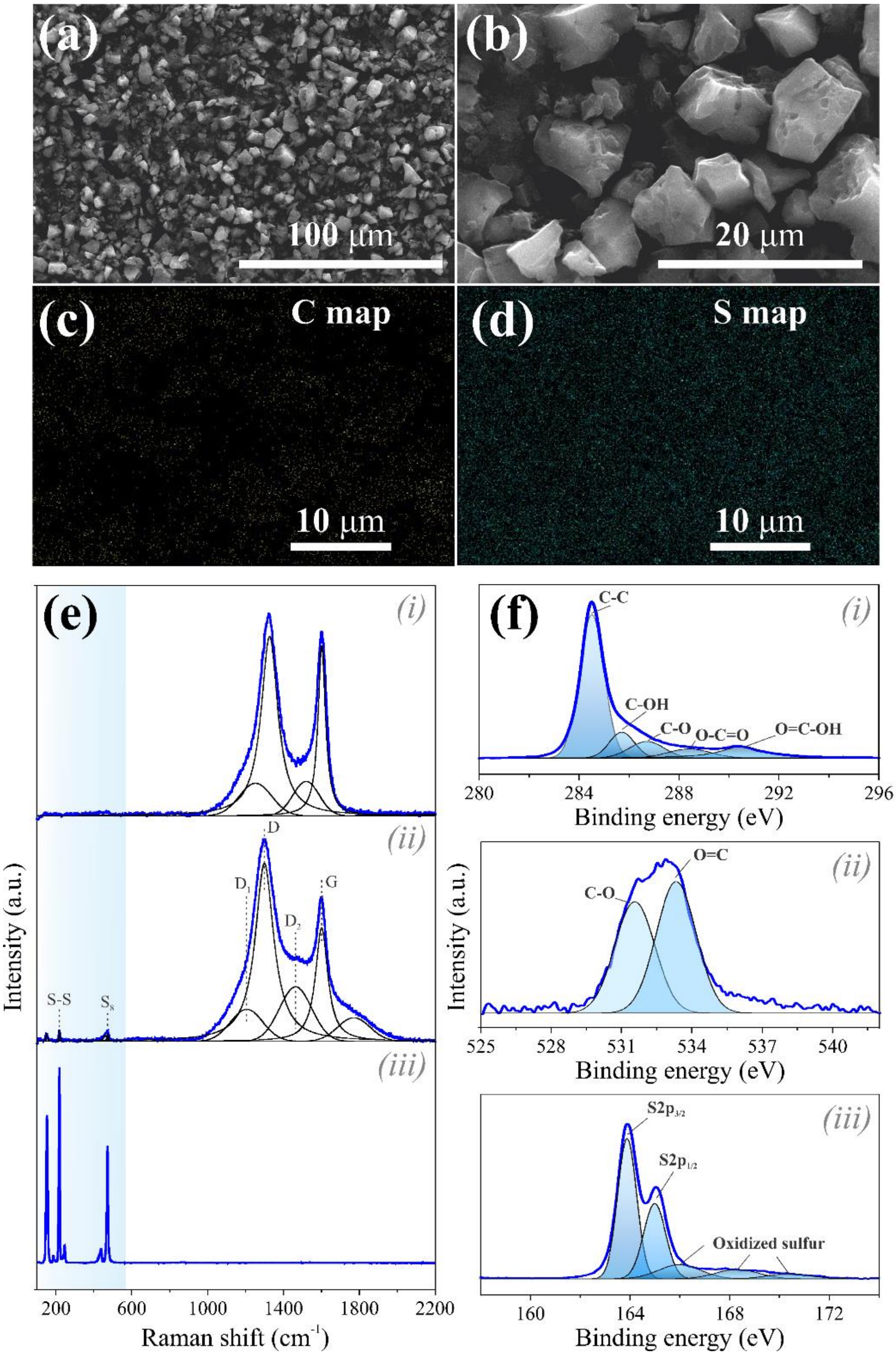

Figure 3.1. SEM micrographs for the AC:S composite at (**a**) low and (**b**) high magnifications. EDS mapping for (**c**) sulfur and (**d**) carbon in the composite. Mapping was obtained for the same region showed in (**b**). Raman spectra (**e**) for (***i***) AC, (***ii***) AC:S, and (***iii***) pure sulfur powder. XPS spectra (**f**) for AC:S referring to the (***i***) C 1s, (***ii***) O 1s, and (***iii***) S 2p binding energies.

Figure 3.1 (e) shows a comparison of Raman spectra obtained for **(*i*)** AC, **(*ii*)** S, and **(*iii*)** AC:S composite, respectively. These spectra elucidate that AC:S combines both spectra

AC and S chemical species, confirming that the synthesis processes did not remove the AC or S intrinsic features. Spectrum ***(i)*** presents two Raman bands at 1326 and 1601 cm^{-1} assigned to the D- and G-bands related to in-plane vibration modes [178]. The first one is a defect-induced band. It is an intervalley double resonance process around the K and K' points in the first Brillouin zone for graphene-like materials. The latter also occurs at the Brillouin zone center but is related to the E_{2g} Raman active phonon modes [179–181]. Besides these prominent bands, bands at 1200 and 1500 cm^{-1} denoted as D_1 & D_2 are characteristic of amorphous carbons. The D_1-band is attributed to the stretching vibrations of sp^2-sp^3 bonds. In the case of D_2, it is related to functional groups bonded on carbon surfaces [36].

The Raman spectrum of **Figure. 3.1 e (ii)** covering the 100 to 600 cm^{-1} wavenumber interval presents four prominent bands centered at 151, 219, 460, and 473 cm^{-1}. The band at 151 cm^{-1} was assigned to the asymmetric S-S bending vibration mode. At the same time, the band at 219 cm^{-1} is assigned to the symmetric S-S vibration bending mode. The band at 473 cm^{-1} represents S-S stretching vibration mode for an S_8 ring structure [182]. The less pronounced band at 440 cm^{-1} also corresponds to the S-S stretching vibration mode [58-60]. These findings confirmed the effectiveness of the synthesis process, *i.e.*, the annealing treatment resulted in the incorporation of sulfur particles into the AC clusters. The Raman spectrum obtained for the composite ***(iii)*** revealed the major chemical characteristics exhibited by the individual materials (AC and S) were preserved in the annealed sample. As a result, the composite material is a promising candidate for use as a cathode in Li-S batteries (see further discussion).

The XPS technique was employed to assess the presence in the composite of different elements and their chemical states. **Figure 3.1 (f)** shows the C 1s, O 1s, and S 2p binding energy regions and the deconvoluted spectra. The C 1s region was resolved into five peaks. The prominent peak at 284.5 eV was attributed to C=C bond, which confirms the presence of σ and π bonds. Such findings are typical of sp^2 hybridization and agree with the previously discussed Raman results. Furthermore, the peak at 285.7 eV is characteristic of C-OH bond, while the other at 286.7 eV is related to C-O bond [186–188]. The two peaks in the higher energy regions at 288.4 eV and 290.5 eV were assigned to carbon bonded with oxygen species, such as C-O, O-C=O, and O=C-OH [186–188]. The O 1s region was resolved into two peaks related to carbonyl groups, *i.e.*, the peak centered at 531.5 eV is characteristic of the C-O bond, while that at 533.3 eV is due to O=C group [43,71,189]. The S 2p region was resolved into five peaks. There are two prominent peaks at 163.9 eV and 165.0 eV, which, in principle, are related to S

$2p_{3/2}$ and S $2p_{1/2}$ energies for the -C-S-C- covalent bond. However, these peaks can also be ascribed to the C-S and S-S bonds, respectively [190–192]. Additionally, the peaks at 166.0 eV and 168.3 eV are consistent with the presence of -C-S(O)$_2$-C- sulfone bridges [193,194]. Hence, it is possible to verify the existence of connections and chemical interactions between sulfur and the carbon host material [32,195].

The carbon, sulfur, and oxygen contents present in the composite were 83%, 14%, and 3%, respectively. The relative composition found for the AC:S material agreed with the preparation method conditions. According to the Raman and XPS findings, the AC:S composite is based on an oxidized carbon platform containing different functional groups (*e.g.*, ketone, carbonyl, and quinone) where sulfur species were anchored.

3.3 Electrochemical results

The elementary processes occurring during the charge-discharge processes in Li-S batteries are quite complex. **Figure 3.2 (a)** illustrates the cyclic voltammetry (CV) at 0.1 mV s^{-1}, evidencing two oxidation peaks (marked as 1 and 2) in the 2.3–2.4 V interval that correspond to the cell charging process. According to the literature, lower-order polysulfides (*e.g.*, Li_2S_2) transform into higher-order polysulfides (*e.g.*, Li_2S_6 and Li_2S_8) during oxidation. Also, one has the reversible formation of sulfur in the solid-state [154]. At the same time, the reduction peak (marked as 3) at ≈ 2.3–2.4 V is due to the first solid-state reduction of the S_8 molecule, which is then converted to a liquid state with the formation of linear polysulfide chains (*e.g.*, Li_2S_x, where $8 \geq x \geq 4$) [27, 75, 76]. This phase is characterized by increased solubility of sulfur species and a low viscosity.

It is proposed that the peak (marked as 4) at 2.05 V results from the reduction of high-order polysulfides into intermediary polysulfides (*e.g.*, Li_2S_x, where $4 \geq x \geq 2$), indicating the feasibility of multiple faradaic reactions involving different sulfur species in the presence of Li-ions [3]. The redox band (5) verified at *ca*. 1.7–1.8 V is commonly assigned to the formation of low-order polysulfides, *i.e.*, it is possible to observe the formation of insoluble species during the discharge process. As a result, one has the formation of a two-phase solution with higher viscosity denoted as catholyte [154].

Figure 3.2 (b) shows a galvanostatic discharge profile obtained with 0.06 C, where the plateaux at 2.4, 2.2, and 1.8 V correspond to the reductions Li_2S_8 to Li_2S_6, Li_2S_6 to Li_2S_4, and Li_2S_4 to Li_2S_2, respectively [151]. As can be verified, the CV peaks are the equivalent electrochemical signals verified as plateaux in the galvanostatic discharge experiments. **Figure**

3.2 (c) presents the charge and discharge voltage profiles obtained for different current densities. The voltage-capacity profiles are very similar during the charging process at constant current due to long-chain polysulfides formation. The discharge curves follow the same path, and all profiles present similar plateaux of reducing polysulfides, as discussed in CV results. Additionally, it is possible to observe flatter plateaux, suggesting a uniform deposition of Li_2S with few activation kinetic barriers [197]. **Figure 3.2 (d)** shows the achieved cell capacity normalized per gram of sulfur as a function of the discharge current density. Experiments indicated a maximum capacity of 1044 mAh g^{-1} with a discharge charge of 0.06 C when the entire sulfur mass per electrode area of ≈ 2 mg_{sulfur} cm^{-2} is considered. The cathode performance was evaluated using this normalization by gradually increasing the charge from 0.06 to 1.1 C. Each charge is applied during five consecutive charge-discharge cycles to ensure reproducible conditions. These experiments are useful to observe the kinetics and stability of the cathode and provide means for clarifying the operation limits of the cell.

From data included in the articles cited in **Table 1**, it is possible to observe that the present AC:S cathode material showed the greatest electrochemical stability during the first three *C*-step tests. The capacity is inversely proportional to the applied discharge current density. Thus, the *C*-steps of 0.06, 0.1, 0.2, 0.5, and 1.1 C resulted in the capacities of 1044, 939, 903, 692, and 566 mAh g^{-1}, respectively. After the current density tests, the discharge current was reduced to 0.5 C to evaluate the presence of hysteresis, which was practically absent. The achieved capacity of 696 mAh g^{-1} is very close to the previously verified capacity of 0.5 C (= 692 mAh g^{-1}).

Figure 3.2 (e) shows the behavior of the AC:S-based cell during the lifecycle test performed at 0.5 C. The capacity curve is shown along with the coulombic efficiency curve as a function of the number of galvanostatic charge-discharge cycles. Regarding the capacity curves, there are two main regions deserving discussion. First, from 1st to about 150th cycle, the curve is characterized by an almost linear capacity reduction from nearly 800 to 200 mAh g^{-1}. Therefore, an equivalent capacity loss of 0.50% per cycle was verified. Second, from 151st to 300th cycle, the curve exhibited a less pronounced capacity reduction rate of 0.57 mAh g^{-1} $cycle^{-1}$ (= 0.071% per cycle). It is interesting to observe that while capacity fades during the lifecycle test, the coulombic efficiency increased from *ca.*78% to 99%. The possible cause of this behavior can be explained by a 'deactivation process' occurring at the cathode. In this sense, at the onset, the capacity is utterly available so that its maximum is observed for the 1st cycle, while the presence of a deactivation process is practically absent.

However, the self-discharging process verified for the tested Li-S cells was considerably higher than the existing data in the literature [198]. At the same time, the charge-transfer resistance was considerably high during the discharging process. The first effect contributes to a loss of the stored energy during and after the galvanostatic discharge experiment. At the same time, the second effect contributes to ohmic losses during the discharge process. As a result, these different effects can result in a reduced coulombic efficiency.

As the galvanostatic charge-discharge cycles increase, the cathode deactivation process becomes more pronounced, and a linear capacity reduction can be observed. Cathode deactivation also leads to a higher equivalent series resistance (ESR). At the same time, the self-discharge current is decreased. Since the self-discharge becomes gradually less significant, almost all energy stored during the charging process can be extracted in the consecutive discharging experiment. As a result, the coulombic efficiency can increase as a function of the GCD cycles, as verified in **Figure 3.2 (e)**.

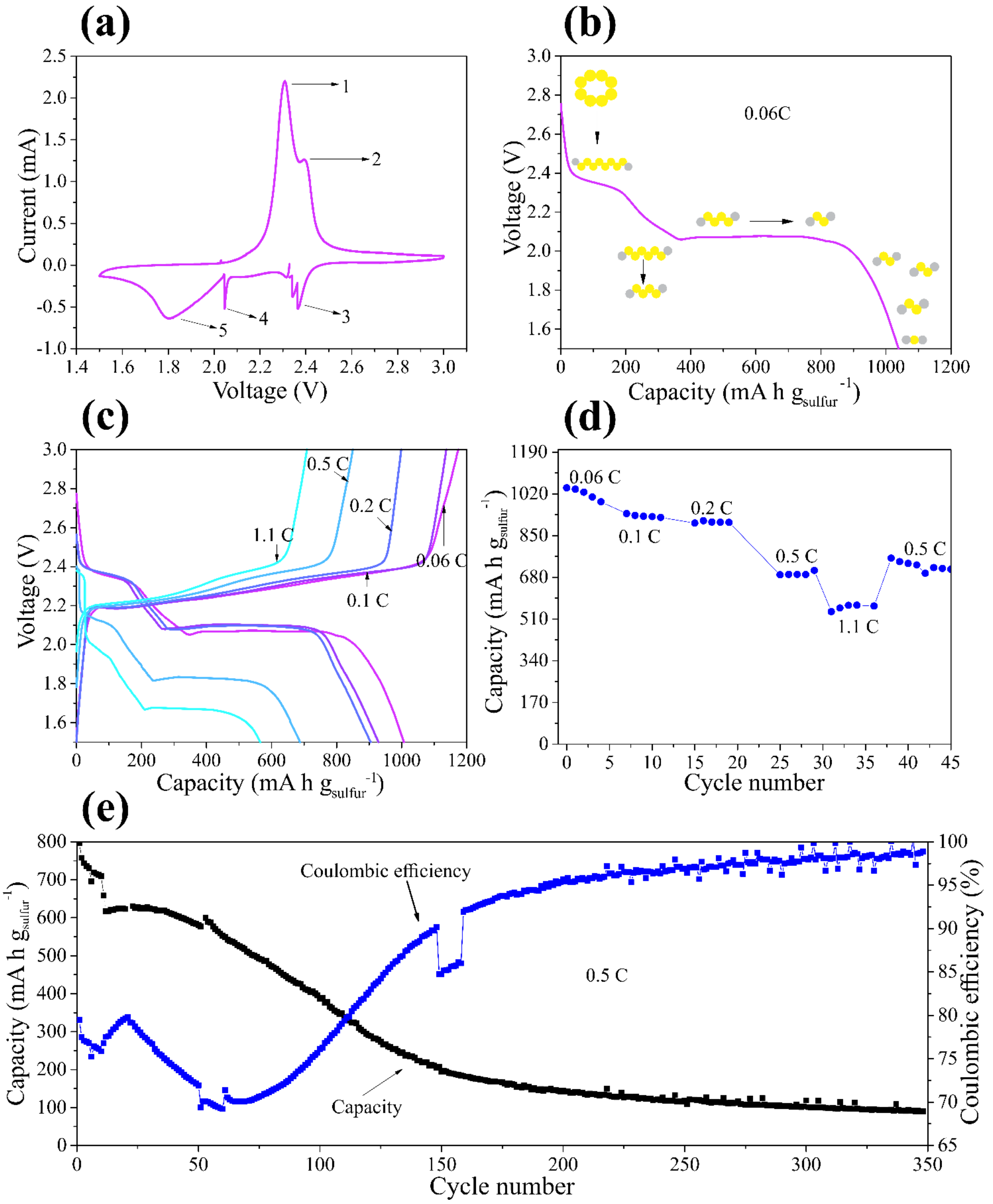

Figure 3.2 - Electrochemical findings obtained for the Li-S-based cell using the CV and GCD techniques: (**a**) cyclic voltammograms at 0.1 mV s^{-1}; (**b**) first discharge at 20 mA g^{-1}; (**c**) cell capacity at different *C*-rates; (**d**) galvanostatic charge-discharge profiles at different *C*-rates; (**e**) coulombic efficiency and specific capacity during the cyclability test. Cell conditions: AC:S composite used as the cathode and Li^0-foil used as the anode.

3.3.1 Electrochemical impedance spectroscopy study

Figure 3.3 shows the (**a**) charge-discharge curves and (**b-c**) gEIS data as a function of SoC. The initial discharge capacity was 2.15 mAh. During the discharge, the transition from S_8 to Li_2S_8 occurs in the region from 100% to 80% SoC, while the reduction from Li_2S_8 to Li_2S_6 occurs from 80% to 70% SoC. From 70% until 15%, the sulfur species of middle-order like

Li_2S_6 are converted to Li_2S_4. From 15% until 0%, the final reduction to Li_2S_2 and Li_2S takes place.

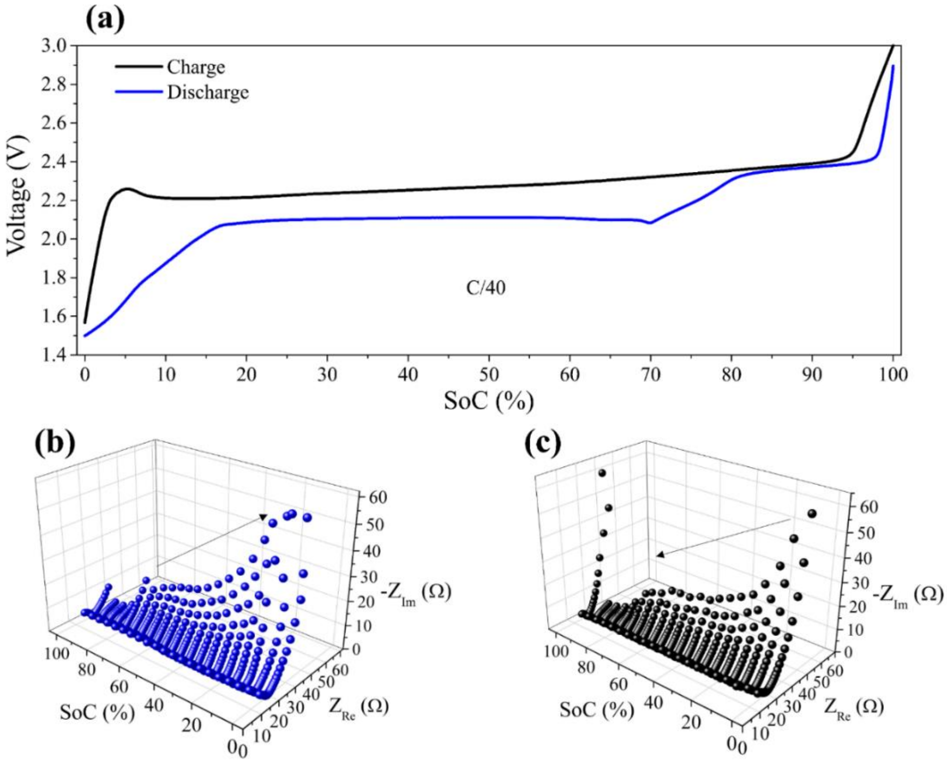

Figure 3.3 - (**a**) Charge-discharge profiles compared for different SoC values of Li-S battery at a current density referred to C/40. Complex-plane impedance plot obtained for the discharge (**b**) and charge (**c**) process.

3.3.2 Quantitative analysis of the impedance data

Figure 3.4 shows an equivalent electric circuit for the fitting/simulation of the *overall cell impedance* using the complex nonlinear least-squares (CNLS) method. Based on the literature [81, 82], the following circuit elements were considered in this work: (*i*) R_e is the equivalent series resistance (*e.g.*, electrolyte, current collectors, and cell connections); (*ii*) C_{dl} is the overall electrical double-layer capacitance verified for the two-electrode cell; (*iii*) R_{ct} is the overall charge-transfer resistance at the different electrodes (anode and cathode); W_o is the open Warburg element representing the finite (restricted) Fickian diffusion of the electroactive (redox) species.

Assuming a complete separation of the capacitive (C_{dl}) and faradaic ($Z_f \equiv R_{ct}W_o$) impedances, the above elements can be lumped to yield the equivalent circuit model. It is worth mentioning that the well-known *Randles-Ershler* circuit involves the presence of the conventional Warburg (W) due to semi-infinite linear diffusion instead of an open Warburg (W_o) representing finite linear diffusion [200].

The analysis comprising the simulation of the impedance findings obtained for a 50%-SoC during the charging process illustrates the quantitative EIS study using the equivalent circuit discussed above (see **Figure 3.4**). As seen, the experimental data obtained for the 10 kHz to 10 mHz range permitted to discriminate the *charge-transfer resistance* (faradaic reaction) occurring in parallel to the electrical double-layer charging process and the finite linear diffusion of the redox species. In all cases, low chi-square values confirmed the excellent quality of the CNLS fitting procedure (*e.g.*, $\chi^2 \leq 2.3 \times 10^{-4}$).

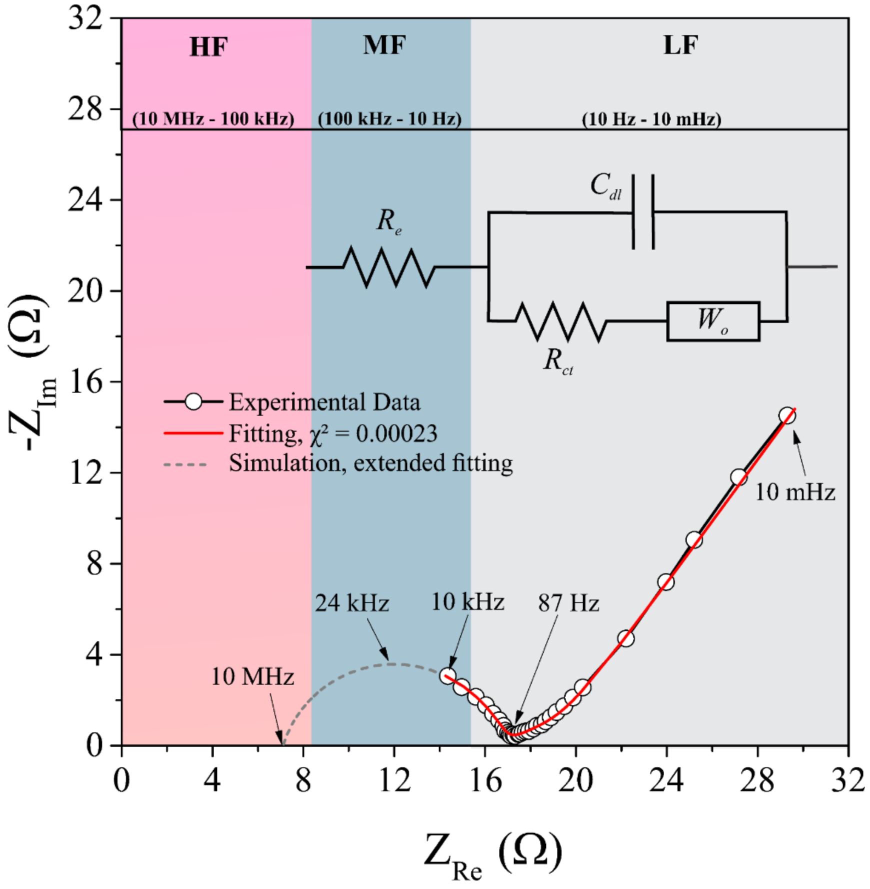

Figure 3.4 The equivalent circuit used in the fitting-simulation procedure and the impedance for the charging process at 50% SoC containing the experimental and simulation findings.

Figure 3.5 (a & b) shows the different circuit parameters as a function of the voltage and SoC values. As previously mentioned in this work, the R_e is directly related to SoC. The electrolyte characteristics (*e.g.*, conductivity, viscosity, and composition) are affected by SoC because the latter modifies the electrolyte composition during conversion of different soluble sulfur species, *i.e.*, it is expected that some soluble polysulfides are formed. At the same time, S-based solid products formed during the faradaic reaction are partially dissolved during changes in SoC values for both charging and discharging processes. Therefore, the electrolyte resistance (a component of *ESR*) is not constant during the charge and discharge. These findings bring exciting considerations about the Ragone plots since they depend on R_e [82]. In this sense, as R_e changes as a function of SoC, it is unclear what is the best SoC value to construct a Ragone plot.

Regarding the battery discharge, **Figure 3.5 (a)** shows that at 100% SoC, the overall ohmic resistance is relatively low (6.59 Ω cm^2), compared to the average maximum values of *ca*. 17.95 Ω cm^2. It can be suspected that the battery still shows a sulfur predominance with the formation of insoluble material in the cathode. As a result, the electrolyte solution is unaffected by the sulfur species at the onset of the discharging process. After that, the reduction reaction takes place, increasing the electrolyte resistance. The second point (95% SoC) in **Figure 3.5 (a)** showed a considerable increase in internal resistance (16.0 Ω cm^2) at ≈ 2.4 V. At this stage, the first voltage plateau for sulfur reduction is was suggest with the release of high-order LPS (Li_2S_8) in the electrolyte. As a result, the viscosity increased concomitantly with the electrolyte resistance [170,201]. After the intermediate reduction stages characterized by a plateau at ≈ 2.1 V, the voltage dropped almost linearly for SoC values lower than 20%. A sudden decrease in R_e values accompanies this voltage behavior due to the formation of insoluble lower-order lithium sulfides (*e.g.*, Li_2S_2 and Li_2S) [202].

The same behavior was verified during charging since from 0 to 10% SoC, the R_e increased because the lower-order sulfur species were oxidized with the formation of larger molecular weight sulfur compounds. The latter are soluble in the electrolyte, increasing its viscosity. For the discharge and the charge processes (0% SoC), different resistance values of 1.47 and 8.88 Ω cm^2 were verified, respectively. The higher resistance associated with the discharge can be ascribed to the existence of Li_2S_2 and Li_2S species together with intermediate order polysulfides in the composition range of Li_2S_4 to Li_2S_6. According to the literature [203], lower/intermediate order polysulfides deposition occurs in the cathode and separator because they are not reversibly transformed into oxidizable species during the charging process, a phenomenon called the '*shuttle effect*' [203].

A similarity is verified in the behavior of the experimental findings showed in **Figure 3.5 (a) & (d)**. However, an interesting point to highlight is that R_e values at 100% SoC are different, *i.e.*, they do not return to the initial value. A resistance increase is observed after the charging and discharging process is finished. Initially, a R_e value of 6.59 Ω cm^2 is observed at 100% SoC. After the discharge-charge cycle is completed, the resistance increases to 13.8 Ω cm^2 at 100% SoC. This behavior may be related to the LPS present in the electrolyte

[170,202,204]. From a practical viewpoint, a R_e increase can be used to evaluate battery aging and SoC control using appropriate management systems.

3.3.3 Analysis of the impedance behavior at intermediate and low frequency regions

During the discharge, at 100% SoC, it is observed in **Figure 3.5 (c)** the highest R_{ct} value of 29.0 Ω cm^2 that indicates the lowest electrocatalytic activity for electron transfer at the cathode and anode [205]. As seen, except for discharges between 0–20% SoC, the average R_{ct} values (≈ 13–19 Ω cm^2) for both charging (anodic) and discharging (cathodic) processes are similar. The main difference being the resistance at 100% SoC, which for the discharge and charge are 29.2 Ω cm^2 and 17.7 Ω cm^2, respectively. This behavior can be associated with better charge transfer when accessing the cathode pore after most of the solid-state sulfur (S_8) has been consumed during the discharge. Thus, the porous carbon structure has more spaces to promote the oxidation reaction of polysulfides and the absence of the S_8 species, which has very high insulating characteristics. These findings indicate the electrocatalytic activity is similar to the redox processes occurring at the anode and cathode. Therefore, deep discharges can be not beneficial for the battery performance since more energy is dissipated as heat due to the formation of a pronounced activation barrier for electron transfer when SoC is drastically reduced. In this experiment the temperature was controlled and adjusted for room temperature, nearly 25 ºC.

Figures 3.4 (b) and **(c)** show a slope change at intermediate frequencies in the complex-plane plots. From the theoretical viewpoint, this impedance behavior indicates that a diffusion mass-transport in a finite barrier, represented by the *Open Warburg Impedance* (W_o) or *Finite Space Warburg* (FSW) ($\varphi \approx -45°$), is substituted by a pseudocapacitive behavior ($\varphi \approx -90°$) due to the total consumption of the active redox species when $\omega \rightarrow 0$. In other words, the electrode/electrolyte interface becomes *blocked for electron transfer* at very low frequencies called the *d.c.* limit. In fact, the mass transfer impedance shows the characteristic straight line with almost unitary slope at medium frequencies since the penetration length of the *a.c.* signal is smaller compared to the diffusion layer thickness, and at very low frequencies, the imaginary impedance tends to infinity as a *d.c.* current is not permitted to flow in the electrode system, *i.e.*, at low frequencies, the observed *pseudocapacitance* is given by $C_W = l/\sigma D^{1/2}$, where l is the effective diffusion length, and σ and D are the Warburg and diffusion coefficients, respectively (see futher discussion) [200].

The pseudocapacitance (C_{W}) due to the diffusion process under ideal (Fickian) linear conditions, instead of an electrostatic capacitance exhibited by the electrical double-layer (C_{dl}), was represented by a CPE to consider the anomalous properties intrinsic to solid electrodes. In this sense, $Z_{\mathrm{cpe(W)}} = 1/Y_{\mathrm{o(w)}}(2\pi f)^n$, where $Y_{\mathrm{o(W)}} \cong C_{\mathrm{W}}$ only when $n \cong 1$. In the limit case described above, when $\omega \rightarrow 0$, the $Y_{\mathrm{o(W)}}$ appears in parallel to C_{dl} and, therefore, the *overall capacitance* is $C = C_{\mathrm{W}} + C_{\mathrm{dl}}$ or, more precisely considering the dispersive effects, one has $Y_0 = Y_{0\mathrm{(dl)}} + Y_{\mathrm{o(W)}}$. From these considerations, one has in the present study the *Generalized Warburg Element* (GWE) accounting for the nonuniform diffusion or multiple paths existing in the system (*e.g.*, tortuosity effects in solid medium).

Experimental values for C_{dl} lower than *ca*. 0.5–1 μF cm^{-2} are commonly meaningless for carbon-based electrode materials in different electrolytes, especially in organic media where a reduced dielectric constant is verified and higher C_{dl} values can be found (*e.g.*, ≈ 3–5 μF cm^{-2}) [18]. Thus, it can be concluded that some absolute values in **Figure 3.5 (c & f)** obtained for the *coin cell* (*e.g.*, cathode and anode disposed of in series) can be an apparent artifact incurred by measuring the overall impedance behavior of a *two-electrode device*. In this sense, the *particular interface* (anode/electrolyte or cathode/electrolyte) that exhibits the *lowest overall capacitance* governs the experimental capacitance measured in practice. From these considerations, the strong capacitance reduction verified at extreme SoC values in **Figure 3.5** can be due to a decrease in the electrochemically active surface area caused by deposition of sulfur species on the cathode, resulting in very low exposed area to the organic electrolyte. It is worth mentioning that most capacitance data given in the literature is obtained using *three-electrode cells*, *i.e.*, the impedance data correspond to a *single interface* whose potential is monitored against a particular voltage benchmark or reference electrode [18].

It is relevant to mention that in practical applications, even for coin cells, a *two-electrode device* will be used. The traditional prediction or calculation of SoC is based on open circuit voltage observation or coulombic counting, both measurable without a third electrode. Although the later one can be applied to any electrochemical storage device, it is only reliable if the cell's self-discharge current is negligible, which is not the case (see further discussion on self-discharge results). On the other hand, since Li-S presents well-defined plateaus in which the open circuit voltage varies just slightly, voltage observation provides a poor method for accurate SoC calculation. Considering the discharge results for the parameters as functions of SoC in **Figure 3.5**, while R_e and R_{ct} show reduced variation from 20 to 95% SoC making a curve fitting correlating resistance and SoC unlikely, C_{dl} behavior exibits a more pronounced variation in the same SoC range. In the 0 to 10%, C_{dl} is very small and not practically useful, while R_e and R_{ct} present pronounced and linear variation. The feasibility of a SoC prediction or calculation based on EIS-extracted parameters, measurable in two-electrode devices and based on the combined behaviors of R_e, R_{ct} and C_{dl} all along the 0 to 100% SoC range is an insight here proposed and yet to be investigated. State-of-health computation may as well follow from this insight.

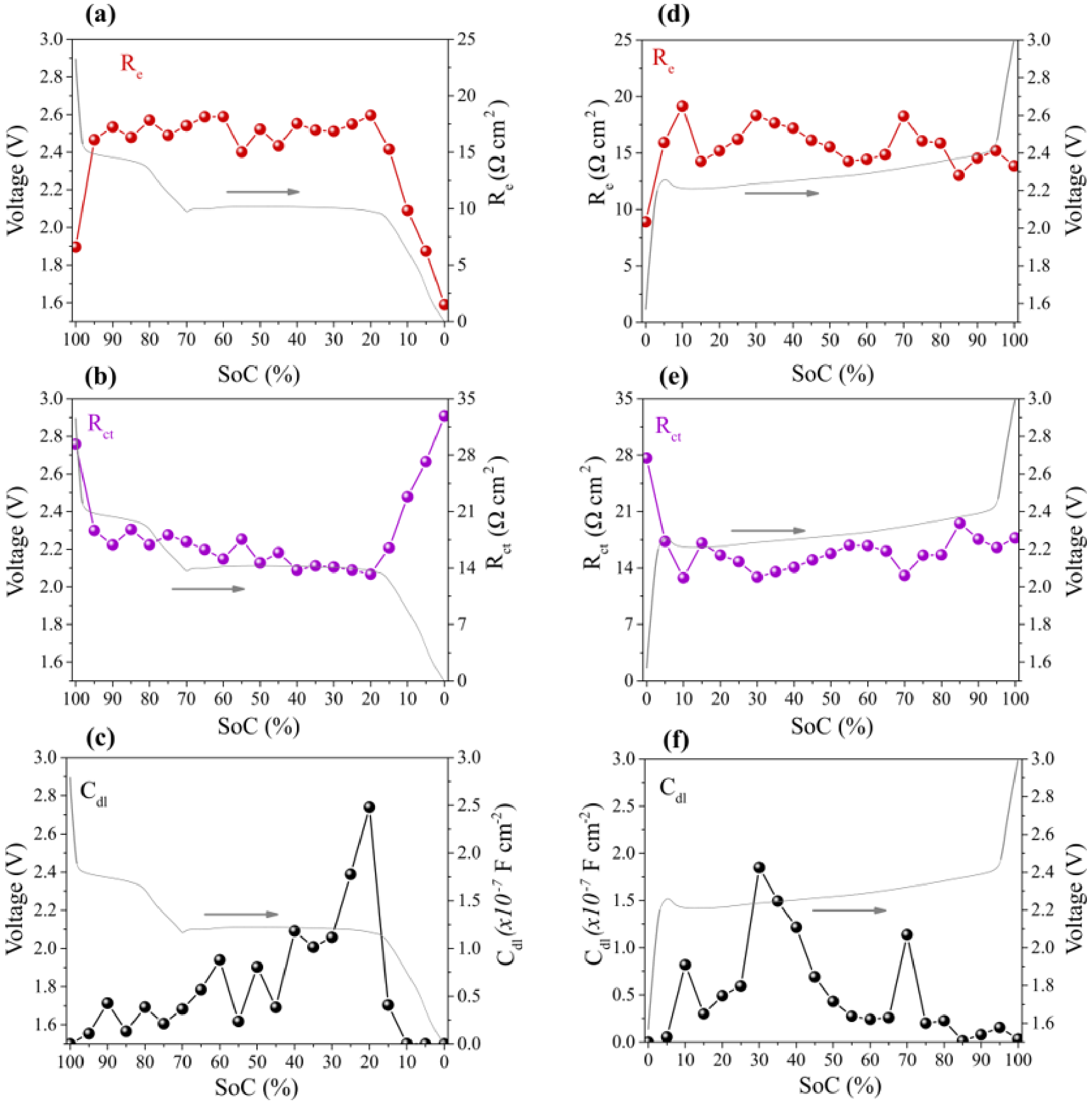

Figure 3.5 - Charge-discharge curves and the impedance parameters as a function of SoC.

3.3.4 Overall mass transport in the two-electrode cell at low frequencies

Special attention was paid to analyze the different parameters used to describe the nonideal diffusion in the finite diffusion barrier present in the two-electrode cell. In this sense, the GWE impedance used in this work is given as [200]:

$$Z_{\text{GWE}} = R_o \frac{coth[(jT\omega)^n}{(jT\omega)^n}, \tag{1}$$

where $R_o = \sigma l/\{D^{1/2}[(j\omega/D)^{1/2}l]^n\}$ and $T = l^2/D$.

The average diffusion coefficient (D) and/or the effective diffusion length (l) is commonly unknown for solid-state redox reactions. Therefore, the general diffusion characteristics are described by the simulation parameters R_o T, and n.

Figure 3.6 (a & d) shows the behavior of the T/s parameter representing the '*characteristic time constant*' for mass transport during the redox reaction. In this sense, T describes how fast the *active redox species* diffuse in a given length (l) [206]. As shown in **Figure 3.6 (c & f)**, the changes verified for T and R_o/Ω cm^2 as a function of SoC values are very similar. The latter parameter represents the '*mass-transfer resistance*' of the redox species in the tortuous paths present in porous electrode materials. In principle, the behavior verified for T and R_o can be associated with the formation of solid polysulfides. Generally, the behavior of R_o values can be associated with the blocking effect incurred by the formation of LPS precipitates (*e.g.*, Li_2S_2 and Li_2S) [154] in the electrolyte that are deposited on the porous electrode surface regions with the creation of an insulating layer that inhibits the ionic diffusion and electron transfer at the active surface sites. At ~0–10 SoC, the maximum values for T and R_o were observed. So, it is possible to interpret that the greater the number of solid sulfur species in the electrolyte, the greater its mass-transfer resistance and, consequently, the diffusion of the active redox species is retarded towards the electrode active surface regions where electron transfer occurs.

Knowing the basic electrochemical process of the Li-S batteries reported in the literature [207], it is possible to infer that the increase in R_o is associated with the migration of LPS which affects the diffusion resistance. These findings can be interpreted considering the formation of short-chain sulfur species. Analyzing the R_o variation with SoC, it is noticed that mass-transfer resistance strongly increases for SoC values lower than 20% (discharge-charge), indicating a poor electrochemical behavior for these conditions [207]. Generally, the changes in R_o can be ascribed to the formation of short-chain sulfur compounds and deposition of this species in the electrode considering the *shuttle* effect. As the discharge proceeds, it is verified that R_o increases. At the same time, for SoC values higher than 20%, soluble sulfur species are predominant (*e.g.*, Li_2S_4 and Li_2S_8), and the resistance values decreased during the charging process.

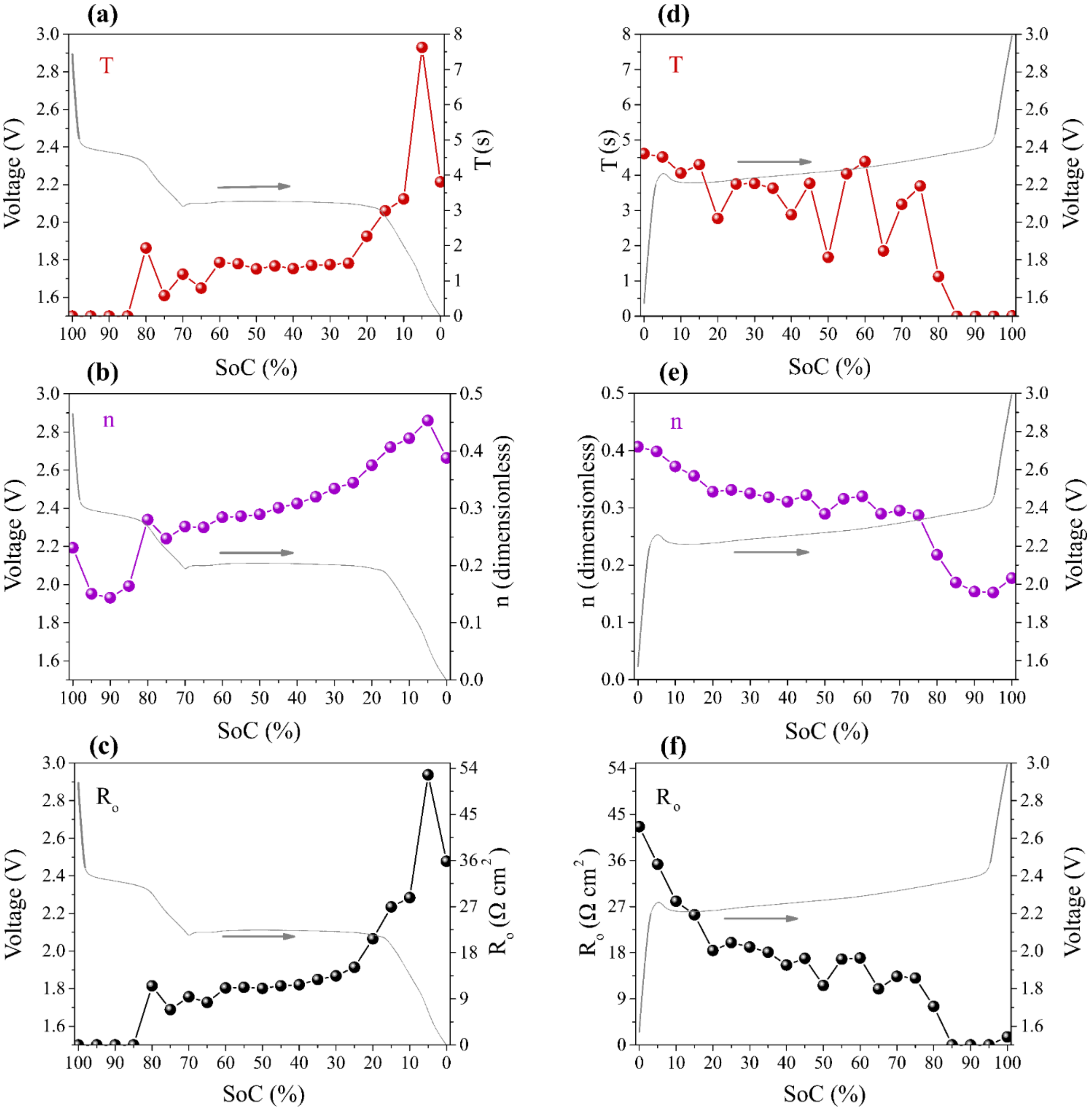

Figure 3.6 - Analysis of the finite diffusion process as a function of the cell voltage and SoC values.

Figure 3.6 (b & e) shows the behavior of the GWE exponent (n) representing the fractional (fractal) mass transport of the redox species in a disordered medium when $n \neq 0.5$. Generally, the formation of sulfur species with different relative sizes changes the transport characteristics in the narrow channels present in porous electrode materials. For both charge and discharge, the SoC values resulted in n values closer to 0.5 (normal conditions) in the presence of the Li_2S_2/Li_2S species (SoC < 20%) instead of S_8 (SoC > 75%). Therefore, the experimental findings show that more normal diffusion conditions are achieved when the device is practically fully discharged or charged, respectively. In addition, the *n vs. SoC* profiles verified for the discharge and charge are practically symmetric, indicating the mass-transport characteristics for the sulfur species are not altered as a function of the discharge-charge cycles.

3.3.5 Self-discharge evaluation

The self-discharge current (I_{sd}) was evaluated for the two-electrode battery cells. In this sense, the rate changes in open-circuit voltage (ΔOCV) were measured for the previously charged devices to evaluate I_{sd} at different voltages. It was assumed that all OCV variation is caused exclusively by the internal cell self-discharge. However, the OCV at a given SoC also changes according to the temperature and charge redistribution immediately after the charging or discharging steps. Since the temperature was kept constant at 24 ± 1°C, it is necessary to determine the relaxation time of the cell under test and disregard the data from this region for the correct evaluation of self-discharge current.

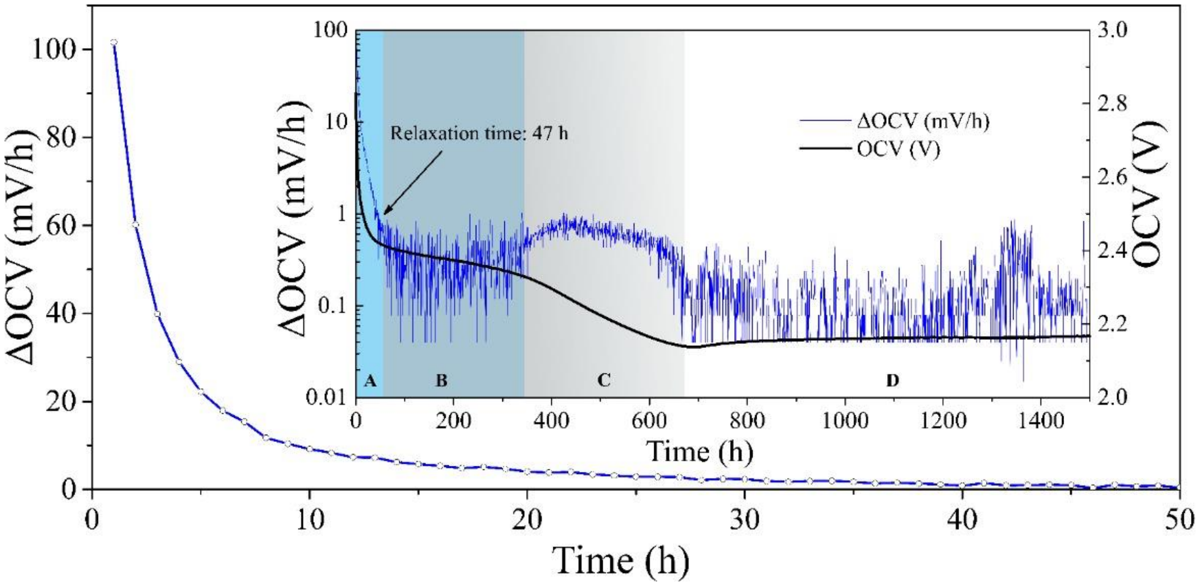

Figure 3.7 - Open circuit voltage changes during a 1500-h self-discharge test at 24 ± 1°C. Outer image (linear scale) depicts the behavior of the OCV in the region (**A**). Inner image (log scale for the *y*-axis) indicates the OCV profile and the ΔOCV values (mV h^{-1}) for the different regions of interest.

Figure 3.7 presents the results after a 1500-h self-discharge experiment where the OCV and the voltage rate change (ΔOCV/mV h^{-1}) are registered. Region (**A**) shows the ΔOCV values up to 100 mV h^{-1} due to the charge redistribution in the presence of a small contribution of the self-discharge current. The precise time when the charge redistribution effect over OCV becomes smaller than the self-discharge current effect cannot be readily determined. However, for practical purposes, it can be estimated as ≈ 47 h, corresponding to an ΔOCV lower than 1 mV h^{-1} for almost steady-state conditions. For region (**B**), it was detected an average ΔOCV value of 335 µV h^{-1} with maximum and minimum values of 1 mV h^{-1} and 39 µV h^{-1}, respectively. These results are relevant compared to the ΔOCV behavior found for the region (**C**) (*e.g.*, Li_2S_6 to Li_2S_4 decomposition), where ΔOCV assumes a much narrower and stable profile with an average value of ≈ 550 µV h^{-1}. Finally, region (**D**) presents a similar behavior to the region (**B**), but with a lower average ΔOCV value of 109 µV h^{-1}.

Considering the data from regions B, C and D and the voltage vs. SoC curve at C/40 previously obtained for the cell under test, **Table 2** presents five calculations obtained from 2.3 to 2.15 V in 100 mV and 50 mV step. Results indicate that I_{sd} is slightly above 600 nA and therefore means that the cell is under self-discharging at about 17% per month and will take approximately 42 h to discharge 1% of its capacity. This is significantly higher than usual self-discharge properties of commercial Li-ion cells, which usually discharge at <1% per month rate. However, these results were expected for Li-S cells [88].

Voltage interval	**Range (mV)**	**Time (h)**	**C/40 Test Capacity (µAh)**	**I_{sd} (nA)**	**Time to 1%-discharge (h)**	**Discharge % per month**
2.30 - 2.20 V	100	143	87	610	42	17
2.25 - 2.15 V	100	172	104	604	42	16
2.30 - 2.25 V	50	67	41	614	41	17
2.25 - 2.20 V	50	75	45	607	42	17
2.20 - 2.15 V	50	96	58	604	42	16

Table 1 – Results for a 1500-h self-discharge experiment at 24 ± 1°C.

When OCV drops below 2.15 V, the assessment of self-discharge capacity becomes very difficult because the cell exhibits the flat plateau already discussed in the previous sections. This makes the discrimination of OCV from the self-discharge experiment and SoC from the C/40 discharge test very dubious. The signal-to-noise ratio becomes small to the point where the variation of open-circuit voltage is no longer a reliable method to address the self-discharge current of the Li-S cell below 70% SoC. However, a residual (or remaining) capacity evaluation can be performed immediately after the 1500 h rest time experiment. It consists of discharging the cell to 1.5 V at a C/40 current and logging the extracted charge. The latter can be compared to the initially available charge at $t = 0$. This experiment revealed a residual stored charge in the cell of 1.32 mAh.

Table 3 presents the results at *t* = 0 and after 1500 h. Considering the 2.568 mAh initial charge (*t* = 0), the cell discharged 1.248 mAh during 1500 h, equivalent to an average self-discharge current of 832 nA. The results using this second method are somehow different from those shown in **Table 2**. However, they include the self-discharge occurring at 2.15 V (voltage plateau) that can not be determined with the other method. As seen, the findings for the different methods are in the hundreds of nA range and are sufficient for practical evaluation of the storage time. **Table 3** also shows that cell capacity was reduced by 11.4% while resting, indicating that the aging effects of electrolyte decomposition are significant. Coulombic efficiency also decreased immediately after the resting time.

Time (h)	**Charge Capacity (mAh)**	**Discharged Capacity (mAh)**	**Coulombic Efficiency (%)**
0	2.568	2.374	92
1500	2.276	2.070	90

Table 2 – Cell parameters at 0 h and after a 1500-h rest time.

3.4 Improvements, shuttle effect and state-of-art

3.4.1 Sulfur loading by area via thickness variation

Thinking about optimizing the electrode to obtain better results of loading of S_8 per area (g_{sulfur} cm^{-2}) and the state-of-art modifications for LSBs were carried out. **Chapter 3** describes an electrode with 60% of S_8 in its composition as charging about the mass of Activated Carbon (w/w) and a capacity of approximately 1050 mA.h g_{sulfur} cm^{-2}. New tests show that 90% loading is much more effective, thus offering an increase in capacity, starting at 1350 g_{sulfur} cm^{-2}. See more in **Figure 3.8.**

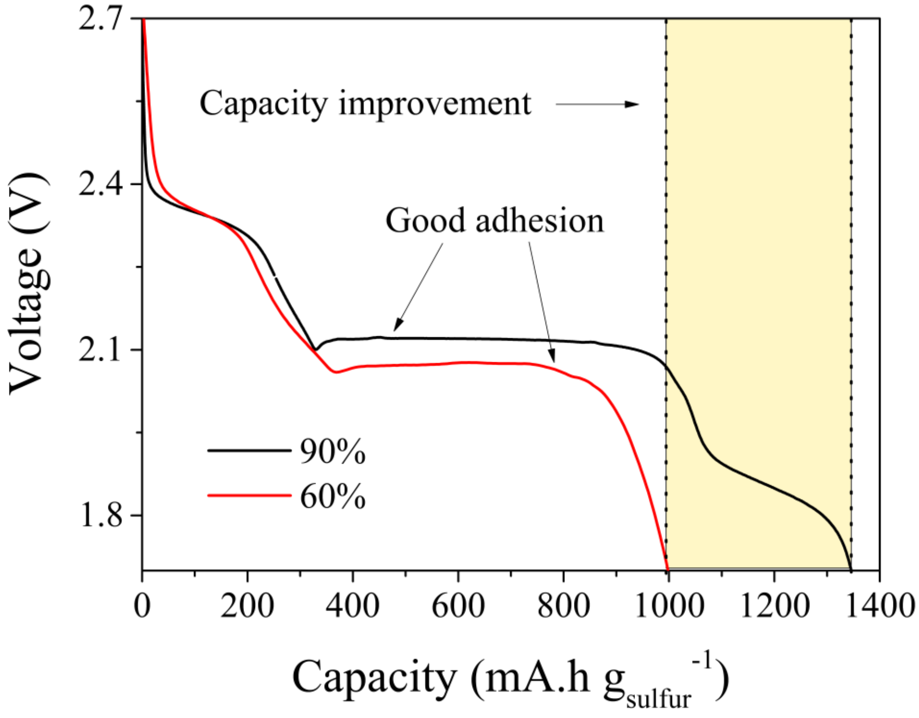

Figure 3.8 – Improvements in charging of sulfur mass in AC electrode.

Other sulfur ratios were also tested, such as 4.5 and 9.0 sulfur cm^{-2} but GCPL, CV and EIS tests showed that the long-term performance of these electrodes is inefficient. Here the electrode thicknesses were changed (55, 110 and 190 µm), focusing on finding the best proportion of active S_8 per area. It can conclude that the best parameters go to the data of 90% of S_8 *i.e.*, 2.1 sulfur cm^{-2}, maintaining the thickness of approximately 55 µm in Aluminum substrate (*TOB-Etched Aluminum foil* - 20 µm) as shown in **Figure 3.9 (a - c).** The cyclicability, cyclic voltammetry and impedance tests showed which electrode is more stable for our interests. Here, in sequence, this electrochemical behavior is presented, which in the future can be improved by optimizing the synthesis process, but which already shows us the best parameter tested here. **Figure 3.9** illustrates the performance of electrodes of different thicknesses, thus indicating the prototype that obtained the best electrochemical results.

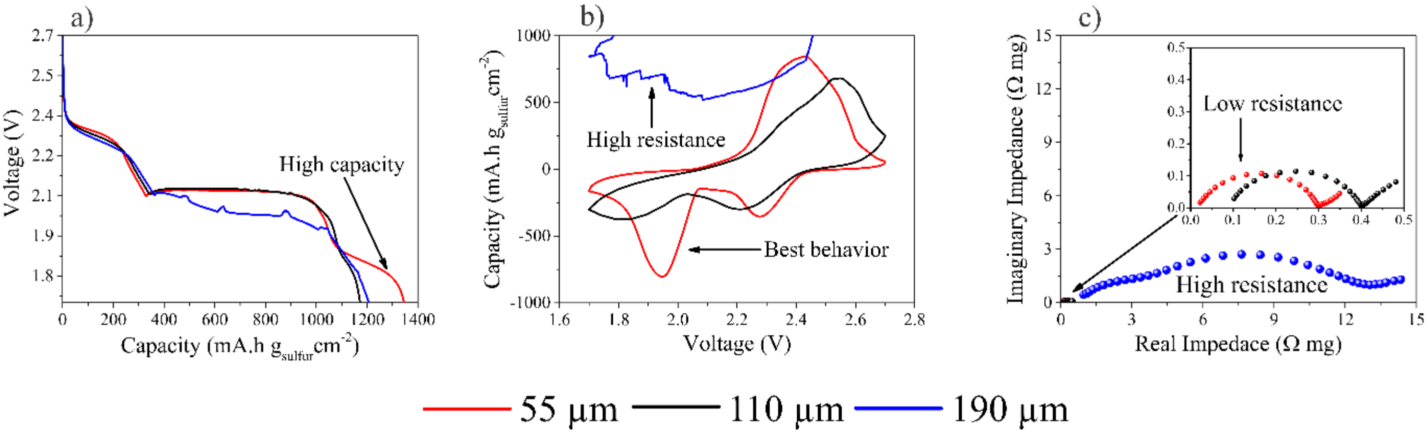

Figure 3.9 – First discharge using current of 50 μA (a), Cyclic voltammetry using 0.1 mV s^{-1}(b), EIS test (c). Author's preliminary results.

Based on the facts mentioned, the highlighted electrode is the one that has 2.1 g_{sulfur} cm^{-2} in its loading. Its first discharge presented the expected shape without noise for Li-S type systems and reached approximately 1350 mAh $g_{enxofre}$ cm^{-2} in **Figure a**, in addition to presenting a very well-behaved voltammogram with a larger area in **Figure b** with a lower impedance than the others. tested shown in **Figure c**. Based on this, this new sulfur loading was adopted for the other tests and is also subject to in-depth characterization. This material will serve as a template for possible future modifications.

3.5 Concluding Remarks

Here in this chapter, we present the production of porous electrodes for application in LSBs in their initial state and changes in their thickness, consequently in their sulfur per area ratio, *i.e.*, g_{sulfur} cm^{-2}. These modifications showed that the best ratio here should be approximately 2 g_{sulfur} cm^{-2}. Observing the results of thickness modification, it is possible to notice a higher initial capacity for the electrodes with less sulfur per area, being: 1170, 1200 and 1350 mA.h g_{sulfur} cm^{-2} for the electrodes of 9, 4.5 and 2 g_{sulfur} cm^{-2}. The state-of-art indicates that the correct ratio of sulfur per area is around 5 g_{sulfur} cm^{-2} but for our material, we observed that 2 g_{sulfur} cm^{-2} is the ideal amount. We can explore intermediate ratios in the future.

4 Discussion of results

4.1 The synthesis process

The process of synthesis of the electrodes is schematically shown in **Figure 3.0** of **chapter 3**. The synthesis is practical to produce ink with excellent particle dispersion, and excellent surface homogeneity is also observed after electrode drying. The homogeneity is confirmed because no clustering points are detected on the electrode surface. Cluster spots causes cracks and fissures in the coating and must be avoided. This process was beneficial for us to start production on a larger scale, *i.e.*, by applying the film with 10cm × 30cm area on an aluminum substrate with 20µm thickness, we can start to simulate a roll-to-roll process experimentally. The improvement of this process will be explored in the PhD and presented here briefly in the following sessions to understand our plans better. In this initial work, the substrate used was AISI316 stainless steel with a diameter of 16 mm.

4.2 Morphological characterization

Figure 3.1 (a-d) shows the surface image of the electrodes as prepared before being used in the electrochemical tests. The AC used has a high surface area ~2500 m^2 g^{-1} and the addition of BP 100 m^2 g^{-1}, binder and S_8, produce an electrode with ~300 m^2 g^{-1}. Such a high-surface area is essential in the cathode to facilitate reactions during charge and discharge potentials, as presented in **chapter 2**. The cathode composition of AC and S_8 is confirmed in **Figure 3.1 (e)**, evidencing the efficiency of the *melt-diffusion* process. Raman spectra confirm the presence of S_8 and AC. S_8 peaks are observed in regions below 600 cm^{-1} and AC above 1000 cm^{-1} in **Figure 3.1 (e)**. The Raman bands of the S_8 structure have active peaks at 153 cm^{-1}, 220 cm^{-1} and 473 cm^{-1}. The vibrational mode located at 150 cm^{-1} and 220 cm^{-1} refer to asymmetric S-S and symmetrical S-S bonds, respectively. The peak located at 473 cm^{-1} with a shoulder at approximately 467 cm^{-1} represents the elongation of the S-S bond to cyclic S_8 [183]. That confirms that the melting process keeps typical S_8 properties.

The D and G bands observed in the AC signature are well known for carbon-based materials. The D band is located at 1326 cm^{-1} for this laser line and is also related to ring breathing mode in the defective region; that is why it is assigned as a disorder in typical 180^o sigma bonds of sp^2 carbon materials. This mode is prohibited for infinite monocrystalline graphene [208]. The G band is assigned to the ring breathing mode of sp^2 carbon materials, *i.e.*, vibrational modes present in all C=C bonds [188]. The G band (*i.e.*, graphite) is observed at

1580 cm^{-1}. To better understand the interaction between the chemical species, present on the electrode surface from their binding energy, **Figure 3.1 (f)** presents the results of the XPS analysis. In **Figure 3.1 (f)** it is possible to observe bonds referring to the $1/2$ e $3/2$ sp^2 orbitals that come from the covalent bonds between sulfur and carbon. It is concluded that the presented methodology is efficient for composite production between S_8 and AC, *i.e.*, the electrode is an AC:S composite.

4.3 Electrochemical data and analysis

Figure 3.2 (a) presents the initial electrochemical results of our Li-S batteries, where it is possible to observe the Nernstian behavior of the active sulfur species within the used WVW (1.5 – 3.0V *i.e.*, Li_2S_8 – Li_2S). Here all oxidation and reduction processes of the used S_8 molecules are observed. For an analysis using a cell with two electrodes, the results are satisfactory so that the definition of the formation of the redox peaks was very effective, giving rise to the confirmation of the results obtained here and compared with works published in the literature[209]. In cathodic current, an increase in the width of peak number 5 (1.8 V) of **Figure 3.2 (a)** is observed when compared to the others (*i.e.*, 1, 2, 3 and 4). This fact occurs due to the generation of solid species corresponding to the shuttle effect (*i.e.*, Li_2S_2 and Li_2S). By increasing the electrolyte resistance in this region (please see more in **Figure 3.5 (a & d)**) caused by the precipitation of these species, there is an increase in polarization, and this phenomenon can be observed. The data are confirmed by observing the voltammogram and the EIS studies as a function of the SoC. The first discharge is shown in **Figure 3.2 (b)** also gives us an interesting parameter for comparison with the cathodic scan of the Li-S battery so that the curves formed in this graph are complementary to the peaks generated in the cyclic voltammetry during the discharge. This information can serve as a benchmark when observing unexpected Nernstian behaviors that generally manifest in the voltammogram related to contamination during the synthesis, coat application or assembly process.

The graphs in **Figure 3.2 (c – d)** correspond to the tests of capacity variation as a function of the applied current density **(c)**. Here it is possible to observe little electrode degradation when increasing the applied C-rate. A suitable electrode can resist this type of current variation when increased to higher densities and then return to a lower current state, following this order: 0.1C, 0.2C, 0.5C, 1C. 2C and go back to 1C. **Figure 3.2 (d)** of capacity as a function of the number of cycles presents this information. To understand how many cycles our prototype supports at a fixed current (1C), the cyclability test was performed to observe its variation at a fixed C-rate and the Coulombic efficiency transient. **Figure 3.2 (e)** shows a high degree of electrode degradation as a function of the number of cycles. From 100 cycles onwards, there is a decrease in capacity and an increase in efficiency. We believe that the reduction in capacity is linked to the formation of the LPS layer on the surface of the carbon electrode. The increase in efficiency can occur through the passivation of the lithium metal electrode, a typical process of oxidation of metals subjected to corrosive atmospheres, which in our case is induced by the charging and discharging cycles of the battery.

4.4 Electrochemical impedance data and analysis

In **Figure 3.3**, an analysis of the battery's SoC was performed as a function of the EIS behavior expressed in the complex plane impedance graph, also known as the Nyquist graph. Here the idea is to understand how the internal processes of the Li-S battery take place, but considering the impedance variation, *i.e.*, at low, medium and high frequencies at different points of the SoC. Between 20 – 70% of the SoC of the LSBs, the formation of plateaus is observed, making it very difficult to understand which SoC the battery is just looking at the Potential(V). Aiming at greater sensitivity, the EIS technique was chosen since it has great analytical potential among the others, does not provide degradation of the analyzed material, and can be performed quickly. Here we use the GEIS because it presents a lower variation of the battery's SoC in tests while collecting the EIS points. Initially, the potential is applied until the battery reaches 5% of its SoC, relaxation time is applied for 15 minutes and then the EIS points are collected. When the tests were carried out using PEIS, making the potentiostatic perturbation, a small variation of the battery's SoC was observed, and this would cause the points not to be acquired at the programmed locations *i.e.*, in intervals of 5 to 5% of the SoC until charging the Li-S battery (100% SoC) and after the finished test made the same for during the discharge.

For this, a GEIS point collection scan was performed every 5% of the SoC. As the variation of potential generates current and on the contrary is also valid. Analyzing the SoC to control the current perturbation proved more efficient when the battery SoC is more stable when the discharging or charging process has paused. To find the best data for the currents applied in the EIS test carried out in search of observing less scattering of points in the complex plane diagram. Initially, the alternating current (AC) was set to zero and the direct current (DC) 5 variations between 0, 50, 100 and 200 µA. Here distortion in results was observed. The opposite was performed, and the best parameters were also DC = 0 and AC = 100 µA. In the end, we had the **Figure 3.3 (c & d),** which appreciated the highlights of the important ones. For a deeper analysis, the electrochemical fitting to produce the equivalent circuit of our two-electrode cell was performed as shown in **Figure 3.4**, whose SoC point was chosen for the fitting at the point corresponding to 50%. At this point, we understand that the expressive behaviors are similar for charging and discharging since there are no species transformation curves in any of the charge and discharge processes. The simplest possible equivalent circuit must be applied. Looking at the data from our χ^2 data the *Randles* circuit showed the most efficient electrochemical system and represented suitable parameters. Other discussions were held below due to the electrochemical *fitting* of the equivalent circuit.

Figures 3.5 and **3.6** showed an analysis of all components of the equivalent circuit so that we can discuss each separately through the EIS points collected as 5 in 5% of the SoC. The R_e data presented in HF shown in **Figure 3.5 (a – d)** have a remarkable similarity to the chemical reduction processes and, shown in the literature for Li-S batteries, is observed[210–212]. When looking at 100% of the SoC it is possible to see that the impedance at this point is the lowest. Right after the transformation of solid phase sulfur to LPS, which in turn are soluble, we quickly observe a significant increase in electrolyte resistance. This behavior is maintained up to 20% of the SoC, which soon after is due to the formation of the *shuttle effect*.

For R_{ct} and C_{dl} data in *MF* the same behavior is observed within SoC observed in the electrolyte data, but now according to the phenomena that occur on the electrode/electrolyte surface. Initially, the highest resistance data of R_{CT} observed in **Figure 3.5 (b – e)** is precisely in 100% of the SoC, where there is a large amount of S_8, which in turn has insulating property. After solubilization of this reagent for LPS, there is a decrease in the internal resistance which then increases by 20% of the SoC due to the *shuttle effect*. This phenomenon happens in the same way as the charging process. The C_{dl} data follow this R_{CT} variation but now with the focus specifically on the evolution of capacitance. Basically, where there is a greater S_8 consumption process at the cathode, there is greater capacitance data. The behavior is highly coherent since when there is the consumption of this species present in the electrode, there is an increase in porosity and a decrease in the insulating element[154]. Therefore, the analysis proves to be highly efficient for obtaining these data, being much more sensitive than techniques focused only on observing the potential variation.

Figure 3.6 shows the fitting of the *Warburg* components observed at LF. This stage was used different parameters to describe the ideal finite barrier diffusion for a two-electrode cell. For the data in **Figure 3.6 (a & d)**, the behavior of T as a function of time(s) was observed to understand the characteristic time constant for mass transport during redox reactions. Here it is described how fast active redox species diffuse over a given length (l)—observing the charging and discharging behavior, the diffusion time of the species increases when they become soluble and interact with the electrolyte. This phenomenon causes the time to grow until the solid phase of the LPF appears. This phenomenon is observed for both the charge and the discharge. When the species are transformed into S_8, the diffusion reaction happens faster since there are not many long-chain species causing an increase in viscosity. **Figure 3.6 (c & f)** shows how variations in LF frequencies (T e R_o/Ω cm^2) as a function of SoC are very similar. The last parameter represents the mass transfer resistance of the redox species in the tortuous paths presented in porous electrode materials. Due to this fact, all the charging and discharging behavior that cause the increasing effect of the cell resistance are associated and duly described in the graphs. Generally, can associate the behavior of the R_o values with the blocking effect generated by forming LPS precipitates, which causes the shuttle effect.

As the Li-S battery forms some discharge levels, for example, at 70 to 20% of the SoC, when looking at the cathode scan, the use of EIS is essential to see the change of these internal transformations due to its high sensitivity. The *fitting* of these circuit parameters proved extremely coherent compared to the known redox processes for Li-S batteries. Future studies will be developed to combine this technique with spectroscopies that follow the morphological variation of the materials in question. Thus, the data can be related to the degree of degradation that the formation of these species causes in the electrode structure, which in the future is degraded in the charging and discharging processes. This study is being carried out in our laboratory.

4.5 Self-discharge observations

Here, the variation of Li-S battery self-discharge in open circuit potential (ΔOCV) was observed for 62 days, as shown in **Figure 3.7**. In conclusion, we can say that after 47 hours of cell relaxation, chemical equilibrium occurs, allowing us to assume a point to start the electrochemical tests. Creating electrochemical tests with potential variations in newly assembled batteries can generate dubious data, and that's why this study was carried out. In this way, it can be understood that the best time to start the analysis should be after the determined time of **A region** presented in that figure.

4.6 Understand the improvements. Shuttle effect and state-of-art

This change was essential to improve the performance of our LSB and not degrade both the electrodes and the DOD processes. When looking at the low area of the charge and discharge curve, there are not many points of decrease potential, so not much is lost in capacity when this change is made in the cut-off. Making this change in the *cut-off*, we have more use of our battery and gain in cycles and efficiency. When spoken about solving the *shuttle effect*, it is possible to attack by different ways, such as the addition of trapping structures or redox mediators in the electrode [213], aditives in electrolyte [214–216] and also exploring different carbon structures that act as a host focused on trapping the LPS. In addition to the changes presented in **Chapter 3** on varying sulfur ratios by area, it is noted that the surface of the aluminum substrate significantly influences coating. Initially, smoother surfaces were tested and presented inferior results to the substrate used with greater roughness in adhesion. The substrate used with the best result is *TOB – Etched Aluminum foil*, with width: 100 mm and thickness: 20 µm and has the following specifications:

Informations	
Areal density.	49g m^{-2}
Surface capacitance.	30~50 µf cm^{-2}
High-temperature oxidation resistance (200°C*30min).	No oxidation
Chemistry content (Al).	>99.45%
Tensile strength (N/CM).	>17
Ductility.	≥ 1.6%

Table 3 – Aluminum TOB substrate specifications.

In the initial results, the ink was deposited on AISI316 stainless steel substrate and then it was deposited on the Al substrate. We believe that the improvement in results is also due to this change. In addition, this modification allows testing in pouch cells, as they depend on electrodes of approximately 5 cm × 7 cm in area. Below is the ink applied on the Al current collector foil.

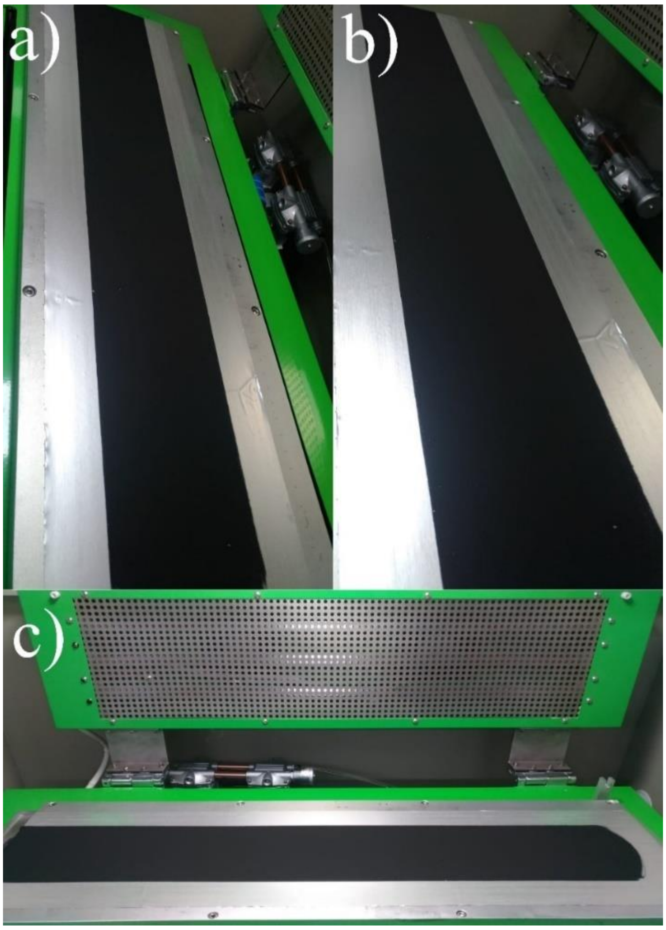

Figure 4.0 – Coating on Al foil by tape casting.

Relying on this improvement of the base electrode, ways to solve the shuttle effect were thought. As the electrode developed so far presented discharges with a capacity of up to 1350 g_{sulfur} cm^{-2}, is believed that the composite can be used as a template for more advanced tests. This way, we can take advantage of the best results of previous research and move towards an increasingly efficient battery.

5 Conclusion and Future Works

This dissertation has presented the main experimental results for an AC:S composite material used as the cathode in Li-S cells we have so far. The material was synthesized and characterized from carbon and sulfur materials. Activated carbon is a stable conductor with a high surface area that quickly extracts electrons from the thin sulfur layer. At the same time, sulfur species combined with Li forms LiS_x complexes that have quasi-reversible electrochemical behavior, storing large amounts of chemical energy to be converted into electrical energy. It was investigated the cell assembly and its respective electrochemical performance. The maximum cell capacity was 1044 g_{sulfur} cm^{-2}, which is 5 times higher than the typical values reported for modern Li-ion batteries. It was verified the quasi-reversible behavior of LiS_x complexes as a function of the state-of-charge (SoC). The cell response in the frequency domain was simulated to analyze the different impedance parameters as a function of SoC. The equivalent series resistance (R_e), charge-transfer resistance (R_{ct}), and double-layer capacitance (C_{dl}) showed stable behavior over 95% to 10% SoC during the discharge and charge. The capacity was reduced to 200 g_{sulfur} cm^{-2}, after 150 cycles, similar to modern LiBs. The cell self-discharge was ~17% a month, which is high compared to modern LIBs with values lower than 1%, and open circuit voltage hourly variation can be separated into regions coinciding with the presence of different polysulfides. The current study paves the way for future studies in Li-S batteries field. Generally, it was reported in this work as an exciting piece of science confirming and complementing several literature reports. Our research group will undertake a future study comparing novel classes of electrode materials and detailing the energy storage mechanisms at extreme SoC values (< 95% and > 20%) and novel SoC and SoH calculation methods. Some points can be highlighted:

- Synthesis and improvement of carbon-based electrodes with high surface area and mass production potential for application in Li-S batteries with 1350 mAh g_{sulfur}^{-1} of capacity.

- Optimization of parameters and electrochemical tests, avoiding excessive degradation of electrodes and cells in general.

- In-depth electrochemical characterization of cells and observation of the phenomena associated with the SoC as a function of electrochemical impedance spectroscopy (EIS) to understand the transformations of the main molecule and formation of the shuttle effect.

6 References

[1] Z.W. Lu, Y.H. Wang, Z. Dai, X.P. Li, C.Y. Zhang, G.Z. Sun, C.S. Gong, X.J. Pan, W. Lan, J.Y. Zhou, E.Q. Xie, One-pot sulfur-containing ion assisted microwave synthesis of reduced graphene oxide@nano-sulfur fibrous hybrids for high-performance lithium-sulfur batteries, Electrochimica Acta. 325 (2019) 134920. https://doi.org/10.1016/j.electacta.2019.134920.

[2] L. Mao, F. Wang, J. Mao, Polar mesoporous zinc sulfide nanosheets encapsulated in reduced graphene oxide three-dimensional foams for sulfur host, Scientific Reports. 10 (2020) 1–8. https://doi.org/10.1038/s41598-020-62037-4.

[3] A. Manthiram, Y. Fu, Y.S. Su, Challenges and prospects of lithium-sulfur batteries, Accounts of Chemical Research. 46 (2013) 1125–1134. https://doi.org/10.1021/ar300179v.

[4] C. Wang, W. Wan, J.T. Chen, H.H. Zhou, X.X. Zhang, L.X. Yuan, Y.H. Huang, Dual core-shell structured sulfur cathode composite synthesized by a one-pot route for lithium sulfur batteries, Journal of Materials Chemistry A. 1 (2013) 1716–1723. https://doi.org/10.1039/c2ta00915c.

[5] X. Ji, K.T. Lee, L.F. Nazar, A highly ordered nanostructured carbon-sulphur cathode for lithium-sulphur batteries, Nature Materials. 8 (2009) 500–506. https://doi.org/10.1038/nmat2460.

[6] Y. Fu, A. Manthiram, Core-shell structured sulfur-polypyrrole composite cathodes for lithium-sulfur batteries, RSC Advances. 2 (2012) 5927–5929. https://doi.org/10.1039/c2ra20393f.

[7] C. Fang, J. Li, M. Zhang, Y. Zhang, F. Yang, J.Z. Lee, M.H. Lee, J. Alvarado, M.A. Schroeder, Y. Yang, B. Lu, N. Williams, M. Ceja, L. Yang, M. Cai, J. Gu, K. Xu, X. Wang, Y.S. Meng, Quantifying inactive lithium in lithium metal batteries, Nature. 572 (2019) 511–515. https://doi.org/10.1038/s41586-019-1481-z.

[8] H. Yuan, T. Liu, Y. Liu, J. Nai, Y. Wang, W. Zhang, X. Tao, A review of biomass materials for advanced lithium-sulfur batteries, Chemical Science. 10 (2019) 7484–7495. https://doi.org/10.1039/c9sc02743b.

[9] S. Li, W. Zhang, J. Zheng, M. Lv, H. Song, L. Du, Inhibition of Polysulfide Shuttles in Li–S Batteries: Modified Separators and Solid-State Electrolytes, Advanced Energy Materials. 11 (2021) 1–24. https://doi.org/10.1002/aenm.202000779.

[10] Y. Lin, S. Huang, L. Zhong, S. Wang, D. Han, S. Ren, M. Xiao, Y. Meng, Organic liquid electrolytes in Li-S batteries: actualities and perspectives, Energy Storage Materials. 34 (2021) 128–147. https://doi.org/10.1016/j.ensm.2020.09.009.

[11] C. Yang, P. Li, J. Yu, L. Da Zhao, L. Kong, Approaching energy-dense and cost-effective lithium–sulfur batteries: From materials chemistry and price considerations, Energy. 201 (2020) 117718. https://doi.org/10.1016/j.energy.2020.117718.

[12] G.G.C. Peterson, J. Brgoch, Journal of Physics : Energy OPEN ACCESS, (2021) 0–13.

[13] Y. Bai, Y. Zhao, W. Li, L. Meng, Y. Bai, G. Chen, Organic-inorganic multi-scale enhanced interfacial engineering of sulfide solid electrolyte in Li-S battery, Chemical Engineering Journal. 396 (2020) 125334. https://doi.org/10.1016/j.cej.2020.125334.

[14] F. Zheng, M. Kotobuki, S. Song, M.O. Lai, L. Lu, Review on solid electrolytes for all-solid-state lithium-ion batteries, Journal of Power Sources. 389 (2018) 198–213. https://doi.org/10.1016/j.jpowsour.2018.04.022.

[15] Y. Kato, K. Kawamoto, R. Kanno, M. Hirayama, Discharge performance of all-solid-state battery using a lithium superionic conductor Li10GeP2S12, Electrochemistry. 80 (2012) 749–751. https://doi.org/10.5796/electrochemistry.80.749.

[16] X. Judez, M. Martinez-Ibañez, A. Santiago, M. Armand, H. Zhang, C. Li, Quasi-solid-state electrolytes for lithium sulfur batteries: Advances and perspectives, Journal of Power Sources. 438 (2019). https://doi.org/10.1016/j.jpowsour.2019.226985.

[17] R.D. Rauh, A Lithium/Dissolved Sulfur Battery with an Organic Electrolyte, Journal of The Electrochemical Society. 126 (1979) 523. https://doi.org/10.1149/1.2129079.

[18] G. Feng, J. Huang, B.G. Sumpter, V. Meunier, R. Qiao, Structure and dynamics of electrical double layers in organic electrolytes, Physical Chemistry Chemical Physics. 12 (2010) 5468–5479. https://doi.org/10.1039/c000451k.

[19] T. Zhou, W. Jin, W. Xue, B. Dai, C. Feng, X. Huang, P. Théato, Y. Li, Radical polymer-grafted carbon nanotubes as high-performance cathode materials for lithium

organic batteries with promoted n-/p-type redox reactions, Journal of Power Sources. 483 (2021). https://doi.org/10.1016/j.jpowsour.2020.229136.

[20] S. Meini, M. Piana, N. Tsiouvaras, A. Garsuch, H.A. Gasteiger, The effect of water on the discharge capacity of a non-catalyzed carbon cathode for Li-O2 batteries, Electrochemical and Solid-State Letters. 15 (2012). https://doi.org/10.1149/2.005204esl.

[21] M. Barghamadi, A.S. Best, A.I. Bhatt, A.F. Hollenkamp, M. Musameh, R.J. Rees, T. Rüther, Lithium-sulfur batteries - The solution is in the electrolyte, but is the electrolyte a solution?, Energy and Environmental Science. 7 (2014) 3902–3920. https://doi.org/10.1039/c4ee02192d.

[22] M. Barghamadi, A.S. Best, A.I. Bhatt, A.F. Hollenkamp, P.J. Mahon, M. Musameh, T. Rüther, Effect of Anion on Behaviour of Li-S Battery Electrolyte Solutions Based on N-Methyl-N-Butyl-Pyrrolidinium Ionic Liquids, Electrochimica Acta. 180 (2015) 636–644. https://doi.org/10.1016/j.electacta.2015.08.132.

[23] Y. Matsumae, K. Obata, A. Ando, M. Yanagi, Y. Kamei, K. Ueno, K. Dokko, M. Watanabe, Effects of Sulfur Loading, Cathode Porosity, and Electrolyte Amount on Li-S Battery Performance with Solvate Ionic Liquid Electrolyte, Electrochemistry. 87 (2019) 254–259.

[24] M. Wild, Lithium-Sulfur Batteries, 2019. https://doi.org/10.1002/9781119297895.

[25] H.S. Kim, C.S. Jeong, Electrochemical properties of binary electrolytes for lithium-sulfur batteries, Bulletin of the Korean Chemical Society. 32 (2011) 3682–3686. https://doi.org/10.5012/bkcs.2011.32.10.3682.

[26] N. Tachikawa, K. Yamauchi, E. Takashima, J.W. Park, K. Dokko, M. Watanabe, Reversibility of electrochemical reactions of sulfur supported on inverse opal carbon in glyme-Li salt molten complex electrolytes, Chemical Communications. 47 (2011) 8157–8159. https://doi.org/10.1039/c1cc12415c.

[27] R. Raccichini, J.W. Dibden, A. Brew, J.R. Owen, N. García-Aráez, Ion Speciation and Transport Properties of LiTFSI in 1,3-Dioxolane Solutions: A Case Study for Li-S Battery Applications, Journal of Physical Chemistry B. 122 (2018) 267–274. https://doi.org/10.1021/acs.jpcb.7b09614.

[28] J.H. Shin, E.J. Cairns, Characterization of N-Methyl-N-Butylpyrrolidinium Bis(trifluoromethanesulfonyl)imide-LiTFSI-Tetra(ethylene glycol) Dimethyl Ether Mixtures as a Li Metal Cell Electrolyte, Journal of The Electrochemical Society. 155 (2008) A368. https://doi.org/10.1149/1.2869876.

[29] D. Bresser, S. Passerini, B. Scrosati, Recent progress and remaining challenges in sulfur-based lithium secondary batteries - a review, Chemical Communications. 49 (2013) 10545–10562. https://doi.org/10.1039/c3cc46131a.

[30] Q. Liu, Q. Jiang, L. Jiang, J. Peng, Y. Gao, Z. Duan, X. Lu, Preparation of SnO 2 @rGO/CNTs/S composite and application for lithium-sulfur battery cathode material, Applied Surface Science. 462 (2018) 393–398. https://doi.org/10.1016/j.apsusc.2018.08.038.

[31] Q. Liu, Q. Jiang, L. Jiang, J. Peng, Y. Gao, Z. Duan, X. Lu, Preparation of SnO 2 @rGO/CNTs/S composite and application for lithium-sulfur battery cathode material, Applied Surface Science. 462 (2018) 393–398. https://doi.org/10.1016/j.apsusc.2018.08.038.

[32] Q. Zhao, K. Zhao, G. Ji, X. Guo, M. Han, J. Wen, Z. Ren, High sulfur loading , rGO-linked and polymer binder-free cathodes based on rGO wrapped N , P-codoped mesoporous carbon as sulfur host for Li-S batteries, Chemical Engineering Journal. 361 (2019) 1043–1052. https://doi.org/10.1016/j.cej.2018.12.153.

[33] Y. Mi, W. Liu, X. Li, J. Zhuang, H. Zhou, H. Wang, High-performance Li–S battery cathode with catalyst-like carbon nanotube-MoP promoting polysulfide redox, Nano Research. 10 (2017) 3698–3705. https://doi.org/10.1007/s12274-017-1581-8.

[34] Y. Tang, Y. Zhang, X. Rui, D. Qi, Y. Luo, W.R. Leow, S. Chen, J. Guo, J. Wei, W. Li, J. Deng, Y. Lai, B. Ma, X. Chen, Conductive Inks Based on a Lithium Titanate Nanotube Gel for High-Rate Lithium-Ion Batteries with Customized Configuration, Advanced Materials. 28 (2016) 1567–1576. https://doi.org/10.1002/adma.201505161.

[35] S.C. Rodrigues, M.C. Silva, J.A. Torres, M.L. Bianchi, Use of Magnetic Activated Carbon in a Solid Phase Extraction Procedure for Analysis of 2,4-dichlorophenol in Water Samples, Water, Air, and Soil Pollution. 231 (2020). https://doi.org/10.1007/s11270-020-04610-1.

[36] B.M. Pires, W.G. Nunes, B.G. Freitas, F.E.R. Oliveira, V. Katic, C.B. Rodella, L.M. Da Silva, H. Zanin, Characterization of porous cobalt hexacyanoferrate and activated carbon electrodes under dynamic polarization conditions in a sodium-ion pseudocapacitor, Journal of Energy Chemistry. 54 (2020) 53–62. https://doi.org/10.1016/j.jechem.2020.05.045.

[37] W. Gu, M. Sevilla, A. Magasinski, A.B. Fuertes, G. Yushin, Sulfur-containing activated carbons with greatly reduced content of bottle neck pores for double-layer capacitors: A case study for pseudocapacitance detection, Energy and Environmental Science. 6 (2013) 2465–2476. https://doi.org/10.1039/c3ee41182f.

[38] P. Han, S.H. Chung, A. Manthiram, Pyrrolic-Type Nitrogen-Doped Hierarchical Macro/Mesoporous Carbon as a Bifunctional Host for High-Performance Thick Cathodes for Lithium-Sulfur Batteries, Small. 15 (2019) 1–10. https://doi.org/10.1002/smll.201900690.

[39] S. Li, Z. Lin, G. He, J. Huang, Cellulose substance derived nanofibrous activated carbon as a sulfur host for lithium-sulfur batteries, Colloids and Surfaces A: Physicochemical and Engineering Aspects. 602 (2020) 125129. https://doi.org/10.1016/j.colsurfa.2020.125129.

[40] G.C. Li, J.J. Hu, G.R. Li, S.H. Ye, X.P. Gao, Sulfur/activated-conductive carbon black composites as cathode materials for lithium/sulfur battery, Journal of Power Sources. 240 (2013) 598–605. https://doi.org/10.1016/j.jpowsour.2013.02.095.

[41] W.S. Hummers, R.E. Offeman, Preparation of Graphitic Oxide, Journal of the American Chemical Society. 80 (1958) 1339. https://doi.org/10.1021/ja01539a017.

[42] H. Wu, J. Mou, L. Zhou, Q. Zheng, N. Jiang, D. Lin, Cloud cap-like, hierarchically porous carbon derived from mushroom as an excellent host cathode for high performance lithium-sulfur batteries, Electrochimica Acta. 212 (2016) 1021–1030. https://doi.org/10.1016/j.electacta.2016.07.153.

[43] D.M. Soares, R. Vicentini, A.C. Peterlevitz, C.B. Rodella, L.M. da Silva, H. Zanin, Tungsten oxide and carbide composite synthesized by hot filament chemical deposition as electrodes in aqueous-based electrochemical capacitors, Journal of Energy Storage. 26 (2019). https://doi.org/10.1016/j.est.2019.100905.

[44] R. Vicentini, D.M. Soares, W. Nunes, B. Freitas, L. Costa, L.M. Da Silva, H. Zanin, Core-niobium pentoxide carbon-shell nanoparticles decorating multiwalled carbon nanotubes as electrode for electrochemical capacitors, Journal of Power Sources. 434 (2019) 226737.

[45] V. BARANAUSKAS, A.C. PETERLEVITZ, H.G. ZANIN, R.F. TEÓFILO, H.J. CERAGIOLI, L.T. KUBOTA, others, CYLINDRICAL ELECTROCHEMICAL CELL WITH DOPED COAXIAL DIAMOND ANODE PRODUCED BY DEPOSITION OF DIAMOND-BEARING FILMS ON MECHANICALLY RESISTANT CYLINDRICAL SUBSTRATES, FOR USE IN AQUEOUS SOLUTION PURIFICATION PROCESSES, (2011).

[46] E.E. Fileti, A. Pascon, D. V Franco, L.M. Da Silva, H.G. Zanin, Effect of conductivity, viscosity, and density of water-in-salt electrolytes on the electrochemical behavior of supercapacitors: molecular dynamics simulations and in situ characterization studies1, (2022).

[47] C.G. Real, E.H.N.S. Thaines, L.A. Pocrifka, R.G. Freitas, G. Singh, H. Zanin, Freestanding niobium pentoxide-decorated multiwalled carbon nanotube electrode: Charge storage mechanism in sodium-ion pseudocapacitor and battery, Journal of Energy Storage. 52 (2022) 104793.

[48] D.K.M. Isidorio, E.A. Santos, R. Vicentini2--rafael, A.L.N. Filho, R.S. de Biasi, H. Zanin, APLICAÇÃO DE FERRITA DE COBALTO (CoFe2O4) E CARVÃO ATIVADO (CA) EM SUPERCAPACITORES, (n.d.).

[49] R. Vicentini, J.P. Aguiar, R. Beraldo, R. Venâncio, F. Rufino, L.M. Da Silva, H. Zanin, Cover Picture: Ragone Plots for Electrochemical Double-Layer Capacitors (8/2021), Batteries \& Supercaps. 4 (2021) 1197.

[50] B. Freitas, W. Nunes, C. Real, C. Rodella, G. Doubek, L.M. da Silva, E.H.N.S. Thaines, L. Pocrifka, R.G. Freitas, H. Zanin, Combining in Situ Electrochemistry, Operando Xrd \& Raman and Density Functional Theory to Investigate the Fundamentals of Li2co3 Formation in Supercapacitor, (n.d.).

[51] V. BARANAUSKAS, A.C. PETERLEVITZ, H.J. CERAGIOLI, F.T. DEGASPERI, P. RAGGIO, J. TSUKADA, H.G. ZANIN, others, SYSTEM FOR DEPOSITING

TUBULAR OR CONICAL DIAMANTIFEROUS FILMS, (2011).

[52] V. Baranauskas, A.C. Peterlevitz, H.G. Zanin, R.F. Teófilo, H.J. Ceragioli, L.T. Kubota, World Intellectual Property Organization PCT, BR. 385 (2010) 1.

[53] A.O. Lobo, H. Zanin, I.A.W.B. Siqueira, N.C.S. Leite, F.R. Marciano, E.J. Corat, Effect of ultrasound irradiation on the production of nHAp/MWCNT nanocomposites, Materials Science and Engineering: C. 33 (2013) 4305–4312.

[54] A.F.R.M. Marco A. V. M. Grinet Hudson Zanin, A. Oliveira, Fast preparation of free-standing nanohydroxyapatite--vertically aligned carbon nanotube scaffolds, Journal of Materials Chemistry B. 1 (2013) 194–203.

[55] L.R. de Andrade, A.S. Brito, A.M.G. de Souza Melero, H. Zanin, H.J. Ceragioli, V. Baranauskas, K.S. Cunha, S.P. Irazusta, Absence of mutagenic and recombinagenic activity of multi-walled carbon nanotubes in the Drosophila wing-spot test and Allium cepa test, Ecotoxicology and Environmental Safety. 99 (2014) 92–97.

[56] H. Zanin, P.W. l May, M. Hamanaka, E.J. Corat, Field emission from hybrid diamond-like carbon and carbon nanotube composite structures, ACS Applied Materials \& Interfaces. 5 (2013) 12238–12243.

[57] H. Zanin, P.W. May, D.J. Fermin, D. Plana, S.M.C. Vieira, W.I. Milne, E.J. Corat, Porous boron-doped diamond/carbon nanotube electrodes, ACS Applied Materials \& Interfaces. 6 (2014) 990–995.

[58] T.A. Silva, H. Zanin, E. Saito, R.A. Medeiros, F.C. Vicentini, E.J. Corat, O. Fatibello-Filho, Electrochemical behaviour of vertically aligned carbon nanotubes and graphene oxide nanocomposite as electrode material, Electrochimica Acta. 119 (2014) 114–119.

[59] H. Zanin, E. Saito, F.R. Marciano, H.J. Ceragioli, A.E.C. Granato, M. Porcionatto, A.O. Lobo, Fast preparation of nano-hydroxyapatite/superhydrophilic reduced graphene oxide composites for bioactive applications, Journal of Materials Chemistry B. 1 (2013) 4947–4955.

[60] R. Vicentini, W. Nunes, L.H. Costa, A. Pascon, L. da Silva, M. Baldan, H.G. Zanin, Environmentally friendly functionalization of porous carbon electrodes for aqueous based electrochemical capacitors, IEEE Transactions on Nanotechnology. (2018).

[61] M.A.V.M. Grinet, H. Zanin, A.E.C. Granato, M. Porcionatto, F.R. Marciano, A.O. Lobo, Fast preparation of free-standing nanohydroxyapatite--vertically aligned carbon nanotube scaffolds, Journal of Materials Chemistry B. 2 (2014) 1196–1204.

[62] T.A. Silva, H. Zanin, F.C. Vicentini, E.J. Corat, O. Fatibello-Filho, Differential pulse adsorptive stripping voltammetric determination of nanomolar levels of atorvastatin calcium in pharmaceutical and biological samples using a vertically aligned carbon nanotube/graphene oxide electrode, Analyst. 139 (2014) 2832–2841.

[63] H. Zanin, P.W. May, A.O. Lobo, E. Saito, J.P.B. Machado, G. Martins, V.J. Trava-Airoldi, E.J. Corat, Effect of multi-walled carbon nanotubes incorporation on the structure, optical and electrochemical properties of diamond-like carbon thin films, Journal of The Electrochemical Society. 161 (2014) H290.

[64] H. Zanin, L.M. Hollanda, H.J. Ceragioli, M.S. Ferreira, D. Machado, M. Lancellotti, R.R. Catharino, V. Baranauskas, A.O. Lobo, Carbon nanoparticles for gene transfection in eukaryotic cell lines, Materials Science and Engineering: C. 39 (2014) 359–370.

[65] L.M. Hollanda, A.O. Lobo, M. Lancellotti, E. Berni, E.J. Corat, H. Zanin, Graphene and carbon nanotube nanocomposite for gene transfection, Materials Science and Engineering: C. 39 (2014) 288–298.

[66] E. Saito, E.F. Antunes, H. Zanin, F.R. Marciano, A.O. Lobo, V.J. Trava-Airoldi, E.J. Corat, Oxygen plasma exfoliated vertically-aligned carbon nanotubes as electrodes for ultrasensitive stripping detection of Pb2+, Journal of The Electrochemical Society. 161 (2014) H321.

[67] H. Zanin, A. Margraf-Ferreira, N.S. Da Silva, F.R. Marciano, E.J. Corat, A.O. Lobo, Graphene and carbon nanotube composite enabling a new prospective treatment for trichomoniasis disease, Materials Science and Engineering: C. 41 (2014) 65–69.

[68] M.M. Zogbi Jr, E. Saito, H. Zanin, F.R. Marciano, A.O. Lobo, Hydrothermal--electrochemical synthesis of nano-hydroxyapatite crystals on superhydrophilic vertically aligned carbon nanotubes, Materials Letters. 132 (2014) 70–74.

[69] H. Zanin, H.J. Ceragioli, A.C. Peterlevitz, V. Baranauskas, F.R. Marciano, A.O. Lobo, Field emission properties of the graphenated carbon nanotube electrode, Applied

Surface Science. 324 (2015) 174–178.

[70] H. Zanin, P.W. May, R.L. Harniman, T. Risbridger, E.J. Corat, D.J. Fermin, High surface area diamond-like carbon electrodes grown on vertically aligned carbon nanotubes, Carbon. 82 (2015) 288–296.

[71] W.G. Nunes, R. Vicentini, L.M. Da Silva, L.H. Costa, T. Tadeu, H. Zanin, Surface and Electrochemical Properties of Radially Oriented Multiwalled Carbon Nanotubes Grown on Stainless Steel Mesh, Journal of The Electrochemical Society. 165 (2018) A3684--A3696. https://doi.org/10.1149/2.022816jes.

[72] T.A. Silva, H. Zanin, P.W. May, E.J. Corat, O. Fatibello-Filho, Electrochemical performance of porous diamond-like carbon electrodes for sensing hormones, neurotransmitters, and endocrine disruptors, ACS Applied Materials \& Interfaces. 6 (2014) 21086–21092.

[73] C. Oliveira, M.F. Stein, E. Saito, H. Zanin, L.S. Vieira, L. Raniero, V.J. Trava-Airoldi, A.O. Lobo, F.R. Marciano, Effect of gold oxide incorporation on electrochemical corrosion resistance of diamond-like carbon, Diamond and Related Materials. 53 (2015) 40–44.

[74] I.A.W.B. Siqueira, C.A.G.S. Oliveira, H. Zanin, M.A.V.M. Grinet, A.E.C. Granato, M.A. Porcionatto, F.R. Marciano, A.O. Lobo, Bioactivity behaviour of nano-hydroxyapatite/freestanding aligned carbon nanotube oxide composite, Journal of Materials Science: Materials in Medicine. 26 (2015) 1–10.

[75] L.D.R. Cardoso, V.J. Trava-Airoldi, F.S. Silva, H.G. Zanin, E.F. Antunes, E.J. Corat, Control of the length and density of carbon nanotubes grown on carbon fiber for composites reinforcement, MRS Online Proceedings Library (OPL). 1752 (2015) 77–82.

[76] H. Zanin, C.M.R. Rosa, N. Eliaz, P.W. May, F.R. Marciano, A.O. Lobo, Assisted deposition of nano-hydroxyapatite onto exfoliated carbon nanotube oxide scaffolds, Nanoscale. 7 (2015) 10218–10232.

[77] T.A. Silva, H. Zanin, F.C. Vicentini, E.J. Corat, O. Fatibello-Filho, Electrochemical determination of rosuvastatin calcium in pharmaceutical and human body fluid samples using a composite of vertically aligned carbon nanotubes and graphene oxide as the

electrode material, Sensors and Actuators B: Chemical. 218 (2015) 51–59.

[78] L.E.S. Soares, S. Nahorny, F.R. Marciano, H. Zanin, A. de Oliveira Lobo, Micro energy-dispersive x-ray fluorescence spectrometry study of dentin coating with nanobiomaterials, in: Biophotonics South America, 2015: pp. 389–400.

[79] T. Silva, H. Zanin, E. Corat, P. May, O. Fatibello-Filho, Preparation and electroanalytical applications of vertically aligned carbon nanotubes, in: Electrochemistry: Volume 13, Royal Society of Chemistry, 2015: p. 50.

[80] H. ZANIN, G. Desenvolvimento de eletrodos cil{\'\i}ndricos de diamante para tratamento de águas, Tese (Doutorado em Engenharia Elétrica)-UNICAMP, Campinas, 2012.

[81] B.C. Lourencao, T.A. Silva, H. Zanin, P.W. May, E.J. Corat, O. Fatibello-Filho, Promising electrochemical performance of high-surface-area boron-doped diamond/carbon nanotube electroanalytical sensors, Journal of Solid State Electrochemistry. 20 (2016) 2403–2409.

[82] R. Vicentini, J. Pedro Aguiar, R. Beraldo, R. Venâncio, F. Rufino, L. M. Da Silva, H. ZANIN, Ragone plots for electrochemical double-layer capacitors, Batteries & Supercaps. (2021). https://doi.org/10.1002/batt.202100093.

[83] T.S. Souza, H.G. Zanin, A. Peterlevitz, V. Baranauskas, G.A. da Silva, C. Reis, E.L. Reis, R.F. Teófilo, MCR-ALS applied to the quantitative monitoring of the electrodegradation process of atrazine using UV spectra: comparative results with HPLC-DAD as a reference method, Qu{\'\i}mica Nova. 39 (2016) 137–145.

[84] N. Metoki, C.M.R. Rosa, H. Zanin, F.R. Marciano, N. Eliaz, A.O. Lobo, Electrodeposition and biomineralization of nano-\$β\$-tricalcium phosphate on graphenated carbon nanotubes, Surface and Coatings Technology. 297 (2016) 51–57.

[85] H. Zanin, B.V.M. Rodrigues, W.A.R. Neto, R.E.S. Bretas, N.S. Da-Silva, F.R. Marciano, A.O. Lobo, High loading of graphene oxide/multi-walled carbon nanotubes into PDLLA: A route towards the design of osteoconductive, bactericidal and non-immunogenic 3D porous scaffolds, Materials Chemistry and Physics. 177 (2016) 56–66.

[86] H. Zanin, Desenvolvimento de um reator para o crescimento de filmes diamant{\'\i}feros tubulares., Universidade Estadual de Campinas, 2008.

[87] J.V.S. Moreira, E.J. Corat, P.W. May, L.D.R. Cardoso, P.A. Lelis, H. Zanin, Freestanding aligned multi-walled carbon nanotubes for supercapacitor devices, Journal of Electronic Materials. 45 (2016) 5781–5788.

[88] P.W. May, M. Clegg, T.A. Silva, H. Zanin, O. Fatibello-Filho, V. Celorrio, D.J. Fermin, C.C. Welch, G. Hazell, L. Fisher, others, Diamond-coated ‘black silicon’as a promising material for high-surface-area electrochemical electrodes and antibacterial surfaces, Journal of Materials Chemistry B. 4 (2016) 5737–5746.

[89] T.S. Souza, H.G. Zanin, A. Peterlevitz, V. Baranauskas, G.A. da Silva, C. Reis, E.L. Reis, R.F. Teófilo, MCR-ALS Aplicado no monitoramento quantitativo do processo de eletrodegradação da atrazina usando espectros UV: Resultados comparativos com HPLC-DAD como um método de referência, Qu{\'\i}mica Nova. 39 (2016) 137–145.

[90] H. Zanin, J.C.M. de Almeida, EE641 (Laboratório de Eletrônica II), (n.d.).

[91] A.C. Peterlevitz, P.W. May, R.L. Harniman, J.A. Jones, H.J. Ceragioli, H. Zanin, Fast electron transfer kinetics on novel interconnected nanospheres of graphene layers electrodes, Thin Solid Films. 616 (2016) 698–702.

[92] R. Iannini, F.T. Degasperi, H. Ceragioli, M.V. Amorim, A. Peterlevitz, V. Baranauskas, H. Zanin, Desenvolvimento de um sistema de aquisição de dados e de controle para a realização de ensaios de emissão de elétrons, (2016).

[93] H. Zanin, A.C. Peterlevitz, H.J. Ceragioli, R.F. Teofilo, F.T. Degasperi, V. Baranauskas, Large-area cylindrical diamond electrodes, ECS Journal of Solid State Science and Technology. 1 (2012) N67.

[94] J.V.S. Moreira, P.W. May, E.J. Corat, A.C. Peterlevitz, R.A. Pinheiro, H. Zanin, Diamond and carbon nanotube composites for supercapacitor devices, Journal of Electronic Materials. 46 (2017) 929–935.

[95] R.F. Spindola, H. Zanin, C.S. Macena, A. Contin, R. de Cássia Silva Luz, F.S. Damos, Evaluation of a novel composite based on functionalized multi-walled carbon nanotube and iron phthalocyanine for electroanalytical determination of isoniazid, Journal of

Solid State Electrochemistry. 21 (2017) 1089–1099.

[96] T.A. Silva, H. Zanin, E.J. Corat, O. Fatibello-Filho, Simultaneous voltammetric determination of paracetamol, codeine and caffeine on diamond-like carbon porous electrodes, Electroanalysis. 29 (2017) 907–916.

[97] S. Nahorny, H. Zanin, V.A. Christino, F.R. Marciano, A.O. Lobo, L.E.S. Soares, Multi-walled carbon nanotubes/graphene oxide hybrid and nanohydroxyapatite composite: A novel coating to prevent dentin erosion, Materials Science and Engineering: C. 79 (2017) 199–208.

[98] J.V. da Silva Moreira, P.L. da R. Almeida, H.G. Zanin, CARACTERIZAÇÃO DE NANOTUBOS DE CARBONO DE PAREDES MÚLTIPLAS AUTOSSUSTENTÁVEIS COMO DISPOSITIVOS SUPERCAPACITORES, Revista Univap. 22 (2016) 910.

[99] J.S. Farias, H. Zanin, A.S. Caldas, C.C. Dos Santos, F.S. Damos, R. de Cássia Silva Luz, Functionalized multiwalled carbon nanotube electrochemical sensor for determination of anticancer drug flutamide, Journal of Electronic Materials. 46 (2017) 5619–5628.

[100] A.G. dos Santos Neto, C.S. de Sousa, A. da Silva Freires, S.M. Silva, H. Zanin, F.S. Damos, R. de Cássia Silva Luz, Electrochemical sensor for detection of imipramine antidepressant at low potential based on oxidized carbon nanotubes, ferrocenecarboxylic acid, and cyclodextrin: application in psychotropic drugs and urine samples, Journal of Solid State Electrochemistry. 22 (2018) 1385–1394.

[101] R. Vicentini, L.H. Costa, W. Nunes, O. Vilas Boas, D.M. Soares, T.A. Alves, C. Real, C. Bueno, A.C. Peterlevitz, H. Zanin, Direct growth of mesoporous Carbon on aluminum foil for supercapacitors devices, Journal of Materials Science: Materials in Electronics. 29 (2018) 10573–10582.

[102] J.J.S. Teles, E.R. Faria, J.H.M. Santos, L.G. De Sousa, D. V Franco, W.G. Nunes, H. Zanin, L.M. Da Silva, Supercapacitive properties, anomalous diffusion, and porous behavior of nanostructured mixed metal oxides containing Sn, Ru, and Ir, Electrochimica Acta. 295 (2019) 302–315.

[103] W.G. Nunes, L.M. Da Silva, R. Vicentini, B.G.A. Freitas, L.H. Costa, A.M. Pascon, H.

Zanin, Nickel oxide nanoparticles supported onto oriented multi-walled carbon nanotube as electrodes for electrochemical capacitors, Electrochimica Acta. 298 (2019) 468–483.

[104] J. Tsukada, H. Zanin, L.C.A. Barbosa, G.A. da Silva, H.J. Ceragioli, A.C. Peterlevitz, R.F. Teofilo, V. Baranauskas, Electro-deposition of carbon structures at mid voltage and room temperature using ethanol/aqueous solutions, Journal of the Electrochemical Society. 159 (2012) D159.

[105] C.G.M. Real, R. Vicentini, W.G. Nunes, O.V. Boas, L.H. Costa, D.M. Soares, H. Zanin, Electric double layer capacitors prepared with polyvinyl alcohol and multi-walled carbon nanotubes, 2018.

[106] C.G.M. Real, R. Vicentini, W.G. Nunes, O.V. Boas, T.A. Alves, D.M. Soares, H. Zanin, Polyacrylonitrile and activated carbon composite for electric double layer capacitors, 2018.

[107] R. Vicentini, W.G. Nunes, L.H. Costa, L.M. Da Silva, A. Pascon, P. Jackson, G. Doubek, H. Zanin, Highly stable nickel-aluminum alloy current collectors and highly defective multi-walled carbon nanotubes active material for neutral aqueous-based electrochemical capacitors, Journal of Energy Storage. 23 (2019) 116–127.

[108] R. Vicentini, L.M. Da Silva, E.P. Cecilio Junior, T.A. Alves, W.G. Nunes, H. Zanin, How to measure and calculate equivalent series resistance of electric double-layer capacitors, Molecules. 24 (2019) 1452.

[109] H. Zanin, E. Saito, H.J. Ceragioli, V. Baranauskas, E.J. Corat, Reduced graphene oxide and vertically aligned carbon nanotubes superhydrophilic films for supercapacitors devices, Materials Research Bulletin. 49 (2014) 487–493.

[110] R. Vicentini, W.G. Nunes, L.H. da Costa, L.M. Da Silva, B. Freitas, A.M. Pascon, O. Vilas-Boas, H. Zanin, Multi-walled carbon nanotubes and activated carbon composite material as electrodes for electrochemical capacitors, Journal of Energy Storage. 33 (2021) 100738.

[111] B. Vitor, P.A. Carlos, Z.H. Giovani, C.H. Jose, others, Filmes DiamantÍferos MagnÉticos E Processo De Crescimento Dos Mesmos Por DeposiÇço QuÍmica De Vapores, (2013).

[112] P.A. Carlos, C.H. Jose, Z.H. Giovani, B. Vitor, others, Nanotubos E Nanofibras De Carbono, Processo De FabricaÇço E Uso Dos Mesmos, (2013).

[113] B. Vitor, P.A. Carlos, Z.H. Giovani, T.R. Francisco, C.H. Jose, K.L. Tatsuo, others, Cylindrical Electrochemical Cell With Doped Coaxial Diamond Anode Produced By Deposition Of Diamond-bearing Films On Mechanically Resistant Cylindrical Substrates, For Use In Aqueous Solution Purification Processes, (2011).

[114] B. Vitor, P.A. Carlos, C.H. Jose, D.F. Tadeu, R. Pedro, T. Jsckson, Z.H. Giovani, System For Depositing Tubular Or Conical Diamantiferous Films, (n.d.).

[115] H.G. Zanin, A.C. Peterlevitz, R.F. Teófilo, H.J. Ceragioli, V. Baranauskas, Synthesis and characterization of magnetic nanocrystalline diamond films, Ferroelectrics. 436 (2012) 96–100.

[116] P.A. Carlos, C.H. Jose, D.F. Tadeu, R. Pedro, T. Jackson, Z.H. Giovani, B. Vitor, others, System For Depositing Tubular Or Conical Diamantiferous Films, (2012).

[117] N.A. Zambianco, T.A. Silva, H. Zanin, O. Fatibello-Filho, B.C. Janegitz, Novel electrochemical sensor based on nanodiamonds and manioc starch for detection of diquat in environmental samples, Diamond and Related Materials. 98 (2019) 107512.

[118] R. Vicentini, W. Nunes, B.G.A. Freitas, L.M. Da Silva, D.M. Soares, R. Cesar, C.B. Rodella, H. Zanin, Niobium pentoxide nanoparticles@ multi-walled carbon nanotubes and activated carbon composite material as electrodes for electrochemical capacitors, Energy Storage Materials. 22 (2019) 311–322.

[119] V.S. Carvalho, A.N. Miranda, W.G. Nunes, L.H. Costa, A.M. Pascon, C.B. Rodella, H. Zanin, G. Doubek, Radially ordered carbon nanotubes performance for Li-O2 batteries: Pre-treatment influence on capacity and discharge products, Catalysis Today. 348 (2020) 299–306.

[120] L.M. Da Silva, R. Cesar, C.M.R. Moreira, J.H.M. Santos, L.G. De Souza, B.M. Pires, R. Vicentini, W. Nunes, H. Zanin, Reviewing the fundamentals of supercapacitors and the difficulties involving the analysis of the electrochemical findings obtained for porous electrode materials, Energy Storage Materials. 27 (2020) 555–590.

[121] D.A.C. da Silva, A.J.P. Neto, A.M. Pascon, E.E. Fileti, L.R.C. Fonseca, H.G. Zanin,

Exploring doped or vacancy-modified graphene-based electrodes for applications in asymmetric supercapacitors, Physical Chemistry Chemical Physics. 22 (2020) 3906–3913.

[122] W.G. Nunes, B.M. Pires, F.E.R. De Oliveira, A.M.P. de Marque, L.F. Cremasco, R. Vicentini, G. Doubek, L.M. Da Silva, H. Zanin, Study of the aging process of nanostructured porous carbon-based electrodes in electrochemical capacitors filled with aqueous or organic electrolytes, Journal of Energy Storage. 28 (2020) 101249.

[123] R.F. Teófilo, H. Zanin, A.C. Peterlevitz, U. Oliveira, J.C. de Paiva, H.J. Ceragioli, E.L. Reis, V. Baranauskas, Diamond cylindrical anodes for electrochemical treatment of persistent compounds in aqueous solution, (2012).

[124] B.M. Pires, W.G. Nunes, B.G. Freitas, F.E.R. Oliveira, V. Katic, C.B. Rodella, L.M. Da Silva, H. Zanin, Characterization of porous cobalt hexacyanoferrate and activated carbon electrodes under dynamic polarization conditions in a sodium-ion pseudocapacitor, Journal of Energy Chemistry. 54 (2021) 53–62.

[125] W.G. Nunes, R. Vicentini, B.G.A. Freitas, F.E.R. Oliveira, A.M.P. Marque, R. Maciel Filho, G. Doubek, L.M. Da Silva, H. Zanin, Pseudo-capacitive behavior of multi-walled carbon nanotubes decorated with nickel and manganese (hydr) oxides nanoparticles, Journal of Energy Storage. 31 (2020) 101583.

[126] H. Zanin, R.F. Teófilo, A.C. Peterlevitz, U. Oliveira, J.C. de Paiva, H.J. Ceragioli, E.L. Reis, V. Baranauskas, Diamond cylindrical anodes for electrochemical treatment of persistent compounds in aqueous solution, Journal of Applied Electrochemistry. 43 (2013) 323–330.

[127] W.G. Nunes, B.G.A. Freitas, R.M. Beraldo, L.M. Da Silva, H. Zanin, others, A rational experimental approach to identify correctly the working voltage window of aqueous-based supercapacitors, Scientific Reports. 10 (2020) 1–9.

[128] R. Vicentini, L.M. Da Silva, D. V Franco, W.G. Nunes, J. Fiates, G. Doubek, L.F.M. Franco, R.G. Freitas, C. Fantini, H. Zanin, Raman probing carbon \& aqueous electrolytes interfaces and molecular dynamics simulations towards understanding electrochemical properties under polarization conditions in supercapacitors, Journal of Energy Chemistry. 60 (2021) 279–292.

[129] D.M. Soares, Z. Ren, S. Bin Mujib, S. Mukherjee, C.G. Martins Real, M. Anstine, H. Zanin, G. Singh, Additive Manufacturing of Electrochemical Energy Storage Systems Electrodes, Advanced Energy and Sustainability Research. 2 (2021) 2000111.

[130] D.A.C. da Silva, A.J. Paulista Neto, A.M. Pascon, E.E. Fileti, L.R.C. Fonseca, H.G. Zanin, Combined density functional theory and molecular dynamics simulations to investigate the effects of quantum and double-layer capacitances in functionalized graphene as the electrode material of aqueous-based supercapacitors, The Journal of Physical Chemistry C. 125 (2021) 5518–5524.

[131] B. Freitas, W.G. Nunes, D.M. Soares, F.C. Rufino, C.M. Moreira, L.M. Da Silva, H. Zanin, Robust, flexible, freestanding and high surface area activated carbon and multi-walled carbon nanotubes composite material with outstanding electrode properties for aqueous-based supercapacitors, Materials Advances. 2 (2021) 4264–4276.

[132] W.G. Nunes, A.N. Miranda, B. Freitas, R. Vicentini, A.C. Oliveira, G. Doubek, R.G. Freitas, L.M. Da Silva, H. Zanin, Charge-storage mechanism of highly defective NiO nanostructures on carbon nanofibers in electrochemical supercapacitors, Nanoscale. 13 (2021) 9590–9605.

[133] M. Alexandreli, C.B. Brocchi, D.M. Soares, W.G. Nunes, B.G. Freitas, F.E.R. de Oliveira, L.E.C.A. Schiavo, A.C. Peterlevitz, L.M. da Silva, H. Zanin, Pseudocapacitive behaviour of iron oxides supported on carbon nanofibers as a composite electrode material for aqueous-based supercapacitors, Journal of Energy Storage. 42 (2021) 103052.

[134] C.G. Real, R. Vicentini, W.G. Nunes, A.M. Pascon, F.A. Campos, L.M. Da Silva, R.G. Freitas, H. Zanin, Analyses of dispersive effects and the distributed capacitance in the time and frequency domains of activated carbon nanofiber electrodes as symmetric supercapacitors, Electrochimica Acta. 402 (2022) 139299.

[135] R. Vicentini, R. Beraldo, J.P. Aguiar, F.E. Oliveira, F.C. Rufino, D.R.G. Larrude, L.M. Da Silva, H. Zanin, Niobium pentoxide nanoparticles decorated graphene as electrode material in aqueous-based supercapacitors: Accurate determination of the working voltage window and the analysis of the distributed capacitance in the time domain, Journal of Energy Storage. 44 (2021) 103371.

[136] D.A.C. da Silva, A. Messias, E.E. Fileti, A. Pascon, D. V Franco, L.M. Da Silva, H.G. Zanin, others, Effect of conductivity, viscosity, and density of water-in-salt electrolytes on the electrochemical behavior of supercapacitors: molecular dynamics simulations and in situ characterization studies, Materials Advances. 3 (2022) 611–623.

[137] H. Zanin, A.C. Peterlevitz, H.J. Ceragioli, A.A. Rodrigues, W.D. Belangero, V. Baranauskas, Magnetic and cytotoxic properties of hot-filament chemical vapour deposited diamond, Materials Science and Engineering: C. 32 (2012) 2340–2343.

[138] M.M. Amaral, R. Venâncio, A.C. Peterlevitz, H. Zanin, Recent advances on quasi-solid-state electrolytes for supercapacitors, Journal of Energy Chemistry. 67 (2022) 697–717.

[139] R. Vicentini, R. Venâncio, W. Nunes, L.M. Da Silva, H. Zanin, New Insights on the Sodium Water-in-Salt Electrolyte and Carbon Electrode Interface from Electrochemistry and Operando Raman Studies, ACS Applied Materials \& Interfaces. 13 (2021) 61139–61153.

[140] A.J.P. Neto, D.A.C. da Silva, V.A. Gonçalves, H. Zanin, R.G. Freitas, E.E. Fileti, An evaluation of the capacitive behavior of supercapacitors as a function of the radius of cations using simulations with a constant potential method, Physical Chemistry Chemical Physics. 24 (2022) 3280–3288.

[141] N.A. Zambianco, V.A.O.P. da Silva, L.O. Orzari, E.J. Corat, H.G. Zanin, T.A. Silva, G.A. Buller, E.M. Keefe, C.E. Banks, B.C. Janegitz, Determination of tadalafil in pharmaceutical samples by vertically oriented multi-walled carbon nanotube electrochemical sensing device, Journal of Electroanalytical Chemistry. 877 (2020) 114501.

[142] M.M. Amaral, A.C. Peterlevitz, C.A.R. Júnior, L.M. Da Silva, H. Zanin, others, Robust, freestanding, and bendable multi-walled carbon nanotube buckypapers as electrode materials for quasi-solid-state potassium-ion supercapacitors, Diamond and Related Materials. 115 (2021) 108354.

[143] C.A.R. Júnior, E.R. Sanseverino, P. Gallo, D. Koch, H.-G. Schweiger, H. Zanin, Blockchain review for battery supply chain monitoring and battery trading, Renewable and Sustainable Energy Reviews. 157 (2022) 112078.

[144] W.G. Nunes, A.M. Pascon, B. Freitas, L.G. De Sousa, D. V Franco, H. Zanin, L.M. Da Silva, Electrochemical Behavior of Symmetric Electrical Double-Layer Capacitors and Pseudocapacitors and Identification of Transport Anomalies in the Interconnected Ionic and Electronic Phases Using the Impedance Technique, Nanomaterials. 12 (2022) 676.

[145] R. Venâncio, R. Vicentini, L.H. Costa, R. Teófilo, L.M. Da Silva, H. Zanin, In-situ electrochemical and operando Raman techniques to investigate the effect of porosity in different carbon electrodes in organic electrolyte supercapacitors, Journal of Energy Storage. 50 (2022) 104219.

[146] J.P.A. Santos, M.J. Pinzón, E.A. Santos, R. Vicentini, C.J.B. Pagan, L.M. Da Silva, H. Zanin, Boosting energy-storage capability in carbon-based supercapacitors using low-temperature water-in-salt electrolytes, Journal of Energy Chemistry. (2022).

[147] M.M. Amaral, V.Y. Yukuhiro, R. Vicentini, A.C. Peterlevitz, L.M. Da Silva, P. Fernandez, H. Zanin, Direct observation of the CO2 formation and C--H consumption of carbon electrode in an aqueous neutral electrolyte supercapacitor by in-situ FTIR and Raman, Journal of Energy Chemistry. 71 (2022) 488–496.

[148] S.H. Chung, A. Manthiram, Designing Lithium-Sulfur Cells with Practically Necessary Parameters, Joule. 2 (2018) 710–724. https://doi.org/10.1016/j.joule.2018.01.002.

[149] J. He, Y. Chen, A. Manthiram, MOF-derived Cobalt Sulfide Grown on 3D Graphene Foam as an Efficient Sulfur Host for Long-Life Lithium-Sulfur Batteries, IScience. 4 (2018) 36–43. https://doi.org/10.1016/j.isci.2018.05.005.

[150] A. Vittore, M.R. Acocella, G. Guerra, Graphite functionalization by ball milling with sulfur, SN Applied Sciences. 1 (2019). https://doi.org/10.1007/s42452-019-0179-z.

[151] A. Ghosh, S. Shukla, G.S. Khosla, B. Lochab, S. Mitra, Sustainable Sulfur-rich Copolymer/Graphene Composite as Lithium-Sulfur Battery Cathode with Excellent Electrochemical Performance, Scientific Reports. 6 (2016) 1–13. https://doi.org/10.1038/srep25207.

[152] J. Gao, M.A. Lowe, Y. Kiya, H.D. Abruña, Effects of liquid electrolytes on the charge-discharge performance of rechargeable lithium/sulfur batteries: Electrochemical and in-situ X-ray absorption spectroscopic studies, Journal of Physical Chemistry C. 115 (2011) 25132–25137. https://doi.org/10.1021/jp207714c.

[153] X. Liang, C.Y. Kwok, F. Lodi-Marzano, Q. Pang, M. Cuisinier, H. Huang, C.J. Hart, D. Houtarde, K. Kaup, H. Sommer, T. Brezesinski, J. Janek, L.F. Nazar, Tuning Transition Metal Oxide-Sulfur Interactions for Long Life Lithium Sulfur Batteries: The “goldilocks” Principle, Advanced Energy Materials. 6 (2016) 1–9. https://doi.org/10.1002/aenm.201501636.

[154] L. Borchardt, M. Oschatz, S. Kaskel, Carbon Materials for Lithium Sulfur Batteries - Ten Critical Questions, Chemistry - A European Journal. 22 (2016) 7324–7351. https://doi.org/10.1002/chem.201600040.

[155] R. Fang, J. Xu, D.W. Wang, Covalent fixing of sulfur in metal-sulfur batteries, Energy and Environmental Science. 13 (2020) 432–471. https://doi.org/10.1039/c9ee03408k.

[156] S.-E. Cheon, K.-S. Ko, J.-H. Cho, S.-W. Kim, E.-Y. Chin, H.-T. Kim, Rechargeable Lithium Sulfur Battery, Journal of The Electrochemical Society. 150 (2003) A800. https://doi.org/10.1149/1.1571533.

[157] Y. V. Mikhaylik, J.R. Akridge, Polysulfide Shuttle Study in the Li/S Battery System, Journal of The Electrochemical Society. 151 (2004) A1969. https://doi.org/10.1149/1.1806394.

[158] S.S. Zhang, Liquid electrolyte lithium/sulfur battery: Fundamental chemistry, problems, and solutions, Journal of Power Sources. 231 (2013) 153–162. https://doi.org/10.1016/j.jpowsour.2012.12.102.

[159] W. Kang, N. Deng, J. Ju, Q. Li, D. Wu, X. Ma, L. Li, M. Naebe, B. Cheng, A review of recent developments in rechargeable lithium-sulfur batteries, Nanoscale. 8 (2016) 16541–16588. https://doi.org/10.1039/c6nr04923k.

[160] C. Barchasz, F. Molton, C. Duboc, J.C. Leprêtre, S. Patoux, F. Alloin, Lithium/sulfur cell discharge mechanism: An original approach for intermediate species identification, Analytical Chemistry. 84 (2012) 3973–3980. https://doi.org/10.1021/ac2032244.

[161] M. Fang, X. Liu, J.C. Ren, S. Yang, G. Su, Q. Fang, J. Lai, S. Li, W. Liu, Revisiting the anchoring behavior in lithium-sulfur batteries: many-body effect on the suppression of shuttle effect, Npj Computational Materials. 6 (2020) 1–6. https://doi.org/10.1038/s41524-020-0273-1.

[162] X. Yu, Z. Bi, F. Zhao, A. Manthiram, Polysulfide-Shuttle Control in Lithium-Sulfur Batteries with a Chemically/Electrochemically Compatible NaSICON-Type Solid Electrolyte, Advanced Energy Materials. 6 (2016). https://doi.org/10.1002/aenm.201601392.

[163] S.K. Kannan, H. Hareendrakrishnakumar, M.G. Joseph, Efficient polysulfide shuttle mitigation by graphene-lithium cobalt vanadate hybrid for advanced lithium-sulfur batteries, Journal of Electroanalytical Chemistry. 899 (2021) 115665. https://doi.org/10.1016/j.jelechem.2021.115665.

[164] C. Weller, S. Thieme, P. Härtel, H. Althues, S. Kaskel, Intrinsic Shuttle Suppression in Lithium-Sulfur Batteries for Pouch Cell Application, Journal of The Electrochemical Society. 164 (2017) A3766–A3771. https://doi.org/10.1149/2.0981714jes.

[165] X. Huang, Z. Wang, R. Knibbe, B. Luo, S.A. Ahad, D. Sun, L. Wang, Cyclic Voltammetry in Lithium–Sulfur Batteries—Challenges and Opportunities, Energy Technology. 7 (2019) 1–13. https://doi.org/10.1002/ente.201801001.

[166] E. Umeshbabu, B. Zheng, Y. Yang, Recent Progress in All-Solid-State Lithium−Sulfur Batteries Using High Li-Ion Conductive Solid Electrolytes, Springer Singapore, 2019. https://doi.org/10.1007/s41918-019-00029-3.

[167] N. Li, F. Gan, P. Wang, K. Chen, S. Chen, X. He, In situ synthesis of 3D sulfur-doped graphene/sulfur as a cathode material for lithium-sulfur batteries, Journal of Alloys and Compounds. 754 (2018) 64–71. https://doi.org/10.1016/j.jallcom.2018.04.018.

[168] X. Yao, N. Huang, F. Han, Q. Zhang, H. Wan, J.P. Mwizerwa, C. Wang, X. Xu, High-Performance All-Solid-State Lithium – Sulfur Batteries Enabled by Amorphous Sulfur-Coated Reduced Graphene Oxide Cathodes, 1602923 (2017) 1–9. https://doi.org/10.1002/aenm.201602923.

[169] X. Judez, H. Zhang, C. Li, J.A. González-Marcos, Z. Zhou, M. Armand, L.M. Rodriguez-Martinez, Lithium Bis(fluorosulfonyl)imide/Poly(ethylene oxide) Polymer Electrolyte for All Solid-State Li-S Cell, Journal of Physical Chemistry Letters. 8 (2017) 1956–1960. https://doi.org/10.1021/acs.jpclett.7b00593.

[170] S. Waluś, C. Barchasz, R. Bouchet, F. Alloin, Electrochemical impedance spectroscopy study of lithium–sulfur batteries: Useful technique to reveal the Li/S electrochemical

mechanism, Electrochimica Acta. 359 (2020) 136944. https://doi.org/10.1016/j.electacta.2020.136944.

[171] P.P.R.M.L. Harks, C.B. Robledo, C. George, C. Wang, T. van Dijk, L. Sturkenboom, E.D.W. Roesink, F.M. Mulder, Immersion precipitation route towards high performance thick and flexible electrodes for Li-ion batteries, Journal of Power Sources. 441 (2019) 227200. https://doi.org/10.1016/j.jpowsour.2019.227200.

[172] B. Chavillon, L. Boutafa, E. Mayousse, B. Chavillon, L. Boutafa, E. Mayousse, Accepted Manuscript, (2018). https://doi.org/10.1016/j.electacta.2018.09.167.

[173] H.J. Peng, J.Q. Huang, X.B. Cheng, Q. Zhang, Review on High-Loading and High-Energy Lithium–Sulfur Batteries, Advanced Energy Materials. 7 (2017) 1–54. https://doi.org/10.1002/aenm.201700260.

[174] N. Angulakshmi, A.M. Stephan, Efficient electrolytes for lithium-sulfur batteries, Frontiers in Energy Research. 3 (2015) 1–8. https://doi.org/10.3389/fenrg.2015.00017.

[175] A. Kawase, S. Shirai, Y. Yamoto, R. Arakawa, T. Takata, Electrochemical reactions of lithium-sulfur batteries: An analytical study using the organic conversion technique, Physical Chemistry Chemical Physics. 16 (2014) 9344–9350. https://doi.org/10.1039/c4cp00958d.

[176] M. Wild, L. O’Neill, T. Zhang, R. Purkayastha, G. Minton, M. Marinescu, G.J. Offer, Lithium sulfur batteries, a mechanistic review, Energy and Environmental Science. 8 (2015) 3477–3494. https://doi.org/10.1039/c5ee01388g.

[177] M.W. Losey, J.J. Kelly, Electrodeposition, 2007. https://doi.org/10.1016/B978-044452190-3.00010-0.

[178] R. Vicentini, L.M. Da Silva, D. V. Franco, W.G. Nunes, J. Fiates, G. Doubek, L.F.M. Franco, R.G. Freitas, C. Fantini, H. Zanin, Raman probing carbon & aqueous electrolytes interfaces and molecular dynamics simulations towards understanding electrochemical properties under polarization conditions in supercapacitors, Journal of Energy Chemistry. 60 (2021) 279–292. https://doi.org/10.1016/j.jechem.2021.01.003.

[179] L.G. Cançado, A. Jorio, E.H.M. Ferreira, F. Stavale, C.A. Achete, R.B. Capaz, M.V.O. Moutinho, A. Lombardo, T.S. Kulmala, A.C. Ferrari, Quantifying defects in graphene

via Raman spectroscopy at different excitation energies, Nano Letters. 11 (2011) 3190–3196. https://doi.org/10.1021/nl201432g.

[180] A.C. Ferrari, J. Robertson, Resonant Raman spectroscopy of disordered, amorphous, and diamondlike carbon, Physical Review B - Condensed Matter and Materials Physics. 64 (2001) 75414. https://doi.org/10.1103/PhysRevB.64.075414.

[181] R. Tuma, G.J. Thomas, Raman Spectroscopy of Viruses, in: Handbook of Vibrational Spectroscopy, UFMG, 2006: p. 185. https://doi.org/10.1002/0470027320.s8207.

[182] P.D. Harvey, I.S. Butler, Raman spectra of orthorhombic sulfur at 40 K, Journal of Raman Spectroscopy. 17 (1986) 329–334. https://doi.org/10.1002/jrs.1250170407.

[183] C. Nims, B. Cron, M. Wetherington, J. Macalady, J. Cosmidis, Low frequency Raman Spectroscopy for micron-scale and in vivo characterization of elemental sulfur in microbial samples, Scientific Reports. 9 (2019) 1–12. https://doi.org/10.1038/s41598-019-44353-6.

[184] A.T. Ward, Raman spectroscopy of sulfur, sulfur-selenium, and sulfur-arsenic mixtures, The Journal of Physical Chemistry. 72 (1968) 4133–4139.

[185] F.P. Daly, C.W. Brown, Raman spectra of rhombic sulfur dissolved in secondary amines, Journal of Physical Chemistry. 80 (1976) 480–482. https://doi.org/10.1021/j100546a012.

[186] R. Vicentini, W. Nunes, B.G.A. Freitas, L.M. Da Silva, D.M. Soares, R. Cesar, C.B. Rodella, H. Zanin, Niobium pentoxide nanoparticles @ multi-walled carbon nanotubes and activated carbon composite material as electrodes for electrochemical capacitors, Energy Storage Materials. 22 (2019) 311–322. https://doi.org/10.1016/j.ensm.2019.08.007.

[187] R. Vicentini, D.M. Soares, W. Nunes, B. Freitas, L. Costa, L.M. Da Silva, H. Zanin, Core-niobium pentoxide carbon-shell nanoparticles decorating multiwalled carbon nanotubes as electrode for electrochemical capacitors, Journal of Power Sources. 434 (2019). https://doi.org/10.1016/j.jpowsour.2019.226737.

[188] R. Vicentini, W. Nunes, B.G.A. Freitas, L.M. Da Silva, D.M. Soares, R. Cesar, C.B. Rodella, H. Zanin, Niobium pentoxide nanoparticles @ multi-walled carbon nanotubes

and activated carbon composite material as electrodes for electrochemical capacitors, Energy Storage Materials. 22 (2019) 311–322. https://doi.org/10.1016/j.ensm.2019.08.007.

[189] R. Vicentini, W.G. Nunes, L.H. Costa, A. Pascon, L.M. Da Silva, M. Baldan, H. Zanin, Environmentally friendly functionalization of porous carbon electrodes for aqueous-based electrochemical capacitors, IEEE Transactions on Nanotechnology. 18 (2019) 73–82. https://doi.org/10.1109/TNANO.2018.2878663.

[190] X. Wu, S. Li, B. Wang, J. Liu, M. Yu, Free-standing 3D network-like cathode based on biomass-derived N-doped carbon/graphene/g-C3N4 hybrid ultrathin sheets as sulfur host for high-rate Li-S battery, Renewable Energy. 158 (2020) 509–519. https://doi.org/10.1016/j.renene.2020.05.098.

[191] L. Peng, Z. Wei, C. Wan, J. Li, Z. Chen, D. Zhu, D. Baumann, H. Liu, C.S. Allen, X. Xu, A.I. Kirkland, I. Shakir, Z. Almutairi, S. Tolbert, B. Dunn, Y. Huang, P. Sautet, X. Duan, A fundamental look at electrocatalytic sulfur reduction reaction, Nature Catalysis. (2020). https://doi.org/10.1038/s41929-020-0498-x.

[192] F. Buckel, F. Effenberger, C. Yan, A. Gölzhäuser, M. Grunze, Influence of aromatic groups incorporated in long-chain alkanethiol self-assembled monolayers on gold, Advanced Materials. 12 (2000) 901–905. https://doi.org/10.1002/1521-4095(200006)12:12<901::AID-ADMA901>3.0.CO;2-B.

[193] L. Qie, W. Chen, X. Xiong, C. Hu, F. Zou, P. Hu, Y. Huang, Sulfur-doped carbon with enlarged interlayer distance as a high-performance anode material for sodium-ion batteries, Advanced Science. 2 (2015).

[194] W. Gu, M. Sevilla, A. Magasinski, A.B. Fuertes, G. Yushin, Sulfur-containing activated carbons with greatly reduced content of bottle neck pores for double-layer capacitors: A case study for pseudocapacitance detection, Energy and Environmental Science. 6 (2013) 2465–2476. https://doi.org/10.1039/c3ee41182f.

[195] G. Zhou, Y. Zhao, A. Manthiram, Dual-Confined Flexible Sulfur Cathodes Encapsulated in Nitrogen-Doped Double-Shelled Hollow Carbon Spheres and Wrapped with Graphene for Li – S Batteries, (2015) 1–10. https://doi.org/10.1002/aenm.201402263.

[196] X. Li, M. Rao, D. Chen, H. Lin, Y. Liu, Y. Liao, L. Xing, W. Li, Sulfur supported by carbon nanotubes and coated with polyaniline: Preparation and performance as cathode of lithium-sulfur cell, Electrochimica Acta. 166 (2015) 93–99. https://doi.org/10.1016/j.electacta.2015.03.070.

[197] G. Zheng, Y. Yang, J.J. Cha, S.S. Hong, Y. Cui, Hollow Carbon Nanofiber-Encapsulated Sulfur Cathodes for High Specific Capacity Rechargeable Lithium Batteries, (2011) 4462–4467.

[198] C. Shen, J.E. Soc, C. Shen, J. Xie, M. Zhang, P. Andrei, M. Hendrickson, E.J. Plichta, J.P. Zheng, Self-Discharge Behavior of Lithium-Sulfur Batteries at Different Electrolyte / Sulfur Ratios JES F OCUS I SSUE OF S ELECTED P APERS FROM IMLB 2018 Self-Discharge Behavior of Lithium-Sulfur Batteries at Different Electrolyte / Sulfur Ratios, (2019). https://doi.org/10.1149/2.0461903jes.

[199] X. Qiu, Q. Hua, L. Zheng, Z. Dai, Study of the discharge/charge process of lithium-sulfur batteries by electrochemical impedance spectroscopy, RSC Advances. (2020). https://doi.org/10.1039/c9ra10527a.

[200] A. Lasia, Electrochemical Impedance Spectroscopy and its Applications BT - Modern Aspects of Electrochemistry, Modern Aspects of Electrochemistry. 32 (2002) 143–248. http://dx.doi.org/10.1007/0-306-46916-2_2%5Cnpapers2://publication/doi/10.1007/0-306-46916-2_2.

[201] S. Waluš, C. Barchasz, R. Bouchet, J.C. Leprêtre, J.F. Colin, J.F. Martin, E. Elkaïm, C. Baehtz, F. Alloin, Lithium/Sulfur Batteries Upon Cycling: Structural Modifications and Species Quantification by in Situ and Operando X-Ray Diffraction Spectroscopy, Advanced Energy Materials. 5 (2015) 1–5. https://doi.org/10.1002/aenm.201500165.

[202] Z. Deng, Z. Zhang, Y. Lai, J. Liu, J. Li, Y. Liu, Electrochemical Impedance Spectroscopy Study of a Lithium/Sulfur Battery: Modeling and Analysis of Capacity Fading, Journal of The Electrochemical Society. 160 (2013) A553–A558. https://doi.org/10.1149/2.026304jes.

[203] A. Manuscript, Materials Chemistry A, (2017). https://doi.org/10.1039/C7TA04962E.

[204] M. Hagen, G. Feisthammel, P. Fanz, H.T. Grossmann, S. Dörfler, J. Tübke, M.J. Hoffmann, D. Börner, M. Joos, H. Althues, S. Kaskel, Sulfur Cathodes with Carbon

Current Collector for Li-S cells, Journal of The Electrochemical Society. 160 (2013) A996–A1002. https://doi.org/10.1149/2.149306jes.

[205] J. Zheng, M. Gu, H. Chen, P. Meduri, M.H. Engelhard, J.G. Zhang, J. Liu, J. Xiao, Ionic liquid-enhanced solid state electrolyte interface (SEI) for lithium-sulfur batteries, Journal of Materials Chemistry A. (2013). https://doi.org/10.1039/c3ta11553d.

[206] S. Ghosh, A. Paul, P. Samanta, B. Landge, S.K. Mandal, S. Sinha, G.G. Dutta, N.C. Murmu, T. Kuila, Influence of transition metals (Cu and Co) on the carbon-coated nickel sulfide used as positive electrode material in hybrid supercapacitor device, Journal of Composites Science. 5 (2021) 1–15. https://doi.org/10.3390/jcs5070180.

[207] J. Song, M.Z. Bazant, Effects of Nanoparticle Geometry and Size Distribution on Diffusion Impedance of Battery Electrodes, Journal of The Electrochemical Society. 160 (2013) A15–A24. https://doi.org/10.1149/2.023301jes.

[208] A.C. Ferrari, J.C. Meyer, V. Scardaci, C. Casiraghi, M. Lazzeri, F. Mauri, S. Piscanec, D. Jiang, K.S. Novoselov, S. Roth, A.K. Geim, Raman spectrum of graphene and graphene layers, Physical Review Letters. 97 (2006) 1–4. https://doi.org/10.1103/PhysRevLett.97.187401.

[209] M. Raja, N. Angulakshmi, A.M. Stephan, Sisal-derived activated carbons for cost-effective lithium-sulfur batteries, RSC Advances. 6 (2016) 13772–13779. https://doi.org/10.1039/c5ra25850b.

[210] L. Wang, T. Zhang, S. Yang, F. Cheng, J. Liang, J. Chen, A quantum-chemical study on the discharge reaction mechanism of lithium-sulfur batteries, Journal of Energy Chemistry. 22 (2013) 72–77. https://doi.org/10.1016/S2095-4956(13)60009-1.

[211] Y. Zhang, C. Fincher, S. McProuty, M. Pharr, In-operando imaging of polysulfide catholytes for Li–S batteries and implications for kinetics and mechanical stability, Journal of Power Sources. 434 (2019) 226727. https://doi.org/10.1016/j.jpowsour.2019.226727.

[212] X. Chen, T.Z. Hou, B. Li, C. Yan, L. Zhu, C. Guan, X.B. Cheng, H.J. Peng, J.Q. Huang, Q. Zhang, Towards stable lithium-sulfur batteries: Mechanistic insights into electrolyte decomposition on lithium metal anode, Energy Storage Materials. 8 (2017) 194–201. https://doi.org/10.1016/j.ensm.2017.01.003.

[213] F. Liu, G. Sun, H. Bin Wu, G. Chen, D. Xu, R. Mo, L. Shen, X. Li, S. Ma, R. Tao, X. Li, X. Tan, B. Xu, G. Wang, B.S. Dunn, P. Sautet, Y. Lu, Dual redox mediators accelerate the electrochemical kinetics of lithium-sulfur batteries, Nature Communications. 11 (2020) 1–10. https://doi.org/10.1038/s41467-020-19070-8.

[214] X. Wang, S. Cai, D. Zhu, S. Mu, Y. Chen, The investigation of water vapor on the Li–O2 battery using a solid-state air cathode, Journal of Solid State Electrochemistry. 19 (2015) 2421–2429. https://doi.org/10.1007/s10008-015-2887-7.

[215] Z. Shen, S. Lang, C. Zhou, R. Wen, L. Wan, In Situ Realization of Water-Mediated Interfacial Processes at Nanoscale in Aprotic Li–O 2 Batteries, Advanced Energy Materials. 10 (2020) 2002339. https://doi.org/10.1002/aenm.202002339.

[216] H.L. Wu, R.T. Haasch, B.R. Perdue, C.A. Apblett, A.A. Gewirth, The effect of water-containing electrolyte on lithium-sulfur batteries, Journal of Power Sources. 369 (2017) 50–56. https://doi.org/10.1016/j.jpowsour.2017.09.044.